ABSTRACT

RELATIONSHIP BETWEEN PHOTOSPHERIC MAGNETIC FIELDS AND CORONAL ACTIVITIES

by
Changyi Tan

Coronal emission comes in two forms, a steady component where the corona is heated to million degrees and a much hotter transient component of solar flares. Both components are known to be related to the evolution of surface magnetic fields. This dissertation studies the evolution of photospheric magnetic fields and flow fields and their relation to the properties of these two coronal emission components.

The key issue in the study of the steady coronal emission is the coronal heating problem: how the corona is heated to millions of degrees while the underlying solar photosphere is only a few thousand degrees. Although there is theoretical and observational evidence to support many aspects of certain heating models, the general agreement is not yet reached. Even the location of the heating source is still under debate. In this dissertation, the correlations between some photospheric magnetic parameters and coronal soft X-ray brightness are statistically evaluated to contribute to resolving the problems of coronal heating. The key findings include: (1) The energy of the Poynting flux is sufficient to heat the corona due to footpoint random motions of magnetic flux tubes. (2) Close correlation is established between coronal brightness and various magnetic parameters. (3) Evolution of 3-D magnetic structure in the form of free magnetic energy plays an additional role in the heating of corona. (4) The coronal holes (lower temperature region) shows more stable magnetic structure than the surrounding areas, demonstrating that the magnetic reconnection frequently occurs in the coronal hole boundary to increase the temperature outside the

holes.

For the transient coronal activity, for example solar flare, the linkage between flare productivity and the free magnetic energy of active regions is explored. The key findings are: (1) For the first time, a positive correlation is found between the available free magnetic energy and flare productivity. (2) Based on the study of the temporal variation of free magnetic energy in flaring and flare-quiet active regions, free magnetic energy is not found to exhibit a clear and consistent pre-flare pattern. Therefore, the triggering mechanism of flares is as important as the energy storage in active regions. (3) As a case study, the topology changes of active region NOAA10930 magnetic fields before and after an X3.4 class flare on December 13, 2006 are studied. For the first time, rapid and permanent changes of optical penumbral and shear flows before and after the flares are found.

This dissertation took the advantage of comprehensive data from several solar space mission such as *SoHO* (*MDI*, *EIT*), *Hinode* (*SOT*, *XRT*) and *Yohkoh* (*SXT*) and ground-based data, e.g. *SOLIS*. Some most advanced data analysis tools were utilized, such as local correlation tracking, Stokes inversion, 180° ambiguity resolution, potential/non-potential field extrapolation and line ratio technique to extract coronal temperature.

RELATIONSHIP BETWEEN PHOTOSPHERIC MAGNETIC FIELDS AND CORONAL ACTIVITIES

by

Changyi Tan

A Dissertation
Submitted to the Faculty of
New Jersey Institute of Technology and
Rutgers, the State University of New Jersey - Newark
in Partial Fulfillment of the Requirements for the Degree of
Doctor of Philosophy in Applied Physics

Federated Physics Department

January 2010

APPROVAL PAGE

RELATIONSHIP BETWEEN PHOTOSPHERIC MAGNETIC FIELDS AND CORONAL ACTIVITIES

Changyi Tan

12/7/09

Dr. Haimin Wang, Dissertation Advisor — Date
Distinguished Professor of Physics, Director of Space Weather Research Laboratory, NJIT

12/7/09

Dr. Dale E. Gary, Committee Member — Date
Distinguished Professor of Physics, Director of Owens Valley Solar Array, NJIT

12/07/09

Dr. Wenda Cao, Committee Member — Date
Assistant Professor of Physics, NJIT

12/07/09

Dr. Tao Zhou, Committee Member — Date
Assistant Professor of Physics, NJIT

12/07/09

Dr. Martin Schaden, Committee Member — Date
Associate Professor of Physics, Rutgers University, Newark

BIOGRAPHICAL SKETCH

Author: Changyi Tan

Degree: Doctor of Philosophy

Date: January 2010

Undergraduate and Graduate Education:

- Doctor of Philosophy in Applied Physics,
  New Jersey Institute of Technology, Newark, New Jersey, 2010
- Master of Science in Plasma Physics,
  Institute of Applied Physics and Computational Mathematics, Beijing, China, 2004
- Bachelor of Science in Astronomy,
  Nanjing University, Nanjing, China, 2001

Major: Applied Physics

Journal Publications:

Tan, Changyi; Jing, Ju; Abramenko, V.I.; Pevtsov, A.A.; Song, Hui; Park, Sung-Hong and Wang, Haimin , 2007, *Statistical Correlation between Parameters of Photospheric Magnetic Field and Coronal Soft X-ray Brightness,* The Astrophysical Journal, 665, 1460.

Tan, Changyi; Chen, P.F.; Abromenko, Valentyna and Wang, Haimin, 2009, *Evolution of Optical Penumbral and Shear Flows Associated with the X3.4 Flare of 2006 December 13*, The Astrophysical Journal, 690, 1820.

Song, Hui; Tan, Changyi; Jing, Ju; Wang, Haimin; Yurchyshyn, Vasyl and Abramenko, V.I., 2009, *Statistical Assessment of Photospheric Magnetic Features in Imminent Solar Flares Predictions*, Solar Physics, 254, 101.

Jing, Ju; Song, Hui; Abramenko, Valentyna; Tan, Changyi; Wang, Haimin, 2006, *The Statistical Relationship between the Photospheric Magnetic Parameters and the Flare Productivity of Active Regions*, Astrophysical Journal, 644, 1273.

Song, Hui; Yurchyshyn, Vasyl; Yang, Guo; Tan, Changyi; Chen, Weizhong; Wang, Haimin, 2006, *The Automatic Predictability of Super Geomagnetic Storms from Halo CMEs Associated with Large Solar Flares*, Solar Physics, 238, 141.

Wang, Haimin; Jing, Ju; Tan, Changyi; Wiegelmann, Thomas and Kubo, Masahito, 2008, *Study of Magnetic Channel Structure in Active Region 10930*, The Astrophysical Journal, 687, 658.

Chen, Wei-Zhong; Liu, Chang; Song, Hui, Deng; Na, Tan, Chang-Yi and Wang, Hai-Min, 2007, *A Statistical Study of Rapid Sunspot Structure Change Associated with Flares*, Chinese Journal of Astronomy and Astrophysics, 7, 733.

Jing, Ju; Tan, Changyi; Yuan, Yuan; Wang, Benjamin; Wiegelmann, Thomas; Xu, Yan, and Wang, Haimin, 2009, *Free Magnetic Energy and Flare Productivity of Active Regions*, Submitted to The Astrophysical Journal.

Tan, Changyi; Jing, Ju; Reale, Fabio and Wang, Haimin, 2009, *Relationship between 3-D Magnetic Structure and Coronal Emissions*, in preparation.

To

My Wife: Xu, Guohong

My Parents: Tan, Zhian and He, Xueyu

My Parents-in-law: Xu, Shihe and Zhang, Yunxiang

My Sister: Tan, Fengyi

ACKNOWLEDGMENT

First and foremost, I would like to gratefully thank my dissertation advisor, Dr. Haimin Wang. He is the first person who introduced the field of solar physics to me. He is much more than an advisor and helps me in all aspects. He shows me a scientist with rigor and integrity. Without his guidance, patience, encouragement and support, I would not finish this thesis. He is always extremely generous and open with his time and ideas. I am deeply attracted and impressed by his broad knowledge, wisdom and passion for solar physics. His character will influence me for a lifetime.

My gratitude goes to Dr. Dale E. Gary and Dr. Carsten Denker. They are very amiable and easy to access if I have questions for them. Dr. Gary not only taught me Radio Astronomy twice, he is also a best example of a real scientist. Dr. Denker taught me Solar Physics and helped me with IDL programming techniques.

I am also grateful to Dr. Ju Jing. She never failed to help me with my draft revisions.

Sincere thanks go to my other committee members, Dr. Wenda Cao, Dr. Tao Zhou and Dr. Martin Schaden, for their helpful suggestions and comments on my thesis and serving as a committee member.

I would like to acknowledge Dr. Richard A. Shine, Dr. A.A. Pevtsov and Dr. P.F. Chen for their patient help with LCT techniques and draft revisions.

I would also like to thank all the rest of the academic and support staff of the Center for Solar-Terrestrial Research and New Jersey Institute of Technology for providing resources and financial support. Our secretory, Christine Oertel, deserves special thanks for her support.

Much respect to my groupmates and friends: Hui Song, Sipeng Gu, Peng Gao, Yan Xu, Chang Liu, Zhiwei Liu, Rui Liu, Na Deng, Gang Fu, Weizhong Chen, Zhen Qin, Yixuan Li, Yuan Yuan, Zhaozhao Li, Ke Su, Zimeng Cheng, Tao Wu, Shuli Teng. Thanks for all the help.

Especially, I would like to give my special thanks to my parents, Tan, Zhian and He, Xueyu, for their priceless love. Lastly, and most importantly, I am deeply thankful to my wife, Guohong Xu, for her love and encouragement through these years. To them I dedicate this dissertation.

This dissertation was supported by the NSF, under grants ATM- 0548952, ATM-0536921, ATM-0716512, ATM 07-16950, ATM 09-36665, and by NASA, under grants NNGO- 4GJ51G, NNXO-7AH78G, NNX0-8AQ90G.

TABLE OF CONTENTS

Chapter **Page**

TABLE OF CONTENTS
(Continued)

TABLE OF CONTENTS
(Continued)

LIST OF TABLES

LIST OF FIGURES

Figure **Page**

LIST OF FIGURES
(Continued)

Figure **Page**

LIST OF FIGURES
(Continued)

LIST OF FIGURES
(Continued)

Figure **Page**

LIST OF FIGURES
(Continued)

LIST OF FIGURES
(Continued)

Figure **Page**

CHAPTER 1

INTRODUCTION

The mechanism of coronal heating, after more than seven decades of study (Grotrian 1939; Edlén 1943; Klimchuk 2006), still remains an open issue. This issue is to solve the problem why and how the corona is heated to several million degrees of temperature, while the underlying photosphere's temperature is only 6000 degrees. Generally, it is believed that the coronal heat energy is from the magnetic fields in the coronal volume above the photosphere (Priest 1990; Browning 1991; Spicer 1991; Cargill 1993; Wolfson et al. 2000). Consequently, the solar corona should respond to the evolution of photospheric magnetic fields. The key is to identify and understand the steady heating mechanism of the magnetic energy transportation and transformation.

The solar flare is a transient process of magnetic energy release in the corona through reconnecting magnetic fields. The impulsive process not only heats the local plasma to temperatures of tens of millions of degrees, but also rapidly accelerates electrons to keV/MeV energy range. The transient coronal emission covers all wavelengths from decameter radio waves to gamma-rays at 100 MeV (Benz 2008). Not surprisingly, impulsive magnetic reconnection takes place in the corona, but the magnetic source is ultimately rooted in photosphere. As for the coronal heating problem, the study of photospheric magnetic fields and evolution is critically important to understand solar flares.

The important solar magnetic fields are manifested by various steady solar features, such as sunspots, filaments (or prominences), plage and magnetic network, and explosive events, e.g. flares and coronal mass ejections (CMEs). The magnetic fields are generated inside the Sun, interact in the solar photosphere, chromosphere, transition region and solar corona, and propagate into interplanetary space. The magnetic fields provide energy to heat the solar atmosphere. Moreover, the photospheric magnetic parameters might be classified into two categories: one is more related to eruptive events, the other one is more related to the steady coronal heating. Therefore, the photospheric magnetic fields are critical for studies of both coronal heating and flares.

This chapter will overall review topics related to my dissertation work: photosphere, corona, magnetism, coronal heating and solar flares.

1.1 Our Star — The Sun

The nearest star, the Sun, is only 150 million km from us. It is a normal main-sequence G2 star. The Sun's energy comes from nuclear processes deep in its interior, the "core", where is has 10 million K temperature and about 100 billion times the Earth's atmospheric pressure. The composition of the Sun is about 70% hydrogen, 28% helium and less than 2% other elements. The energy of the inner nuclear reactions is transported outward by convection and radiation. Because of the high plasma density, the photon mean free path is short and it would take even hundreds of thousands of years to transport a photon from the core to the outer surface. From the interior to the solar atmosphere, the Sun can be divided into six layers: the core (which occupies the innermost quarter or so of the Sun's radius), the radiative zone, the convective zone, then the visible solar atmospheric layers called photosphere, the chromosphere, and the outermost layer, the corona (see Figure 1.1 and 1.2). The interior layers, e.g. core, radiative zone and convective zone can be studied by helioseismology. There are three important kinds of waves, acoustic, gravity, and surface gravity waves. These three wave types generate p-modes, g-modes, and f-modes, respectively, as resonant modes of oscillation because the Sun acts as a resonant cavity. The three outer layers, photosphere, chromosphere and corona can be directly observed through the emissions covering all the wavelengths from 10 m to 10^{-3} Å, spanning radio, infrared, optical, ultraviolet, X-ray and gamma-ray emissions.

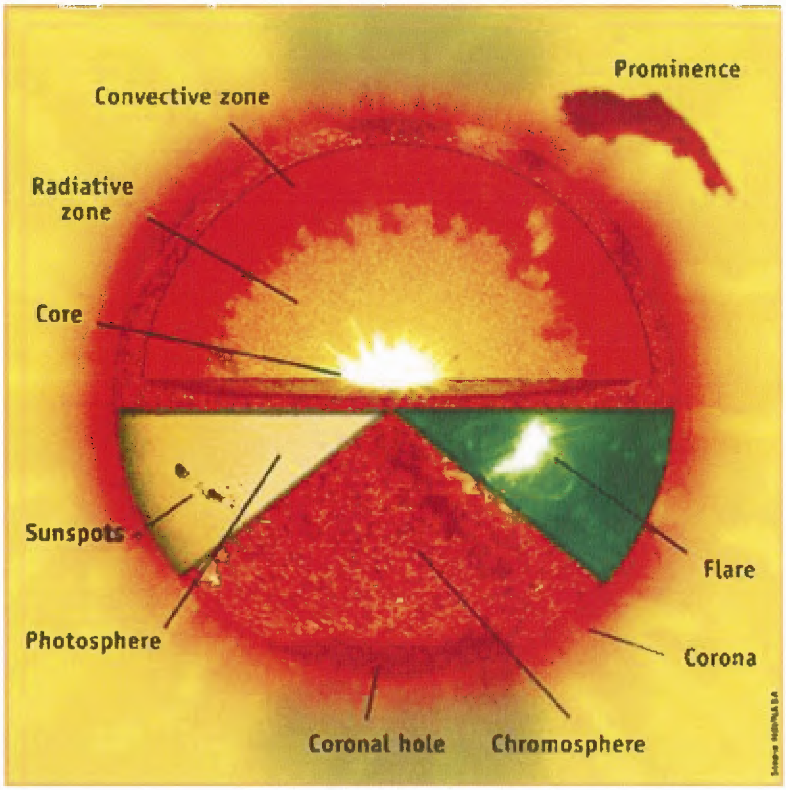

Figure 1.1 The structure of the Sun. (Photo courtesy SOHO consortium. *SoHO* is a project of international cooperation between the European Space Agency and the U.S. National Aeronautics and Space Administration.)

The hot ionized magnetized gases of the Sun exhibit differential rotation: near the solar equator the surface rotates once every 25.4 days, but near the poles the rotation period is as much as 36 days. This is a common feature of most stars. Because of differential rotation, Coriolis forces and induction, the combined effect, called the solar dynamo, is the main mechanism that drives the 22-year magnetic cycle. In another words, a rotating body

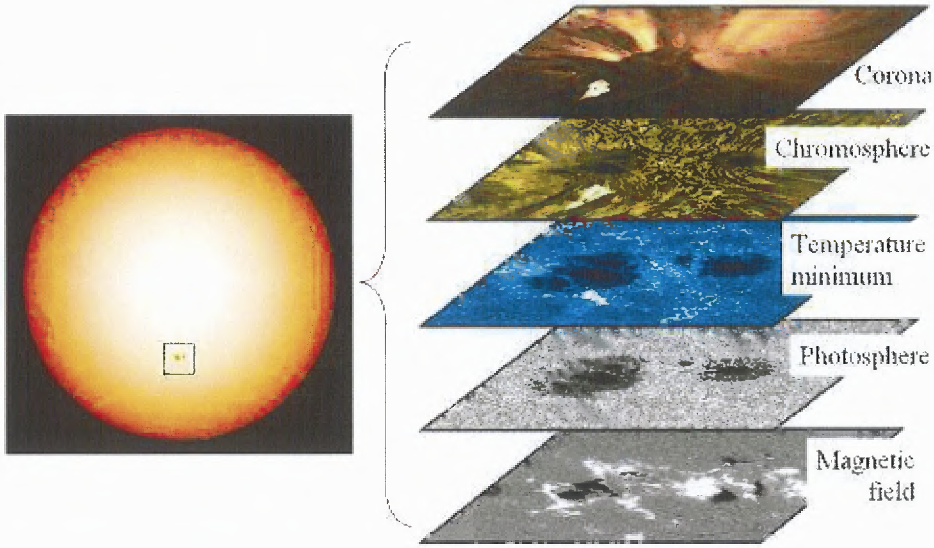

Figure 1.2 The stratified structure of the solar atmosphere (courtesy of *Hinode* Team).

of conductive plasma develops self-amplifying electric currents, and then the electric currents produce self-consistent magnetic fields to magnetize the gas. The differential rotation extends about one-third of the way down into the interior of the Sun but the rest of the Sun rotates as a rigid body (Stix 1989).

The solar magnetic fields (see Figure 1.3) play a dominant role in all solar activities, e.g. solar flares, coronal mass ejections, filament eruptions and coronal heating. The strong magnetic fields are concentrated in sunspots or active regions, while the weaker fields are dispersed throughout the entire Sun, e.g. plage, quiet Sun areas and coronal holes (e.g. Figure 1.4). Consequently, the key to solar physics is to understand the interactions between magnetic fields and plasma on all scales.

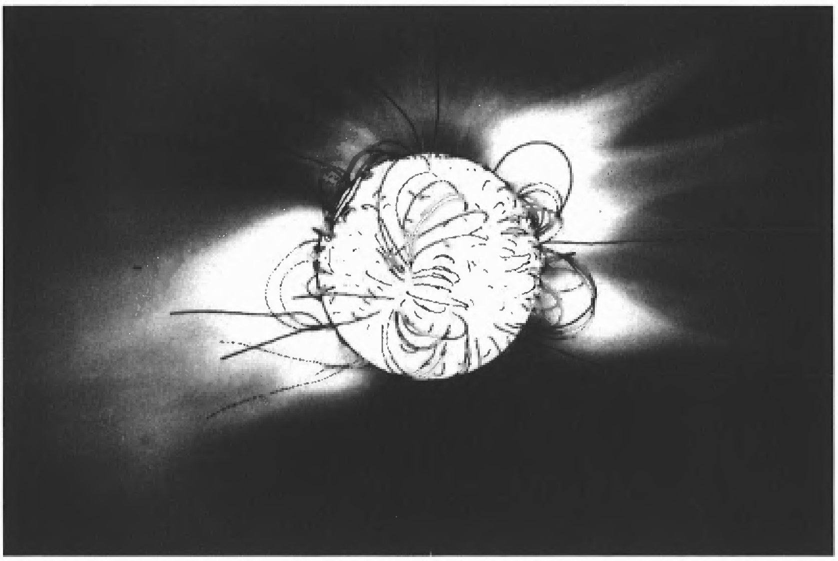

Figure 1.3 The schematic topology of the magnetic fields of the whole Sun, like a hairy ball. (Courtesy of Ms. Lee Slone)

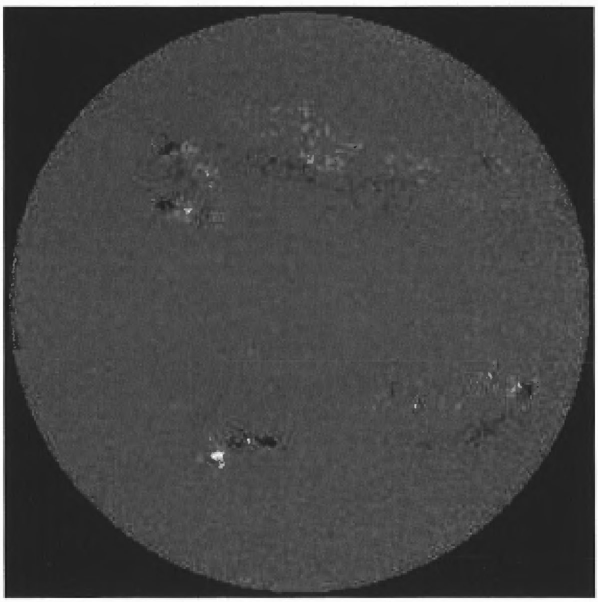

Figure 1.4 The *SoHO* MDI magnetogram on January 27, 1998. (courtesy of *SoHO* Team)

1.2 The Photosphere

The photosphere, the visible surface of the Sun, is the layer below which the Sun becomes opaque, or optically thick. Above the photosphere the visible light is free to propagate outward into space. Because H^- ions absorb visible light easily and the abundance of H^- ions decreases rapidly in the photosphere, the opacity decreases rapidly as well (Abhyankar 1977). The physical thickness of photosphere is about several hundred kilometers which is a relatively thin layer of the Sun. The photosphere is often referred to as the Sun's surface. The spectrum of the radiation from the photosphere is approximately a black-body spectrum from which one can infer the temperature of photosphere to be about 6000 Kelvin. But the black-body spectrum is interspersed with atomic absorption/emission lines from the tenuous atmosphere. The atoms in the Sun's atmosphere will absorb certain frequencies of energy in the electromagnetic spectrum, producing characteristic dark absorption lines in the spectrum (see Figure 1.5) (Stix 1989). The photosphere has a particle number density of $\sim 10^{14} cm^{-3}$ which is about 1% of the density of Earth's atmosphere at sea level.

In areas of strong magnetic concentration, the photosphere exhibits dark sunspots with distinct boundaries between umbra and penumbra in continuum or G-band observations. The "dark" appearance is because sunspots are cooler than the quiet Sun areas around them. The umbral temperature of a typical sunspot is about 4000 K which is much lower than the surface temperature of the photosphere in the quiet Sun areas. Sunspots can be as large as 50,000 km in diameter. The magnitude of sunspot magnetic field decreases gradually from the center, where it is about 3000 G, to the outer part, where it is several hundred Gauss (Denker 2005). Because of the strong magnetic field in sunspots, heat conduction is impeded by the magnetic field, which makes the umbra much cooler. The measurement of

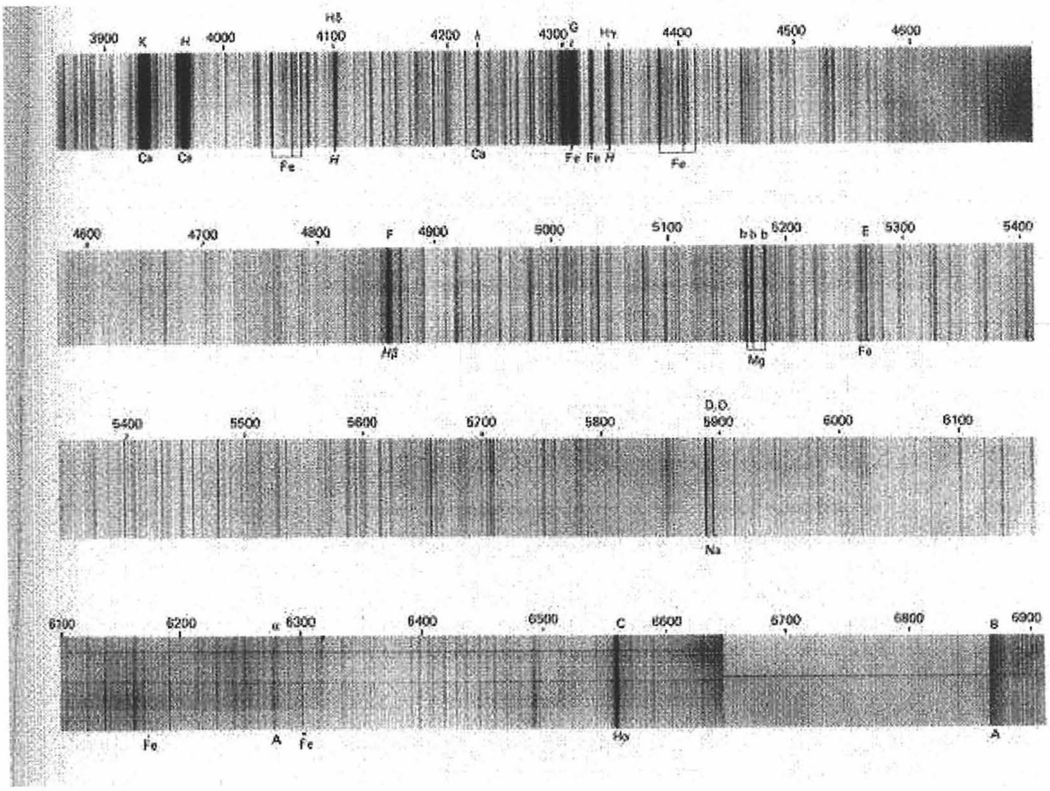

Figure 1.5 The solar optical spectra (Stix 1989).

photospheric magnetic field will be discussed in Section 1.4.

It is known that the convective zone connects the radiative zone and photosphere via as many as four distinct scales of convection: granulation, mesogranulation, supergranulation and giant cells. The granulation and supergranulation have been intensively studied by many authors (e.g. Hart 1954, 1956; Schwarzchild 1959; Bray et al. 1984a,b; Title et al. 1987), while the mesogranulation and giant cells have not yet been verified. The size of a granule is about 1000 km with life-time 10-20 min. Supergranules have typical sizes of 30 Mm and typical life-time 1-2 days. Magnetic concentration at the boundary of granules is called filigree which can be clearly seen in high-resolution G-band or some white light images. On a larger scale, the magnetic network corresponds to the supergranule boundary. In regions of quiet Sun, magnetic fields inside the network boundary are called intranetwork fields (Livingston & Harvey 1975; Harvey 1977). The discrete magnetic elements, in the form of network and intranetwork, cover the entire photosphere.

1.3 The Corona

The first observations of the solar corona can be dated to ancient eclipse records from historical sources of China and India. Solar eclipses were recorded in China as early as 2800 BC (Guillermier & Koutchmy 1999). Around 1942, solar physicists identified forbidden lines of highly ionized atoms and realized the high temperature of the corona (Bray et al. 1991).

The solar corona is a region that extends from 2.8 Mm to millions of kilometers above the solar photosphere. It has a lower plasma density than the photosphere, but with much higher temperature, 10^6 - 10^7 kelvin. Because of its temperature, the coronal plasma is highly ionized. The corona consists of such structures as closed loops, open bundles or streams of plasma which are shaped by magnetic fields that emerge from the Sun. The temperature of a given structure varies along each field line. By distinguishing its location in the corona, solar coronal phenomena can be subdivided into three categories: active regions (ARs), quiet Sun regions (QSs) and coronal holes (CHs) (see Figure 1.6). They exhibit a characteristic temperature trends: CHs have the coolest temperatures of T $\sim$ 1 MK; QSs are about 2 MK; while nonflaring active regions are hottest, about 2-6 MK (Aschwanden 2009). Magnetic fields in ARs and QSs are mostly closed loops, while in CHs they are dominated by open fields. Active regions typically consist of strong magnetic field concentrations with opposite magnetic polarities. Due to the dynamic processes in active regions such as magnetic flux emergence, reconnection, cancellation and reconfiguration, the heated plasma flows upward and fills the coronal loop, which makes the coronal loops hotter and denser than the coronal background. This is the reason that active regions are so bright in soft X-rays. The quiet Sun regions make up a large fraction of total solar surface area. In fact, the quiet Sun regions are not really "*quiet*". The dynamic processes, physically equivalent to active regions, reach down to smaller scales, such as nanoflares (Parker 1988), microflares (van Speybroek et al. 1970), explosive events (Brueckner & Bartoe 1983), and soft X-ray jets (Shibata et al. 1992; Alexander & Fletcher 1999). From high resolution observations, the basic physics governing active regions and quiet Sun regions is getting more and more similar except in the spatial scales. Coronal holes, the darkest areas of the corona, often locate in the northern and southern polar zones. They can also occasionally appear in other places including the equatorial zones. Coronal holes, which are the origin of the fast solar wind, are dominated by open magnetic field lines.

The open field lines allow heated plasma from the Sun to escape into interplanetary space and form the spiral solar wind. Because of lower plasma density, the coronal hole regions appear much darker than quiet Sun (Aschwanden 2009). Because of the efficient plasma transport, CHs are much cooler than other regions.

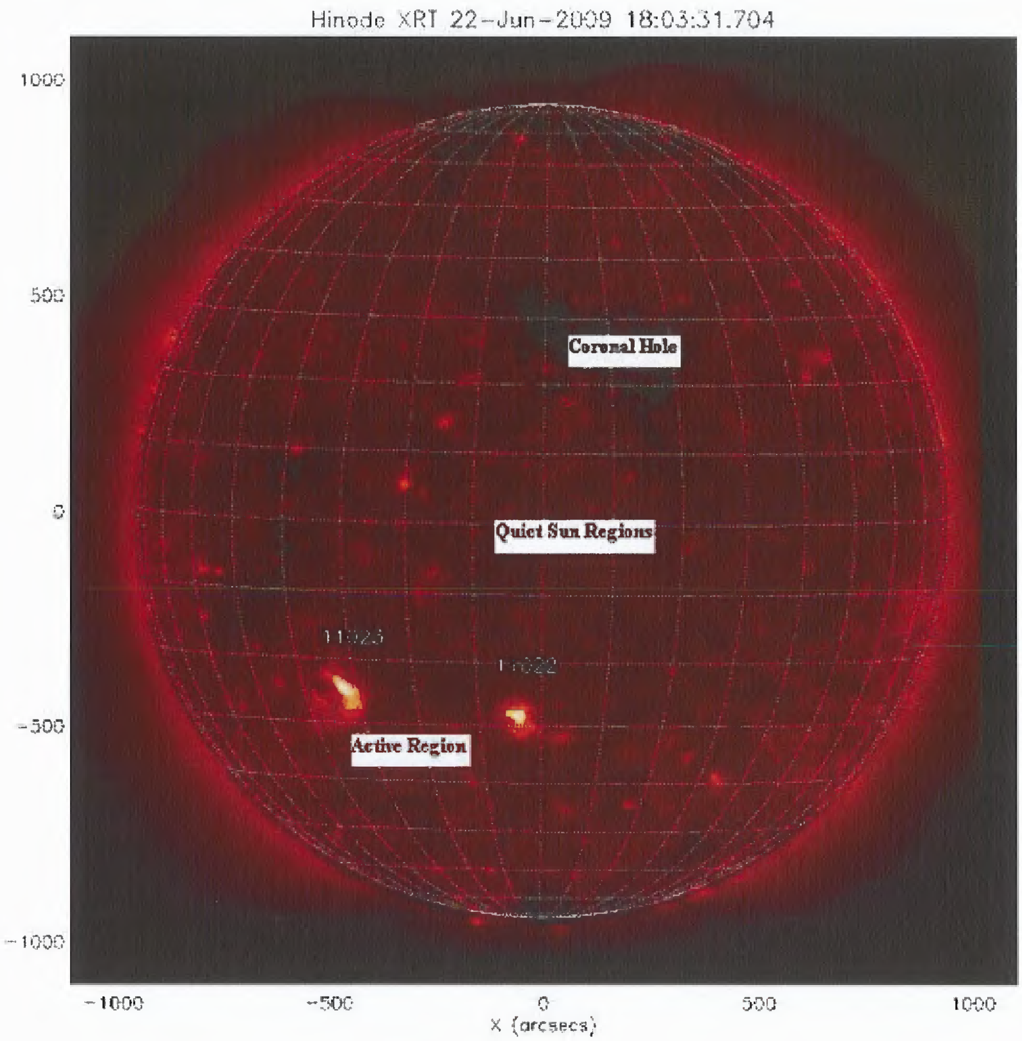

Figure 1.6 The *Hinode* XRT image of solar corona on June 22, 2009 (courtesy of *Hinode* Team). The figure shows the corona of active regions, quiet Sun regions and a coronal hole.

1.4 Magnetism

Magnetism is the key to discovering and understanding the Sun. Solar magnetic fields are mainly produced by the flow of electrically charged ions and electrons in the convection cells. Magnetic fields are present everywhere in the Sun. For example, a steady prominence or limb filament seen floating above the surface of the Sun is balanced and suspended with the tension force of magnetic fields (see Figure 1.7). All levels of solar activity and their space weather effect are related to solar magnetic fields.

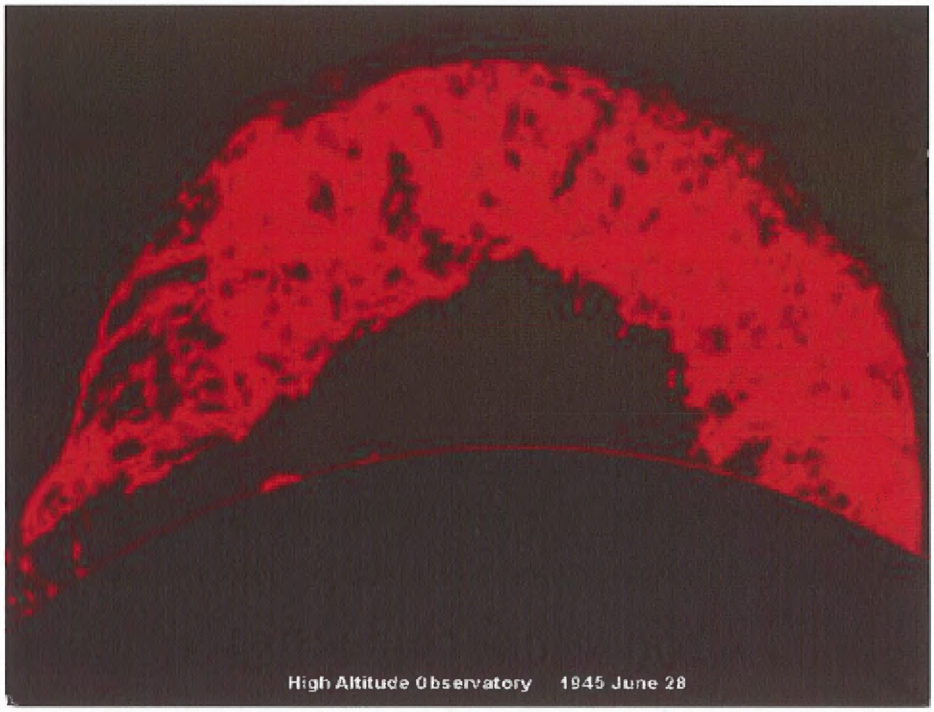

Figure 1.7 A prominence was observed on June 28, 1945 (courtesy of High Altitude Observatory).

During some periods, the Sun's magnetic fields simplify into the form of a magnetic dipole. It can be often represented by so-called potential field. At other times, the field is extremely complex, carrying current (specified by the α, so-called "force-free parameter", which is in general a scalar function of the spatial position $\mathbf{x}$, defined by the force-free magnetic field equation, $\nabla \times \mathbf{B} = \alpha(\mathbf{x})\mathbf{B}$ (Lüst & Schlüter 1954; Sakurai 1981)) which creates a more complex nonpotential field. The potential field resembles a bipolar magnetic field that would result if the magnetic energy reaches the minimum, like the "magnet" field configuration as Figure 1.8. When the Sun's magnetic field becomes nonpotential, the field lines resemble kinked or twisted tubes. The field develops kinks and twists for three reasons: (1) the inner part of the Sun rotates more rapidly than outer layers, (2) equatorial plasma rotates more rapidly than higher latitude plasma, and (3) there is sub-surface convective motion. The rotational differences shear and stretch field lines, and eventually, the field lines become so distorted that the kinks and twists develop.

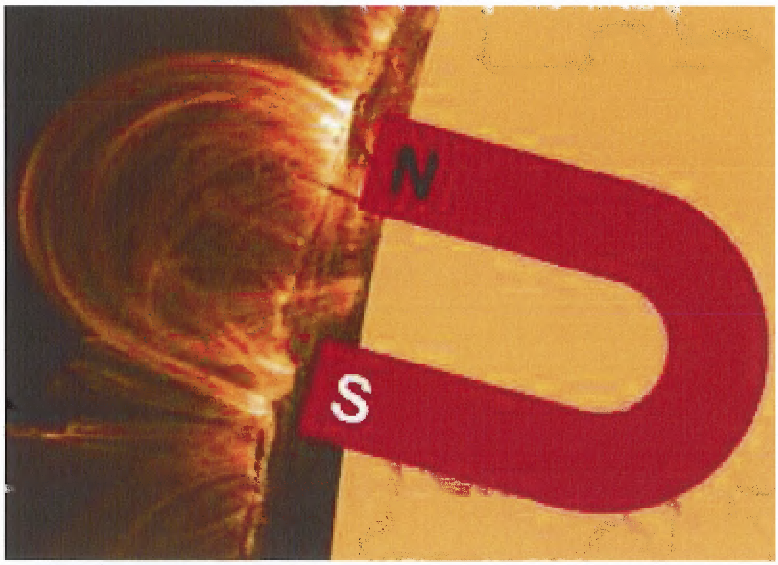

Figure 1.8 The magnet of solar magnetic fields. The original artwork by Randy Russell using an image from NASA's *TRACE* (Transition Region and Coronal Explorer) spacecraft. (courtesy of *TRACE* Team)

The quantitative study of the evolution and motion of the solar magnetic field is a crucial step towards exploring the Sun. Because of the distance between the Sun and Earth, the magnetic field of the Sun can not be detected in a direct manner but rather, remote sensing must be used. To measure the magnetic fields, the Zeeman effect is widely used in contemporary solar observations. The energy levels of atoms in the presence of a magnetic field are split into more than one level. Among the atomic absorption lines interspersed in the black-body continuum spectrum, one can choose certain magnetically sensitive lines (those that show larger splitting in magnetic fields due to their larger Landé g-factor (Landé 1937)) with which to measure circular and linear polarization, in term of, Stokes parameters, I, Q, U, V. The strength and direction of the magnetic field can be determined from the measurement of such polarized signals, using Stokes inversion (Skumanich & Lites 1987). The Stokes parameters, or Stokes vector, are a set of values that describe the polarization state of electromagnetic radiation. They were defined by George Gabriel Stokes in 1852. The four Stokes parameters, I, Q, U, V, can fully describe the states of unpolarized, partially polarized, and fully polarized light. The Stokes parameters are convenient because they are all measurable by remote sensing. Magnetically sensitive lines are more accurate for Stokes measurement, like Sodium or Iron lines. Besides Zeeman effect, the Hanlé effect is another useful tool to diagnose chromospheric magnetic fields, especially the fields in filaments (Faurobert 2000).

Globally, the solar magnetic field evolves with the 11-year sunspot cycle or 22-year magnetic cycle along with the sunspot number. The field is more complicated at solar maximum than at solar minimum as explained by solar dynamo theory see (Stix 1989, and references therein). For an individual active region, its lifetime varies in the range of days to months, and to a large extent depends on its size. At the decay phase, the active region is gradually dispersed by processes of diffusion, convective motions, differential rotation and meridional motion.

Magnetic reconnection is the major process to release the stored magnetic energy in a plasma. Magnetic reconnection describes the process in which magnetic field lines with opposite polarities change their pattern of connectivity. In magnetic reconnection, magnetic field energy is converted to plasma kinetic and thermal energy. For instance, solar flares and CMEs involve a large scale reconnection of solar magnetic flux, partially releasing stored magnetic energy that has been accumulated over a relatively long time. The aurora is another phenomenon due to magnetic reconnection, but in Earth's magnetosphere.

In plasma physics, it is well known that magnetic field lines are "frozen-in" to plasma if the local conductivity is high. Infinitely conductive plasma forbids the direct transport across field lines. Therefore, the question is how magnetic reconnection happens. According to magnetohydrodynamics (MHD) theory, reconnection occurs in the current sheet that is needed to sustain the change in the magnetic field, as formulated in one of Maxwell's equations:

$$\nabla \times \mathbf{B} = \mu \mathbf{J} + \mu \varepsilon \frac{\partial \mathbf{E}}{\partial t}. \tag{1.1}$$

The resistivity of the current sheet allows magnetic flux from either side to diffuse through it, cancelling out flux from the other side at the infinitely thin current sheet. In the presence of the strong current sheet, even a vanishingly small amount of resistivity in such a small volume can become important. Then the central plasma is pulled out by magnetic tension perpendicular to the reconnected magnetic field lines. Therefore, the drop of magnetic pressure pulls more plasma and magnetic flux into the X-point or reconnection point, consequently yielding a self-sustaining process (Priest & Forbes 2000). There are many reconnection scenarios to predict the process with different reconnection speed, e.g. *Sweet-Parker* magnetic reconnection scenario (Sweet 1958; Parker 1957) and *Petschek* magnetic reconnection scenario (Petschek 1964) (see Figure 1.9).

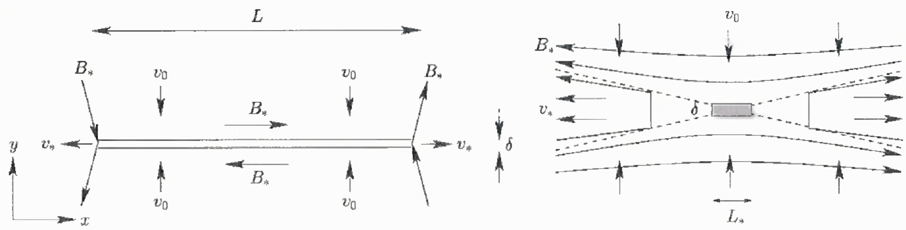

Figure 1.9 The left panel shows the *Sweet-Parker* magnetic reconnection scenario (Sweet 1958; Parker 1957) and the right panel shows the *Petschek* magnetic reconnection scenario (Petschek 1964).

1.5 Coronal Heating

The solar atmospheric temperature and density profiles have been generally known for more than six decades. The profiles are shown in Figure 1.10. However, a key question still remains to be answered is why the temperature of the Sun's corona is millions of kelvins higher than that of the photosphere. It is generally agreed that the heating energy comes from the magnetic fields, but the heating mechanisms do not come to agreement. There are two predominant categories of coronal heating mechanisms (see Table 1.1): wave heating (alternating current, AC model) and magnetic reconnection (or nanoflares) (direct current, DC model) (Klimchuk 2006). However, more and more recent work rules out the wave heating models because of the issues of energy budget (Narain & Ulmschneider 1996), waves penetration the chromosphere (Stein & Nordlund 1991; Bogdan et al. 2003) and energy dissipation in corona (Parker 1991a,b; Collins 1992; Muller et al. 1994; Narain & Ulmschneider 1996).

A nanoflare heating model was proposed by Parker in 1980's (see Parker 1983, 1988). The basic idea is that the unresolved magnetic field lines/strands are stretched and entangled together in the corona by the random motions of photospheric magnetic loop footpoints. The small scale reconnection or nanoflare happens ubiquitously. The

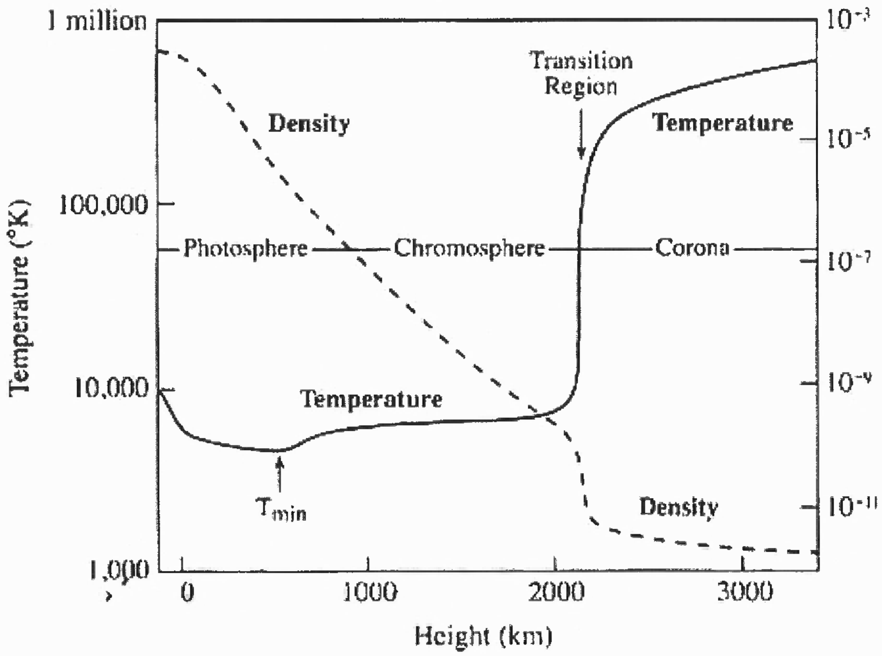

Figure 1.10 The temperature and density profiles of solar atmospheric plasma (Stix 1989).

Table 1.1 Comparison of Coronal Heating Models

DC (reconnection)	AC (waves)
B-field stresses	Photospheric footpoint shuffling
Magneitc reconnections	MHD waves
Nanoflares	*Alfvén* waves and magnetic flux tube waves
Uniform heating	Nonuniform heating

uniform reconnection produces electric current sheets dynamically. The current sheets heat the corona. Based on the recent space-based coronagraph observations and analysis, nanoflare heating mechanism became a promising solution towards the coronal heating problem (Reale & Peres 2000; Warren et al. 2002; Patsourakos & Klimchuk 2006; Klimchuk 2006; Reale et al. 2009), although problem remain.

1.6 Solar Flares

A solar flare is a quick and energetic explosive event of the Sun that can release up to 10^{32} - 10^{33} ergs of energy in minutes. Microflares, in contrast, release $\sim 10^{27}$ ergs and nanoflares are still weaker. The study of solar flares can be traced back to 1850's when Carrington (1859) and Hodgson (1859) scientifically documented the first observed flare independently. Generally, based on the morphology of flaring site, flares can be classified as compact flares and larger, longer-duration two-ribbon flares (Pallavicini et al. 1977; Liu 2007). On the other hand, if one instead looks into the time profile of soft X-ray emission, the flares are divided into two groups: single burst flare and multiple-burst flare. The multiple-burst flares include homologous flares (Waldmeier 1938). If they occur in the same region, they are called successive flares (Liu et al. 2009). If they occur in different active regions, they are called sympathetic flares (Pearce & Harrison 1990). Nevertheless, the explosive events rapidly release the free magnetic energy to heat the coronal plasma and accelerate particles to nearly relativistic velocities towards the interplanetary space and magnetic loop footpoints. Many flare models make specific applications of reconnection in various forms to understand the flare triggering, energy release, and related dynamical processes, such as CSHKP model (Carmichael 1964; Sturrock 1966; Hirayama 1974;

Kopp & Pneuman 1976), emerging flux model (Heyvaerts et al. 1977), flux rope catastrophic model (Forbes & Priest 1995), magnetic breakout model (Antiochos 1998), loop-loop model (Uchida 1980) and tether-cutting model (Moore et al. 2001). Jing et al. (2006) intensively studied the correlation between flare productivity and photospheric magnetic parameters. Their finding supports the close relationship between photospheric magnetic nonpotentiality and flare productivity.

The strong relationship between photospheric magnetic fields and coronal activity, in aspects of coronal heating and solar flares, have been clearly shown. The importance of photospheric magnetic fields is therefore clear. Although a substantial amount work has been done, there is still a need for new research on this topic with the development of new instruments and data analysis techniques. This dissertation aims at the study of the linkage between photospheric magnetic fields and coronal emission.

CHAPTER 2

STATISTICAL CORRELATIONS BETWEEN PARAMETERS OF PHOTOSPHERIC MAGNETIC FIELDS AND CORONAL SOFT X-RAY BRIGHTNESS

2.1 Introduction

It is well-established that the solar magnetic fields play essential role in heating the solar corona (Priest 1990; Browning 1991; Spicer 1991; Cargill 1993; Wolfson et al. 2000). Ultimately, the energy required for the coronal heating should come from the convection motions in or below photosphere (Zirker 1993). The questions of how exactly this energy is transported to the corona and what is the prime mechanism of the coronal heating are still debated. In a broad sense, the heating mechanisms can be classified in two categories (Hollweg 1993; Parker 1988): alternating current (AC) heating (e.g. dissipation of magnetohydrodynamic waves), and direct current (DC) heating (e.g. the dissipation of electric currents through nanoflares). Several recent studies ((e.g. Mandrini et al. 2000)) give preference to 'DC' heating mechanisms.

A poor knowledge of the coronal magnetic field and spectrum of velocities with respect to the magnetic field footpoints makes it difficult to directly identify the exact heating mechanism. Therefore, alternative approaches have been adopted to examine relationships between the coronal brightness (proxy for heating rate) and observable photospheric magnetic field parameters. For example, Golub et al. (1980) and more recently Fisher et al. (1998) quantified the scaling relationships between various "global" magnetic parameters and X-ray luminosity. The best correlation was found between total unsigned magnetic flux and X-ray luminosity (Fisher et al. 1998). The relationship between coronal structures and nonpotentiality of magnetic fields has also been extensively investigated (Metcalf et al. 1994; Falconer et al. 1997; Maeshiro et al. 2005). These studies identified a spatial coincidence between sites of bright coronal X-ray features and strong-sheared magnetic neutral lines (Falconer et al. 1997) suggesting a link between the coronal heating and the nonpotentiality of the magnetic field. Length of the neutral line was also found to be strongly correlated with flare productivity of active regions, e.g. (Jing et al. 2006; Song et al. 2006a,b). Yashiro & Shibata (2001) investigated relationship between thermal and magnetic properties of active regions; the empirical scaling laws between magnetic flux and total thermal energy, and gas pressure and averaged magnetic flux found to be consistent with the Alfvén wave heating model.

Finally, high correlation between soft X-ray flux density and the dissipations of magnetic energy in the photosphere found by (Abramenko et al. 2006b) suggests a link between the energy of random motions of photospheric footpoints of magnetic field lines and the heating of the X-ray corona.

Both AC and DC heating mechanisms require photospheric footpoint motions (Tsiklauri 2005; Klimchuk 2006). Tsiklauri (2005) showed that if the time scale of motions is much shorter than the scale of Alfvén waves that propagate along a coronal loop, the heating should be dominated by the AC heating mechanism; otherwise the DC heating mechanism should prevail. For AC heating mechanism, the footpoint random motions produce Alfvén waves (Kudoh & Shibata 1999; Moriyasu et al. 2004). For DC heating, the motions stress the magnetic field leading to reconnection that releases the energy for heating (Lin et al. 1984; Dennis 1985; Parker 1988; Klimchuk 2006). Thus, in AC-mechanism dominated scenario, one should see a direct relationship between the amplitude of footpoint motions and coronal brightness. In case of DC-mechanism, however, the correlation may be weaker, or even absent, as footpoint motions only serve as a prelude creating favorable conditions for magnetic reconnection; it is the final reconnection that releases the energy and heats the corona. Katsukawa & Tsuneta (2005) showed that the hotter the loops – the lower the magnetic filling factor at their footpoints, which implies that hotter coronal loops could have more room for footpoint motions. This raises an idea to examine a correlation between the coronal X-ray brightness and random velocities of magnetic fields at the photosphere.

This chapter is focused on relationships between X-ray brightness of active regions and several magnetic parameters including properties of random motions of the photospheric magnetic footpoints and the Poynting flux due to these motions. In §2.2, data sets and reduction are presented; in §2.3, the parameters are described, the results and discussion are summarized in §2.4, §2.5, respectively.

2.2 Data Sets and Data Reduction

The data sets used in this study include full disk longitudinal magnetograms observed by the Michelson Doppler Imager (MDI, (Scherrer et al. 1995)) on board the Solar and Heliospheric Observatory (SOHO) and Soft X-ray Telescope (SXT) single-frame desaturated (SFD) composite images on *Yohkoh* (Tsuneta et al. 1991).

Using SOHO/MDI and *Yohkoh* data, the author created two data sets. Data set 1 was used to study the relationship between the X-ray brightness and magnetic parameters, and data set 2 was utilized to study the effects of random motions of photospheric field on coronal heating. The data sets include both (NOAA) numbered active regions (AR) and small well-defined bipoles without NOAA AR number. The MDI data are full disk longitudinal magnetograms observed with 96 minutes cadence and the spatial resolution of 1.98 arc seconds per pixel. The SXT data are 512 $\times$ 512 pixels' images with the spatial resolution of 4.92 arc seconds per pixel (so called, SXT half resolution). The SXT data obtained with AlMgMn-sandwich filter were used only. SXT data were processed following standard *Yohkoh* data reduction procedure.

Data set 1 consists of pairs of full disk MDI magnetograms and SXT images taken from May 1996 to December 1996 around the minimum of sunspot activity cycle. SXT images (in half-resolution and AlMgMn-filter) were selected to be closest in time to MDI magnetograms; the maximum time difference between magnetic and X-ray observations is about 40 minutes. Using these data, total 185 active regions are selected for studying magnetic parameters that can be derived from a single magnetogram: length of strong-gradient magnetic neutral line, L_{GNL}, the magnetic energy dissipation, ε, the unsigned line-of-sight magnetic flux, Φ, and average strong-field gradient across neutral line $< \nabla B_z >$. These parameters will be described in detail in next section. To perform these calculations, the rectangular boxes are manually selected around each active region of interest. The size of a box was determined using both MDI magnetograms and SXT images. The observer selected box size to include the entire magnetic field of active region of interest and the major coronal structure deemed to belong to this region. Figure 2.1 shows examples of active region selections. The size of boxes depends on the size of active region, but the boxes have the same size (in arc seconds) for corresponding MDI-SXT pairs of images. When appropriate, the location of boxes (in SXT images) was adjusted to compensate for a time difference between SXT and MDI observations. The effect due to the box size was estimated that if the box is increased by 10% size, the adjustment to the parameters will be less than 1%. To reduce the errors due to the projection effect, only the regions located near the disk center are selected, i.e. confined within $\pm 40^\circ$ central meridian distance (CMD) and $\pm 35^\circ$ latitude. Figure 2.1 shows MDI magnetogram and SXT X-ray image giving example of two types of regions selected for study: numbered active region (NOAA AR 07986, labelled 1) and small bipolar region (labelled 2) without NOAA AR number.

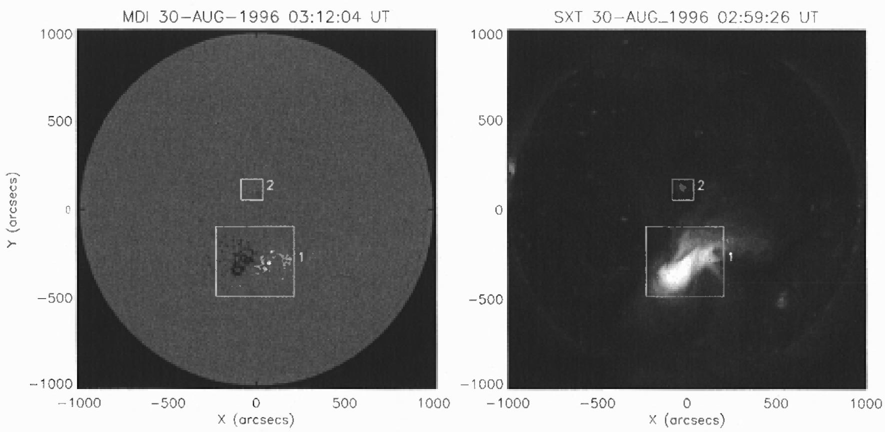

Figure 2.1 Full disk MDI magnetogram (left) observed at 03:12:04 UT on August 30 1996 and (right) full disk SXT image observed at 02:59:26 UT on August 30 1996. On magnetogram, white/black is positive/negative polarity. Box 1 is example of NOAA numbered AR 07986, and box 2 is a well-defined bipole without NOAA number. Figure 2.2 shows enlarged magnetograms for both regions.

Due to the data quality and the sample quantity, the author extended data set 1 to get another one named data set 2. Data set 2 consists of 169 active regions selected in a similar way as described above using full disk observations from May 1996 to September 1997. In this data set, for each SXT image the author selected five consecutive magnetograms with observing cadence of 96 minutes. The sequence of MDI magnetograms spans about 8 hours and is centered at around the SXT image observing time. This data set is used to compute the photospheric horizontal velocities via local correlation tracking (LCT) technique and the Poynting flux.

The original intent was to use the same time interval for both data sets. However, since the growing regions are excluded from the second data set, the author had to extend the time period to September 1997 to get enough samples.

The regions selected for both data sets are mature and non-flaring. The maturity (i.e. lack of rapid expansion) was judged on the basis of visual inspection of selected consecutive magnetograms. For NOAA numbered regions the maturity was additionally established using data from the *Solar Geophysical Data* (SGD) reports. To avoid possible effects of flares on X-ray brightness (Pevtsov & Kazachenko 2004, e.g.), the SGD reports are used to select non-flaring periods of active regions evolution.

2.3 Parameters

In the present study both extensive (integrated over area of box) and intensive (average over area) parameters are determined. The author expects that extensive quantities are affected by the size of active regions, and intensive quantities should be independent of AR size.

2.3.1 Coronal Brightness

Coronal X-ray brightness (L_B) was computed using intensity derived from the SFD images (in Data Numbers, DN):

$$L_B = \sum_{i=1}^{n} \ell_B(i) dA, \tag{2.1}$$

where dA is a pixel area, ℓ_B is X-ray brightness of i^{th}-pixel, and n is the total number of pixels.

To calculate X-ray brightness, the author selected pixels which brightness exceeds 3σ noise level above average intensity. For each SXT image, the author manually selected the darkest area and calculated average intensity (I_{AVG})in that area and its standard deviation (σ). As the selection of darkest area is subjective, the author repeated this procedure several times and averaged the results to get the noise level. Furthermore, insignificant difference is found in noise level due to subjective selection (within $\pm$ 5%).

2.3.2 Photospheric Magnetic Parameters

Data set 1 was used to compute several parameters of the magnetic field. In the following, B_x, B_y, and B_z represent components of magnetic field in Cartesian coordinate system with z along line-of-sight, and x,y situated in image plane. However, as the author selected active regions to be near disk center, the axes of this coordinate system are close to true vertical and horizontal directions in respect to solar surface.

(1) Length of magnetic neutral lines with strong-gradient magnetic field, L_{GNL}:

$$L_{GNL} = \sum_{i=1}^{n} i \, dl, \tag{2.2}$$

where , dl is linear (deprojected) pixel size, and summation is performed over the pixels satisfying $\nabla B_z > 50$ Gauss per Mm^{-1} condition, and $\nabla B_z = \sqrt{\left(\frac{dB_z}{dx}\right)^2 + \left(\frac{dB_z}{dy}\right)^2}$.

L_{GNL} was first introduced by Falconer et al. (2003) as a measure of nonpotentiality of active regions. Its relationships with CMEs and flare productivity have been explored by several researchers (e.g. Falconer et al. 2003; Song et al. 2006b; Jing et al. 2006). And

Wang et al. (2006) investigated the strong linear correlation between magnetic shear and magnetic gradient along the neutral lines. Although the exact functional dependence between non-potentiality and length of neutral line is not well-established, L_{GNL} was used in several previous studies as a measure of non-potentiality. This approach is adopt in order to be able to compare the findings with the results of these published papers.

Unlike other parameters, which intensive form was computed as area-average of extensive parameter, the author calculated area-averaged gradient of magnetic field (<grad B_z >) as intensive form of L_{GNL}. Similar to L_{GNL}, only pixels with ∇B_z gradient exceeding 50 G Mm^{-1} were used to compute $< \nabla B_z >$.

(2) magnetic energy dissipation rate:

$$\varepsilon = \sum_{i=1}^{n} \varepsilon(B_z)\, dA, \tag{2.3}$$

where $\varepsilon(B_z) = \left(6\left(\left(\frac{dB_z}{dx}\right)^2 + \left(\frac{dB_z}{dy}\right)^2\right) + 4\left(\frac{dB_z}{dx}\frac{dB_z}{dy}\right)\right)$.

This parameter was introduced by Abramenko et al. (2003), (see also Jing et al. (2006)) as a measure of degree of intermittency of the magnetic field and as a proxy for the overall flare productivity of active regions. The auther refer the reader to these previous papers to an additional discussion of this parameter.

(3) unsigned longitudinal magnetic flux Φ:

$$\Phi = \sum_{i=1}^{n} |B_z| dA. \tag{2.4}$$

Unsigned magnetic flux has been previously shown to have strong correlation with L_B (e.g. Schrijver et al. 1985; Fisher et al. 1998).

2.3.3 Footpoint Random Velocity

The data set 2 was employed to calculate velocities of photospheric motions of magnetic fluxes and the Poynting flux.

The local correlation tracking (LCT) technique was originally developed by November & Simon (1988) to determine transverse displacements of solar features. For this study, the author adopt the LCT method which was widely used to measure the photospheric velocity fields in more recent studies (Chae 2001; Chae et al. 2001, 2004; Moon et al. 2002a,b). This LCT code has the ability to compensate (or eliminate) the effects due to the solar photospheric differential rotation. The auther refer the reader to these articles for further details on the LCT method.

In general, the calculation errors of an LCT routine increase significantly when tracking weak magnetic features. For this study the author chooses to track only pixels with magnetic flux larger than 50 G. Apodizing window function for LCT was selected to be a Gaussian with FWHM of 10 arc sec. These selections are based on previous applications of the method in order to reduce the noise without loss of ability to track small displacements.

For each active region (data set 2), the transverse displacements of flux elements were determined using a sequence of five successive longitudinal magnetograms as described in Section 2.2. Magnetograms were taken with 96-minutes cadence. The whole sequence covers 8-hour time interval centered at the time of corresponding SXT observation. Assuming that the detectable displacement is about one pixel, the time cadence (96 minutes) and pixel size (2 arc sec) lead to conclusion that the data would not allow to measure velocities smaller than $\approx$ 250-300 m/s. However, the employed LCT code has an ability to measure sub-pixel displacements, which translates to velocities of $\approx$ 100 m/s.

Further details on sensitivity of the LCT method are provided in Appendix. Figure 2.2 gives examples of horizontal velocity maps for two active regions shown in Figure 2.1.

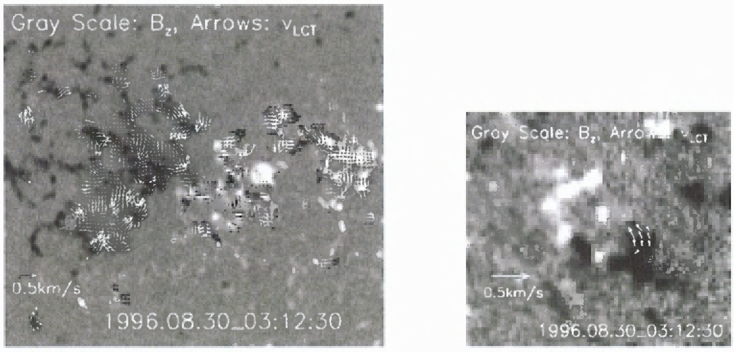

Figure 2.2 Magnetograms (grey scale, white/black is positive/negative polarity) and transverse velocity field maps (white/black arrows) of two active regions. Left panel corresponds to box 1 (435 $\times$ 391 arc seconds) and right panel corresponds to box 2 (139 $\times$ 122 arc seconds) on Figure 2.1.

For each sequence of five successive magnetograms, the four transverse velocity maps are obtained as output of LCT routine. Each transverse velocity map was used to calculate a single number, a random velocity:

$$V_{rdm} = \sqrt{\sigma_x^2 + \sigma_y^2}, \tag{2.5}$$

where $\sigma_{x,y}$ are standard deviations of V_x and V_y velocities determined by LCT.

2.3.4 Poynting Flux

Energy flux from the photosphere due to footpoint motions can be expressed as the Poynting flux (Parker 1979, 1988; Dahlburg et al. 2005; Abramenko et al. 2006b):

$$F = -\frac{1}{4\pi} \cdot B_z \cdot \mathbf{B_h} \cdot \mathbf{V_h} \tag{2.6}$$

here B_h is the horizontal component of the magnetic field. As only longitudinal magnetograms are used, the author makes additional assumption that $|B_h| \sim |B_z|$, and use the following equation as a proxy for the Poynting flux:

$$E = \frac{1}{4\pi} \sum_{i=1}^{n} |V_h| \cdot B_z^2, \tag{2.7}$$

where $V_h = [(V_x - \langle V_x \rangle)^2 + (V_y - \langle V_y \rangle)^2]^{\frac{1}{2}}$.

Replacing B_h with B_z for the purpose of calculating the Poynting flux seems to be reasonable in case of magnetic fields with intermediate inclinations. However, for extreme inclinations (i.e. when magnetic field is purely vertical or horizontal), this assumption may either overestimate or underestimate the Poynting flux. The author expects that averaging over large area of magnetograms may help to cancel out the effects of over-/under-estimation. Ultimately, to test the validity of the assumption would require high resolution full disk vector magnetograms, which are not available at the time of this study.

2.4 Results

2.4.1 Coronal Brightness versus Magnetic Parameters

Using data set 1, the author calculated linear (Pearson) correlation coefficients (LCCs) between the soft X-ray brightness, L_B and three photospheric magnetic parameters: the length of magnetic neutral line, L_{GNL}, energy dissipation rate, ε, and magnetic flux Φ. Figure 2.3 shows scatter plots of averaged magnetic and X-ray quantities, and Figure 2.4 presents correlations between the integrated quantities.

For area-averaged parameters (Figure 2.3), the LCCs between the X-ray brightness

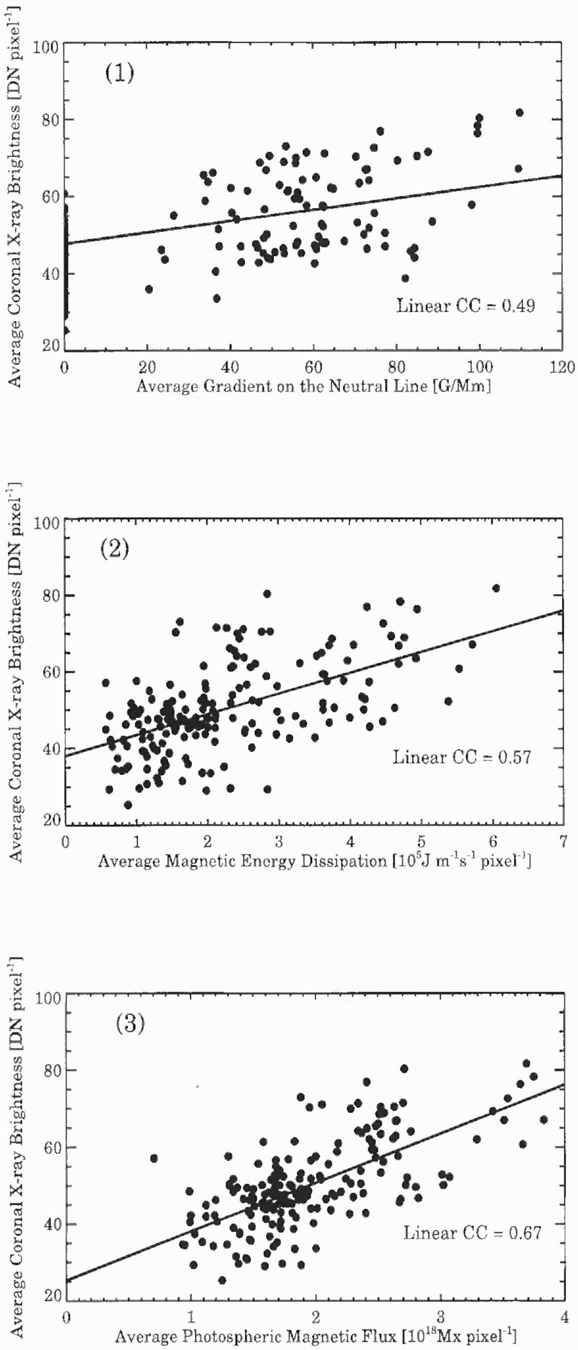

Figure 2.3 Scatter plots of area-averaged parameters showing average coronal X-ray brightness vs. (a) area-averaged gradient of magnetic field, $< \nabla B_z >$, (b) averaged energy dissipation, $< \varepsilon >$, and (c) averaged photospheric magnetic flux, $< \Phi >$. Solid lines show first degree polynomial fit to the data. Linear correlation coefficient (CC) is provided for each pair of variables.

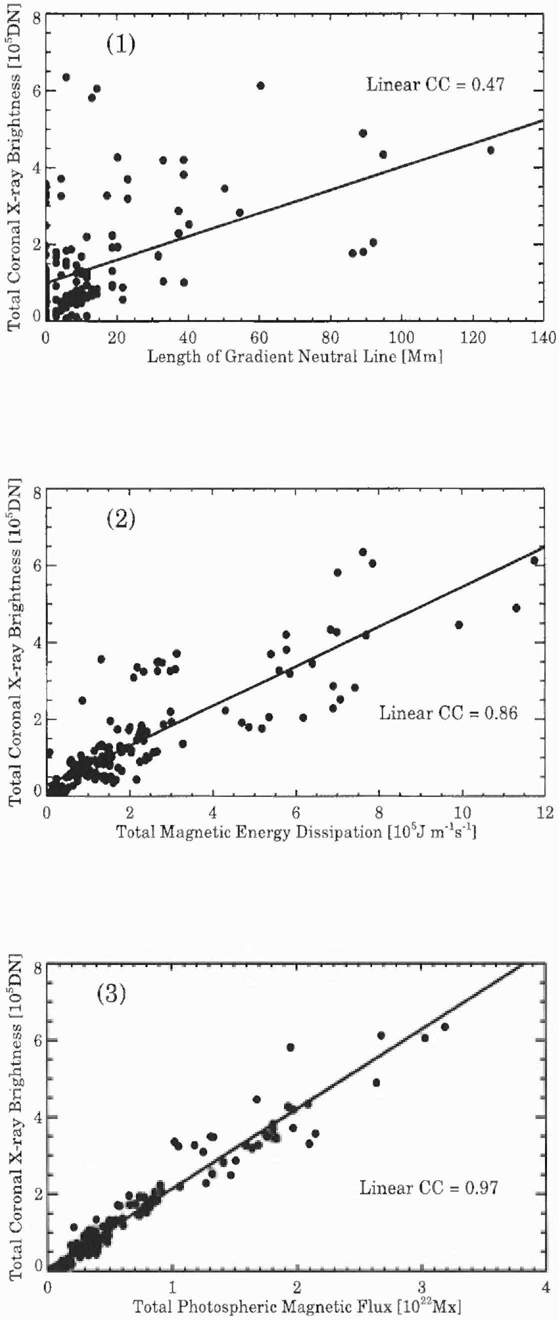

Figure 2.4 Scatter plots of area-integrated parameters showing dependence of total coronal X-ray brightness as function of (a) length of the neutral line with field gradient exceeding 50 G/Mm, L_{GNL}, (b) total energy dissipation, ε, and (c) total unsigned photospheric magnetic flux, Φ. Solid lines show first degree polynomial fit to the data. Linear correlation coefficient (CC) is provided for each pair of variables.

and magnetic measures are: 0.49 ($<\nabla B_z>$), 0.57 ($<\varepsilon>$), and 0.67 $<\Phi>$). For integrated parameters (Figure 2.4), the correlations are: 0.47 (L_{GNL}), 0.86 (ε), and 0.97 (Φ).

The length of high-gradient magnetic neutral line and the mean magnetic gradient along the neutral line, appears the most weakly correlated with the coronal brightness as compared with two other parameters.

Correlation between the magnetic energy dissipation and the soft X-ray luminosity (Figures 2.3, 2.4, middle panels) is higher than that for the gradient along the neutral line (compare top and middle panels in Figures 2.3 and 2.4).

Correlation between the unsigned magnetic flux of active region and the X-ray luminosity was found to be the highest in this study (Figure 2.3, 2.4, bottom panels), which is in a good agreement with earlier findings, e.g. Fisher et al. (1998). Extremely high correlation (LCC=0.97) between the total unsigned flux and the total X-ray flux is rather due to the size of active regions; the correlation between area-averaged parameters is weaker(LCC=0.67).

2.4.2 Coronal Brightness vs. Random Velocity

Photospheric footpoint random motions are derived as described in Section 2.2 using subset of 169 active region (data set 2). The speed varies between 0.08 to 0.16 km/s, in general agreement with previous studies by (Title et al. 1987, 1992; Welsch et al. 2004); averaged horizontal velocity of magnetic regions is about 0.1 km/s.

Figure 2.5 shows the scatter plot of average horizontal velocities, V_h of the photospheric random motions versus average coronal X-ray brightness. Figure 2.6 shows the correlation between average unsigned magnetic flux and V_h. There is no correlation between the strength of the photospheric magnetic field and the photospheric motions of magnetic concentrations. Thus, at the level of the measurements there is no indication that stronger magnetic field might suppress random motions of magnetic footpoints. Equally, there is no correlation between velocities of random motions at the photosphere and X-ray brightness of corona.

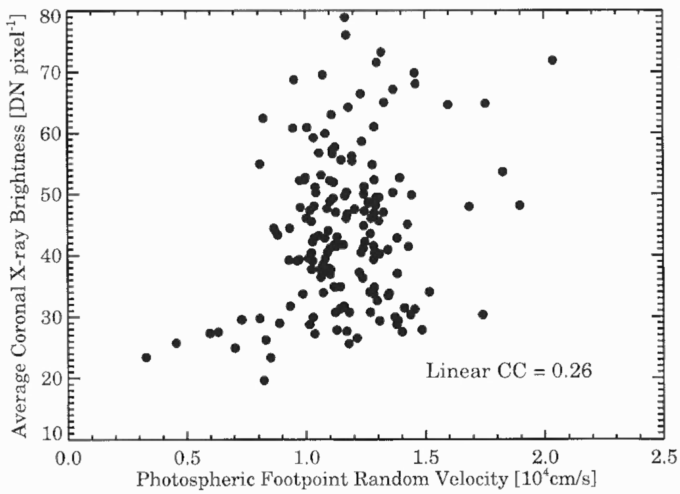

Figure 2.5 Average coronal X-ray brightness vs. photospheric random motions.

2.4.3 Coronal Brightness vs. Poynting Flux

Figure 2.7 is a correlation plot between the X-ray brightness and the Poynting flux, calculated by Equation (7) (also based on data set 2). Both area-integrated and area-averaged parameters show good, near linear relationship. It appears that in two areas, $LogE < 6.7$ and $LogE > 7.6$, the relation E vs. L_X flattens. These thresholds, identified by the vertical dashed lines, are clearer in Figure 2.7a. Although the number of data points in these flat

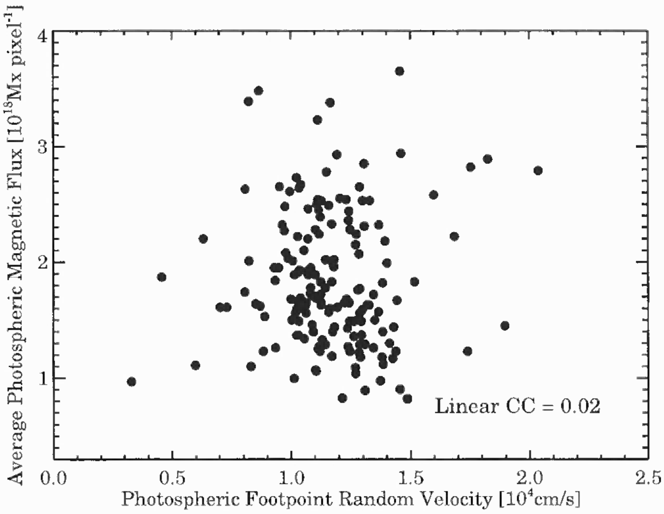

Figure 2.6 Averaged photospheric magnetic flux as function of the photospheric random motions.

areas is small, they may be an indication of real deviation from otherwise linear relationship between Poynting flux and X-ray brightness. The point below $LogE = 6.7$ may be due to limited sensitivity of SXT/*Yohkoh* to a low X-ray fluxes. This might also be effect of truncation error, as SFD images store information in the logarithmic scale. The threshold at $LogE = 7.6$ might indicate a possible saturation of X-ray brightness (i.e. putting more energy to the corona via photospheric random motions might not increase coronal brightness anymore).

In both instances, the number of data points in these outliner areas is too small to be certain that they are real. Further investigations are needed to confirm their presence. In this study, the author excluded data points lying outside of vertical dashed lines from calculation of linear correlation coefficients.

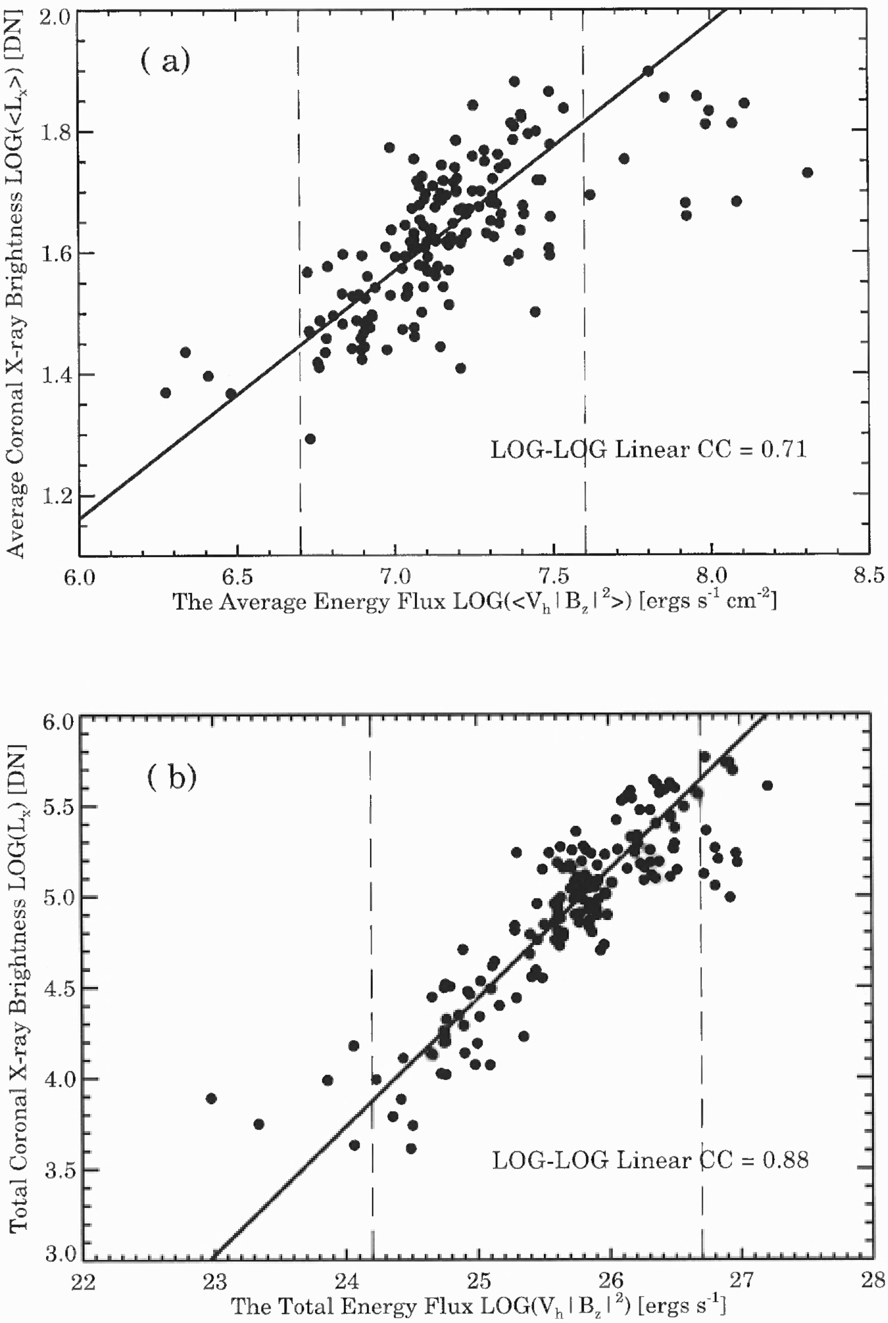

Figure 2.7 Area-average (a) and area-integrated (b) scatter plots showing the LOG-LOG correlation between Poynting flux and coronal X-ray brightness. Solid lines show first degree polynomial fit to the data. Vertical dashed lines outline the data used to calculate linear fits and correlation coefficients (see text).

Linear correlation is higher for area-integrated (E and L_X) parameters (LCC=0.88), and it is slightly lower, LCC=0.71, for area averages. This strong correlation suggests that the X-ray coronal brightness scales with the energy of the photospheric motions of corresponding magnetic concentrations. Figure 2.7a shows that the Poynting flux supplies about $10^{6.7} - 10^{7.6}$ ergs $cm^{-2}s^{-1}$, which is sufficient for coronal heating (according to Withbroe & Noyes (1977); Narain & Ulmschneider (1996); Schrijver et al. (2004); Klimchuk (2006) energy supply to the corona above active region should be about 10^7 ergs $cm^{-2}s^{-1}$).

2.5 Conclusions and Discussion

Based on the analysis of soft X-ray luminosity and line-of-sight magnetograms for more than 160 active regions, the following conclusions are drawn:

1) The best observed correlations between the averaged (over an active region area) soft X-ray brightness and magnetic field measures were found for the Poynting flux density (LCC=0.71) and for the total unsigned magnetic flux density (LCC=0.67).

2) The averaged values of magnetic gradient across strong-field neutral line $< \nabla B_z >$, and of magnetic energy dissipation, $< \varepsilon >$, showed lower correlations with $< L_B >$(LCCs are 0.49 and 0.57, respectively).

3) The averaged values of the horizontal velocities of random motions of magnetic features, determined by the local correlation tracking routine, did not show any correlations with neither the X-ray brightness density nor the total unsigned magnetic flux density (LCCs are 0.26 and 0.02, respectively).

4) The correlations between the total X-ray flux and the integrated magnetic parameters are 0.47, 0.86, and 0.97 for the length of strong gradient neutral line, total magnetic

energy dissipation and total unsigned magnetic flux, respectively.

5) The magnitude of the Poynting flux, which describes the energy input into the corona due to random footpoint motions in the photosphere, ranges between $10^{6.7}$ and $10^{7.6}$ ergs $cm^{-2}s^{-1}$ for the majority of active regions in the data set.

The length of high-gradient magnetic neutral line could serve as a proxy of active region's magnetic non-potentiality (Falconer et al. 2003; Jing et al. 2006; Song et al. 2006b). In this sense, the author may conclude that a number of active regions exhibit zero non-potentiality, however the X-ray flux from these nearly potential regions is of the same magnitude as that for others, significantly non-potential regions in this data set. This behavior suggests that the overall non-potentiality (large-scale electric currents) does not play a significant role in heating the entire active region corona. On the other hand, non-potentiality might be important in a localized heating, e.g. in vicinity of magnetic neutral line.

Indeed, non-potentiality strongly correlates with the flare productivities (Jing et al. 2006). Song et al. (2006a) also found that non-potentiality is more important parameter for flare productivity than the unsigned magnetic flux. Table 1 shows that the non-potentiality has stronger correlation with flare productivity than magnetic flux, while unsigned magnetic flux shows much stronger correlation with X-ray brightness of active region. Then one may suggest that length of neutral line may reflect localized properties that are important for localized heating and flares, while total unsigned flux serves as a proxy for heating of entire active region corona.

A possible explanation for significant correlation between the magnetic energy dissipation and the X-ray parameters may be a fact that the magnetic energy dissipation is not only a measure of non-potentiality (Jing et al. 2006), but also is a proxy for the intensity of turbulent motions in the photosphere and beneath (Abramenko et al. 2006). This provides us an argument in favor of the strong relevance of photospheric turbulent motions to the heating of the corona above active regions. The relationship between the magnetic energy dissipation and parameters of the soft-X-ray luminosity was also analyzed by Abramenko et al. (2006) for a time period near the solar maximum. The authors reported a slightly higher correlation between the averaged X-ray flux and averaged dissipation: LCC= 0.68 versus LCC=0.57 obtained here. Whether such difference is the result of data selection, or of the solar cycle influence, is a subject for future investigations.

A strong correlation between the total unsigned magnetic flux and the total X-ray flux is a rather expected result. However, a high correlations between the area-averaged fluxes may imply that the surface X-ray brightness of active regions depends on their total magnetic flux (and hence, of the size). In other words, a line-of-sight column of coronal plasma in larger active regions tends to be brighter than a similar column in smaller regions. This is somewhat unexpected, as none of existing coronal heating mechanisms have intrinsic dependence on active region size. What could be a possible explanation of such

Table 2.1: Result Comparison.

	L_{GNL}	ε_{tot}	Φ_{tot}
Flare Index (FI_{SXR})[a]	0.68	0.72	0.65
Coronal Brightness (our result)	0.47	0.86	0.97

[a]as calculated by Song et al. (2006a).

dependency? The solar atmosphere is optically thin everywhere in the X-ray corona. The author suggests, however, that there are local variations of optical thickness even within a single active region. The optical thickness is determined by several parameters including size of coronal volume filled by the magnetic fields. Due to larger size, magnetic fields in larger active regions will naturally extend to larger heights, thus filling up larger volume. This will increase the optical thickness, and hence, a line-of-sight column of plasma in larger regions may appear brighter. The author believes that this increase in optical thickness might have additional effect of strengthening the correlation between the unsigned magnetic flux and X-ray brightness of active regions.

Muller et al. (1994); Berger & Title (1996) showed the photospheric random velocity is in the order of 1 km/s that is faster than the results of the study. The higher velocities are obtained is because of the combination of tracking displacements in G-band bright points due to granular flows and effects from the solar differential rotation. However, Welsch et al. (2004) tracked horizontal displacements of magnetic flux elements using LCT and IVM vector magnetograms. Although original IVM magnetograms are 1.1 arc sec per pixel, the data were re-mapped to 1.77 arc sec per pixel. These re-mapped magnetograms are close in resolution of MDI full disk magnetograms used in this study (1.98 arc sec per pix). The Figures 2.5 and 2.6 of Welsch et al. (2004) suggest that a typical velocities of horizontal displacements are somewhere around 0.1 km/s, in agreement with this findings. The results of Welsch et al. (2004) also provide indirect support to the claim that LCT is capable of measuring a sub-pixel displacements (they measure displacements as small as 80 m/s).

The present study did not reveal any correlation between the averaged velocities in the photosphere and the X-ray brightness. However, this inference does not imply that such a correlation cannot exist. The author understands that the (low spatial and temporal resolution) data may not be optimal to determine the motions involved in the coronal heating. A strong relevance of the photospheric random motions to the heating of the corona follows from revealed here statistical dependence of the X-ray brightness from the parameters, that are intrinsically related to the intensity of turbulent motions, namely, from the Poynting flux and magnetic energy dissipation. The estimation shows that the Poynting flux is quite sufficient to heat the corona above the majority of studied active regions. Higher resolution observation can result in even higher Poynting flux.

As for the possible mechanisms for the coronal heating (AC heating versus DC heating), both of them rely on the random motions in the photosphere. In this sense, the results show that both of them may be plausible in active regions, however they may operate at different spatial and temporal scales. This problem requires high temporal and spatial resolution data, along with elaboration of new approaches to obtain the distribution of velocities in the photosphere.

Appendix: LCT Technology Test

To test the LCT method, an artificial image containing several sources of different size is created(see Figure 2.8). All features are 2-D Gaussian profiles with different maxima ranging between 100 and 900 Gauss. A normally distributed random noise of 14 G was added to the image. The original image had simulated spatial resolution of 0.2 arc second per pixel. Next all sources were displaced by 0.2 arc second in the same (horizontal) direction. The original and displaced images were serially averaged to simulate larger pixelation (from 0.2 arc second to 2 arc second) and subjected to a LCT. The resulting shift detected by LCT was compared with original shift. The results show that even with significant averaging, the LCT allows to detect original shift with less then 6% uncertainty (see Figure 2.9). This exercise also confirms that LCT cannot detect displacements of some faint features (for example, feature in the small box area, Figure 2.8), if the maximum amplitude of a feature is around the threshold of 80 Gauss.

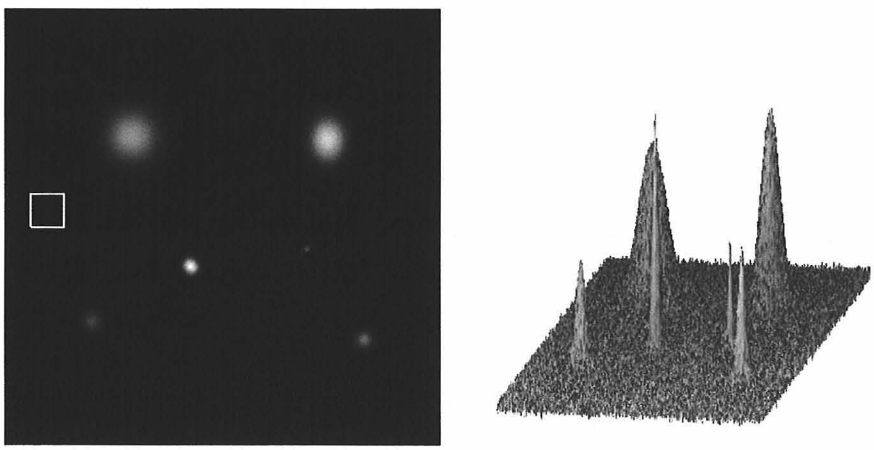

Figure 2.8 It shows the artificial images. The left panel is the artificial image, the right panel is the 3-D profile. All the features are Gaussian distributions. The random noises with magnitude of 14 Gauss are added.

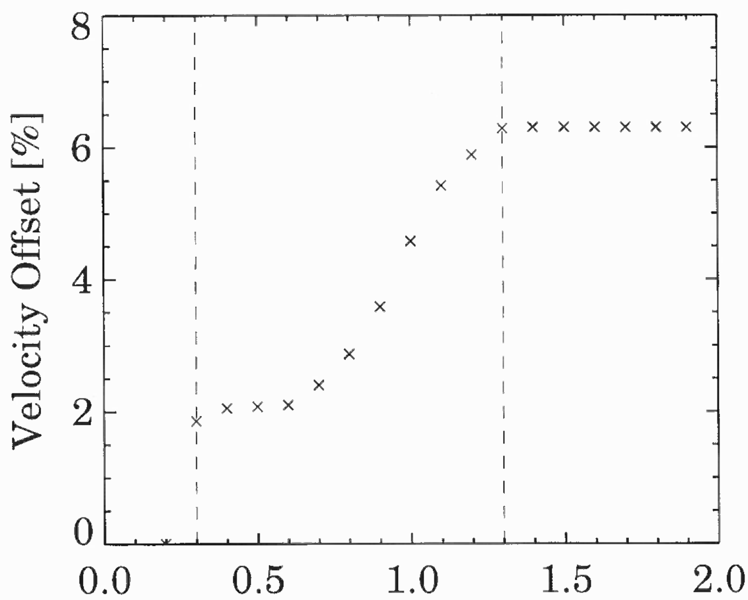

Figure 2.9 The average velocity offset vs. the image pixel size. Although the pixel sizes are different, the displacements are exactly same as 0.2 arc second (see text).

CHAPTER 3

FREE MAGNETIC ENERGY AND FLARE PRODUCTIVITY OF ACTIVE REGIONS

3.1 Introduction

The solar magnetic field is the source of most (if not all) solar energetic events such as flares and coronal mass ejections (CMEs). Since the coronal magnetic field cannot be precisely measured at present except in a few special cases (e.g. Gary & Hurford 1994; Lin et al. 2004), the efforts to identify the magnetic properties important for flare/CME production have been made almost exclusively with parameters derived from the photospheric magnetic fields. Generally speaking, these magnetic parameters quantify the size and/or the topological complexity of an active region. Several recent instances are: the total unsigned magnetic flux $\Phi = \int |B_{rad}| dA$ where B_{rad} is the radial component of the magnetic field and the integral is performed over the field of view (FOV) A (Barnes & Leka 2008; Song et al. 2009); the amount of magnetic flux close to the strong-gradient magnetic polarity inversion line (PIL; Schrijver 2007); the length of the high-gradient and high-sheared PIL (Falconer et al. 2003); the total magnetic dissipation (Jing et al. 2006; Song et al. 2009); the effective connected magnetic field (Georgoulis & Rust 2007); and the photospheric excess energy (Leka & Barnes 2003; Barnes & Leka 2008). In particular, the photospheric excess energy E_{pe} measures the difference between the observed and the potential fields at the photospheric surface, i.e., $E_{pe} = \int \frac{B_o^2}{8\pi} dA - \int \frac{B_p^2}{8\pi} dA$, where the superscripts o and p represent the observed field and the potential field, respectively. Note that E_{pe} is not a true magnetic energy stored in an active region, since the integral is computed only at the photospheric surface and not throughout the coronal volume. Although all these photospheric magnetic parameters have been reported to bear certain relation to flare occurrence, the limitations of using the state of the photospheric magnetic fields to distinguish between flare-active and flare-quiet regions and to forecast flare occurrences have been addressed (Leka & Barnes 2007).

Compared to those photospheric magnetic parameters, free magnetic energy E_{free} derived from 3-dimensional (3-D) coronal magnetic configuration over an active region seems to be a more intrinsic physical parameter related to the flare/CME productivity of an active region. E_{free} quantifies the energy deviation of the coronal magnetic field from its potential state. Since currently the most sophisticated and accurate methods to model the coronal magnetic field are nonlinear force-free (NLFF) field extrapolation methods, E_{free} can be estimated by:

$$E_{free} = E_N - E_p = \int \frac{B_N^2}{8\pi} dV - \int \frac{B_p^2}{8\pi} dV, \tag{3.1}$$

where V is the volume of the computational domain from photosphere to corona, and the superscripts N and p represent the NLFF field and the potential field, respectively. E_{free} calculated in this way is regarded as the upper limit of the energy that is available to power the flares/CMEs. Knowledge of the amount of E_{free} and its temporal variation associated with flares/CMEs is important to the understanding of energy storage and release processes in active regions. Progress in this research area has been made recently by, e.g., Bleybel et al. (2002); Régnier et al. (2002); Régnier & Canfield (2006); Guo et al. (2008); Thalmann & Wiegelmann (2008); Thalmann et al. (2008); Jing et al. (2009a).

On the other hand, solar flares are classified as X, M, C or B according to their peak soft X-ray (SXR) flux, as measured by the *Geostationary Operational Environmental Satellite* (GOES) and recorded in the NOAA Space Environment Center's solar event reports. The peak SXR flux of X-, M-, C- and B-class flares is of 10^{-4}, 10^{-5}, 10^{-6} and 10^{-7} W m^{-2} magnitude order, respectively. As proposed by Abramenko (2005), the flare productivity of an active region can be measured by the SXR flare index (FI; hereafter) which counts the X-, M-, C- and B-class flares by different weights. The weight of each class is 10 times stronger than the succeeding one, with X-class flares having a weight of 100 in units of $10^{-6}Wm^{-2}$. I.e.,

$$FI = (100 \times \sum_{\tau} I_X + 10 \times \sum_{\tau} I_M + 1 \times \sum_{\tau} I_C + 0.1 \times \sum_{\tau} I_B)/\tau \qquad (3.2)$$

where τ is the length of the time window, usually measured in days, and I_X, I_M, I_C and I_B are GOES peak SXR flux of X-, M-, C- and B-class flares produced by the given active region within the time window τ. In other words, the FI measures an active region's daily average flare production within the time window. In this study, the author used three different time windows ranging from the time of the analyzed magnetogram to 1, 2 and 3 subsequent days after that time, i.e., FI_{n-day} where n=1, 2, 3.

The goal of this chapter is two-fold. First, the author examined the statistical correlation between free magnetic energy E_{free} derived from 3-D NLFF fields and flare index measured within the 1-, 2- and 3- time windows FI_{n-day}. This correlation has not been explored before to the author's knowledge. Secondly, the author studied the temporal variation of E_{free} for both flare-active and flare-quiet regions. With the advances in the high-resolution vector-magnetographic capabilities of the *Hinode* spacecraft (Kosugi et al. 2007) and the computational capabilities of NLFF field extrapolation, the author is presently in a good position to explore these issues. The author anticipated that this study will help us disclose the energy storage and release mechanism of flares, and perhaps even provide a tool to forecast flares.

3.2 Data Processing and NLFF Field Extrapolation

This study requires extrapolating the 3-D NLFF coronal fields from the photospheric boundary. The photospheric vector magnetograms, obtained by the Spectro-Polarimeter (SP) of the Solar Optical Telescope (SOT; Tsuneta et al. 2008) on board *Hinode*, are used as the boundary conditions. The SOT-SP obtains Stokes profiles of two magnetically sensitive Fe lines at 630.15 and 630.25 nm with a sampling of 21.6 mÅ. The polarization spectra is inverted to the photospheric vector magnetograms using an Unno-Rachkovsky inversion based on the assumption of the Milne-Eddington atmosphere (e.g., Lites & Skumanich 1990; Klimchuk et al. 1992).

As the author discussed in the previous study (Jing et al. 2009a), the 180° azimuthal ambiguity in the transverse magnetograms is resolved using the "minimum energy" method that is the top-performing automated method among state-of-art algorithms in this area (Metcalf et al. 2006). This method uses the simulated annealing algorithm to minimize a function $|J_z| + |\nabla \cdot \mathbf{B}|$, where the former is the vertical electric current density and the latter is the field divergence (Metcalf et al. 1994). The projection effect is removed for those magnetograms which were observed far from the disk center.

The NLFF field extrapolation endeavors have been plagued by the problem that the photospheric magnetic field, which has a plasma-β of the unity order, does not satisfy the force-free condition (Gary 2001). To find suitable boundary conditions for the NLFF field modelling, the author has to preprocess the measured photospheric magnetograms by using a preprocessing scheme developed by Wiegelmann et al. (2006). This preprocessing scheme removes non-magnetic forces and torques from the boundary and approximates the photospheric magnetic field to the low plasma-β force-free chromosphere. In an effort to test the performance of the preprocessing procedure, the author compared the unpreprocessed and preprocessed SOT-SP photospheric line-of-sight (LOS) magnetogram B_z of AR NOAA 10960 with the co-aligned chromospheric LOS magnetogram. The chromospheric magnetogram was obtained by the Vector SpectroMagnetograph (VSM) instrument located on the Synoptic Optical Long-term Investigations of the Sun (SOLIS; Keller & Nso Staff 1998). SOLIS/VSM produces spectroheligram of HeI line at 1083.0 nm, photospheric LOS and vector magnetograms of Fe line at 630.2 nm, and chromospheric LOS magnetograms of CaII line at 854.2 nm line. The latter is used here for comparison. The comparison is made on a pixel-by-pixel basis and the scatter plots are shown in Figure 3.1. As seen from this figure, the linear correlation coefficient (CC) increases from 0.74 to 0.92 in the unpreprocessed to preprocessed case, indicating that the preprocessed field is closer to the chromospheric field, and hence closer to the force-free condition. Additionally, as confirmed by some model tests (Metcalf et al. 2008; Wiegelmann et al. 2008), the ability of the NLFF field extrapolation algorithms to reconstruct the coronal field morphology is substantially improved by using the preprocessed photospheric boundary.

Finally, the NLFF field and the potential field were extrapolated from the disambiguated and preprocessed magnetograms using the weighted optimization method (Wiegelmann 2004) and Green's function method (Aly 1989), respectively. The weighted optimization method is an implementation of the original work of Wheatland et al. (2000). It

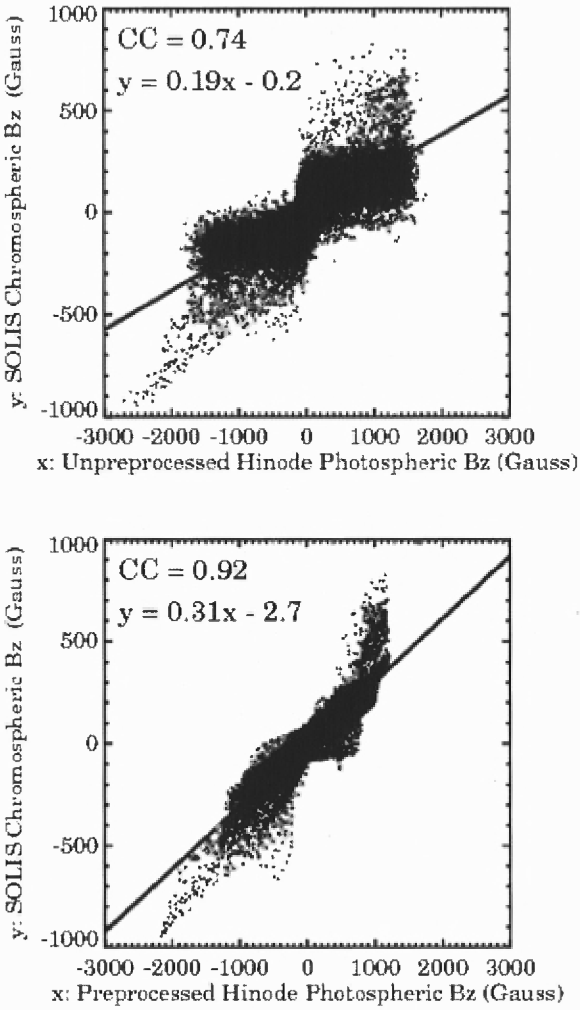

Figure 3.1 *Top*: SOLIS chromospheric line-of-sight magnetic field B_z vs. unpreprocessed Hinode/SP photospheric B_z; *Bottom*: SOLIS chromospheric B_z vs. preprocessed Hinode/SP photospheric B_z. The SOLIS chromospheric magnetogram was taken on 2007 Jun. 8 at 18:28 UT in AR 10960, and the Hinode/SP photospheric magnetogram was taken at 18:39 UT on the same day and in the same active region. The solid line in each panel is the least-square best fit to the data points in a form of $y = ax + b$, where a and b are constants. The linear correlation coefficients (CCs) between the quantities are shown in each panel.

involves minimizing a joint measure (L) for the normalized Lorentz force and the divergence of the field throughout the computational domain V:

$$L = \frac{1}{V}\int_{V}[\omega_f(\mathbf{r})B^{-2}|(\nabla\times\mathbf{B})\times\mathbf{B}|^2 + \omega_d(\mathbf{r})|\nabla\cdot\mathbf{B}|^2]dV, \tag{3.3}$$

where $B = |\mathbf{B}|$, ω_f and ω_d are weighting functions for the force and divergence terms, respectively. Both ω_f and ω_d are position-dependent. They are chosen to be 1.0 in the center of the computational domain and drop to 0 monotonically in a buffer boundary region that consists of 16 grid points towards the side and top boundaries. More detailed descriptions of the method were given by Wiegelmann (2004) and Schrijver et al. (2006). Subsequently the author derived free magnetic energy E_{free} using the integration Equation 3.1 over the 3-D volume.

3.3 Description of Active Regions

Hinode was launched in September 2006 and the SOT-SP onboard *Hinode* captured its first light on October 2006. A total of 97 active regions were identified by NOAA from 2006 October 1 to 2008 December 31, i.e., NOAA 10913-11009. Of these active regions, during their lifetime, a considerable part (73 of 93) did not produce any flare activity above B-class (referred to as "flare-quiet"), 21 produced moderate flares (C-class) and three produced major flares (X- and/or M-class).

To check the statistical correlation between E_{free} and FI_{n-day}, it is important that the sample is comprised of major flaring, moderate flaring and flare-quiet regions. Therefore, the author gave priority to NOAA 10930 and 10960, as they are 2 of the very few active regions which produced major flares. Moreover, NOAA 10930 and 10960 are well covered by the SOT-SP observation over a period of several days. The data taken at both flare-active and flare-quiet phases not only expand the sample size but also diversify the values of FI_{n-day}. Additionally, another 11 active regions are included in the sample to supplement the low end of FI_{n-day}. The data selection is mainly based on the availability the SOT-SP data. A final tally of 75 vector magnetgrams from 13 active regions are analyzed in this chapter. The distribution of FI_{3-day} shows that 33 of 75 (44%) cases lie between 0 and 1 (i.e., flare-quiet during the subsequent 3-day time window), 27 of 75 (36%) cases lie between 1 and 10 (equivalent to a daily average of a C-class flare during the subsequent 3-day time window) and the rest 15 (20%) cases are larger than 10 (equivalent to a daily average of a M/X-class flare during the subsequent 3-day time window). Table 3.1 lists the information on the 13 active regions.

As shown in the 4th column of the Table 3.1, the heights of the computational domain are chosen to be 120″above the photosphere for all the cases, but the FOVs on the lower boundary vary from case to case according with the SOT-SP scan area. Since E_{free} is a volume-integrated parameter, the difference in the lower boundary FOVs may introduce an uncertainty in the statistical correlation and must be treated with caution.

Figure 3.2 presents an example in which the author tested how E_{free} of an active region changes with the varying FOV and height of the computational domain V. The top panel in Figure 3.2 shows a LOS magnetogram of the active region NOAA 10930. The colored boxes mark the 9 different FOVs, ranging from $30'' \times 12''$ to $288'' \times 158''$. The smallest box only covers a small area around the flaring PIL, while the largest box covers not only the sunspots that comprise the major portion of this active region but also the weaker plage regions surrounding the sunspots. The bottom left panel shows the NLFF field energy E_N, the potential field energy E_p and the free magnetic energy E_{free} as a function of the 9 selected FOVs, given a fixed height (120″) of V. As shown in Eq.(1), E_{free} is defined as the excess E_N from E_p. Each data point with a certain color corresponds respectively to the FOV box with the same color. The E_{free} first increases rapidly with an expanding FOV, then reaches its maximum when the major portion of this region is covered by the FOV, then changes little despite the continued growth of FOV. The bottom right panel shows E_N, E_p and E_{free} as a function of height, given a fixed FOV (288″ × 158″) of the lower boundary of V. Evidently, E_{free} displays an impulsive increase from the lower boundary to a certain height (50″in this case), then stays almost constant beyond this height. The author ran the E_{free}-FOV and E_{free}-height tests on other active regions and get similar results. It suggests that the difference in FOVs of the samples is not likely to significantly affect the statistical correlations that will be shown in §3.4, as long as the sampled active regions are well covered by the magnetograms. It also suggests that the magnetic fields approach potential beyond a certain height which is of tens of arcsec magnitude order, consistent with previous results (Jing et al. 2008). A height of 120″ of V adopted in this study seems to be enough to constrain the nonpotential magnetic fields.

To study the temporal variation of E_{free}, the author selected three active regions, NOAA 10930, 10960 and 10963. As mentioned, the former two exhibited one major flare and several moderate flares during the SOT-SP observations over a period of days. The latter produced a few moderate flares at some point in its lifetime, but did not flare during the observation period. For each region, a sequence of the vector magnetograms at a general cadence of a few hours is used as the boundary conditions to extrapolate the 3-D NLFF

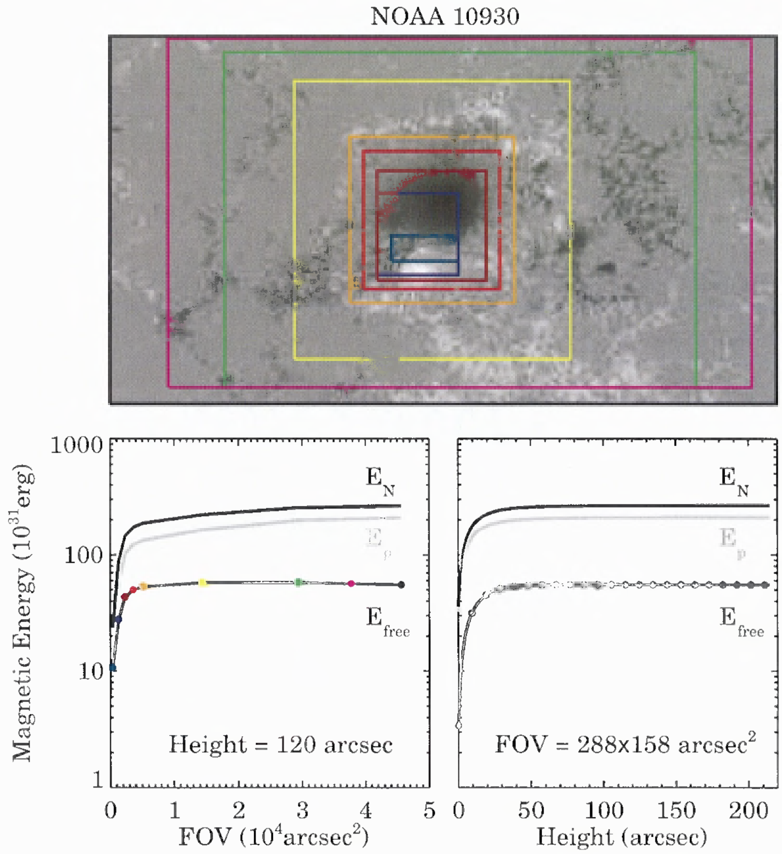

Figure 3.2 *Top*: A snapshot of line-of-sight magnetograms of NOAA 10930. The whole FOV is $288'' \times 158''$. The colored boxes mark the 9 different FOVs. *Bottom Left*: the NLFF field energy E_N, the potential field energy E_p and the free magnetic energy E_{free} as a function of the 9 selected FOVs, given a fixed height ($120''$). The data dot with a certain color corresponds respectively to the FOV box with the same color. *Bottom Right*: E_N, E_p and E_{free} as a function of height, given a fixed FOV of $288'' \times 158''$.

field. These magnetograms are co-aligned to have the same target location and the same FOV. In Figure 3.3, the snapshots of the vector magnetogram of the 3 regions and the corresponding NLFF fields are shown in the left and right columns, respectively.

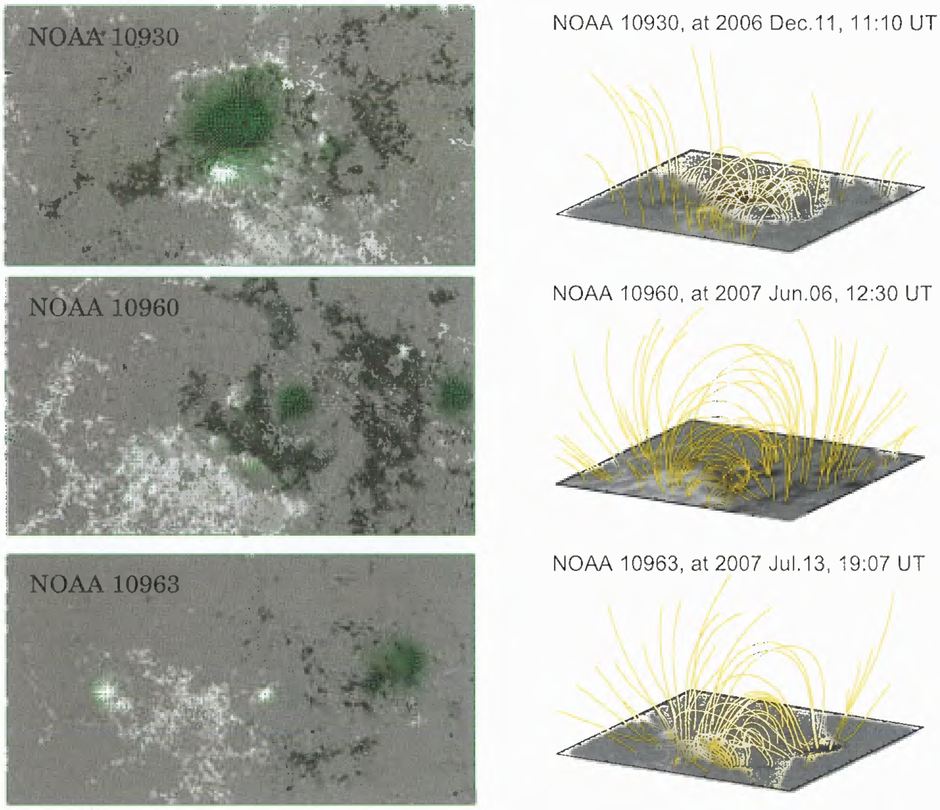

Figure 3.3 *Left panels*: Snapshots of the *Hinode*/SP vector magnetograms. From top to bottom, they are NOAA 10930 taken on 2006 Dec. 11 at 11:10 UT, NOAA 10960 taken on 2007 Jun. 6 at 12:30 UT, NOAA 10963 taken on 2007 Jul. 13 at 19:07 UT. The background images are the line-of-sight magnetograms. Green arrows indicate the transverse fields. The FOVs of three magnetograms are $288'' \times 158''$, $288'' \times 158''$, and $288'' \times 154''$, respectively. *Right panels*: Extrapolated NLFF fields of NOAA 10930, 10960 and 10963. The boundary images are the vector magnetograms shown in the left panels.

3.4 Results

In Figure 3.4, the left-to-right top panels show the scatter plots of FI_{3-day} vs. E_{free}, FI_{2-day} vs. E_{free}, and FI_{1-day} vs. E_{free}, respectively. The solid line superposed in each plot indicates the least-square best fit to the data points. The cross CCs between the quantities are also given in the panels. Note that FI_{n-day} is plotted in a logarithmic scale. The FI_{n-day} with 0 value is set to 0.01 to avoid arithmetic error and are shown as grey points. These grey points are excluded from the fitting and CC calculation. While the points are widely scattered, the result still reveals a positive correlation between the quantities ($0.55 < CCs < 0.76$), suggesting that major flares generally come from active regions with high energy content.

Furthermore, to test the ability of E_{free} to distinguish between flare-quiet and flare-active populations, the author divided the data points into four groups (denoted by (1)-(4), seen in the middle panel of Figure 3.4) with the horizonal and vertical dashed lines in each panel. The horizonal dashed line shows the observed $FI_{n-day} = 1$, which is equivalent to a daily average of a C1.0 flare within the time window and is taken as a threshold for flare-active regions. The vertical dashed line is drawn according with the derived maximum E_{free} of the flare-quiet regions. The author wished to test the hypothesis that the population on the right side of the vertical line are flare-active. In this sense, group 1 refers to incorrectly rejected the flare-active cases (Type I error) and group 2 refers to failing to reject the flare-quiet cases (Type II error). Groups 3 and 4 (the shaded areas) mean that flare-quiet and flare-active populations are well separated by the vertical line. The frequencies of the groups 1-4 are also given in Figure 3.4. Inspection of Figure 3.4 immediately reveals that most of data points fall into groups 3 and 4. The Type I and Type II error rates are $\sim 8 - 12\%$ in total. This means that, based on the sample presented here, flare-quiet and flare-active populations can be separated by E_{free} with a $\sim 88 - 92\%$ success rate.

For comparison, the middle and bottom panels of Figure 3.4 show similar diagrams

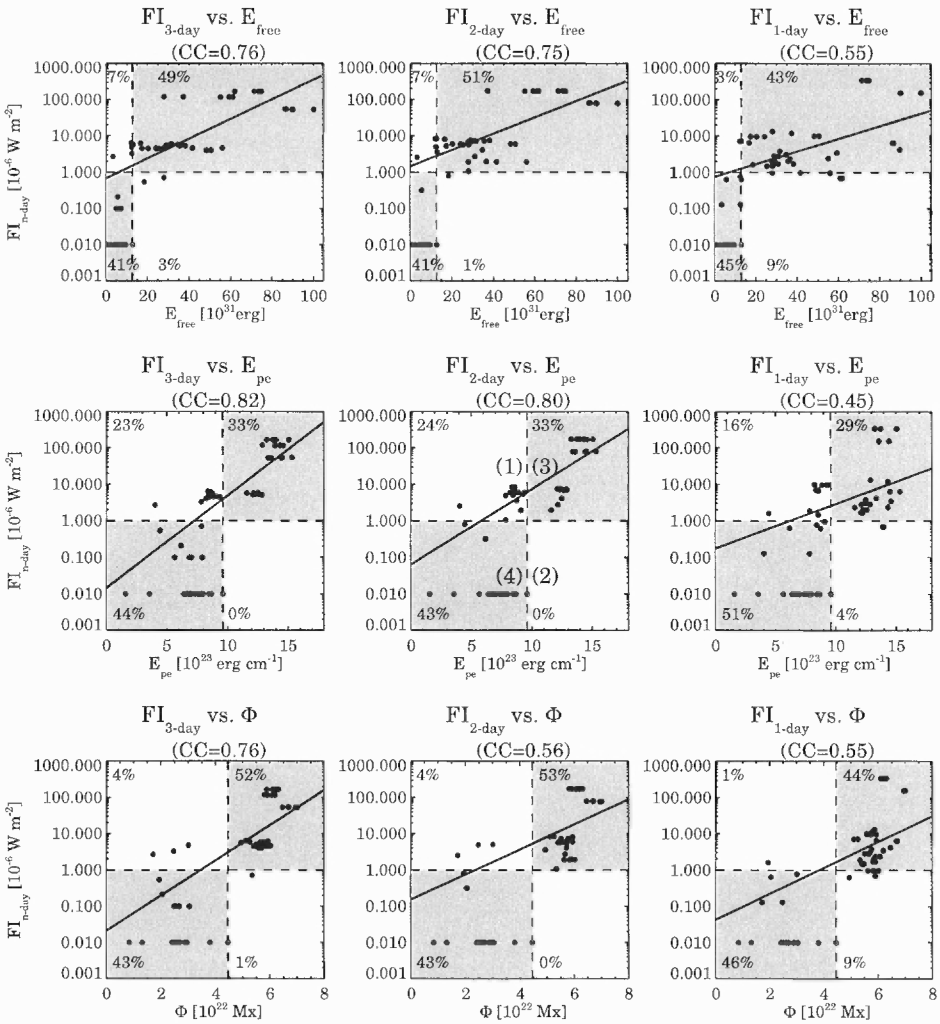

Figure 3.4 *Top panels*: Scatter plots of FI_{n-day} vs. E_{free}; *Middle panels*: Scatter plots of FI_{n-day} vs. E_{pe}; *Bottom panels*: Scatter plots of FI_{n-day} vs. Φ, where n = 3, 2, 1 from left to right. The FI_{n-day}s with 0 value are set to 0.01 to avoid arithmetic error and shown as grey points. The solid lines indicate the least-square best fits to the data points, and CCs are correlation coefficients, with grey points excluded. In each panel, the data points are divided into four groups, denoted by (1)-(4) in the middle panel, with the horizontal and vertical dashed lines. The horizontal dashed line shows $FI_{n-day} = 1$, while the vertical dashed line is drawn according with the maximum E_{free} of the flare-quiet regions. The percentages refer to the frequencies of each group.

in which the photospheric excess energy E_{pe} and the total unsigned photospheric magnetic flux Φ are plotted against the FI_{n-day}. The definitions of E_{pe} and Φ are given in §3.1. The former is regarded as a proxy for E_{free}, while the latter is a simple measure of an active region's size (Barnes & Leka 2008). The positive correlations are still evident in each panel. The author also notes the following properties:

First, when two populations (flare-quiet and flare-active) are concerned, Φ and E_{free} perform better than E_{pe} in separating two populations. Taking the 3-day time window for example, the success rate of Φ, E_{free} and E_{pe} are 95%, 90% and 77%, respectively.

Secondly, when only considering the flare-active population, all three parameters are moderately to strongly correlated with FI_{n-day}. In addition, despite the fact that E_{free} is one of the most direct measures for the available energy in a 3-D magnetic field, its correlations with FI_{n-day} are found to be quite similar to the correlations of the photospheric magnetic parameters, E_{pe} and Φ. In particular, E_{pe} performs best in relating to FI_{3-day} with a CC as high as 0.82 and performs worst in relating to FI_{1-day} with a CC of 0.45. Basically the difference among these three parameters is not significant. The similar magnitudes of the CCs imply that E_{free}, E_{pe} and Φ have approximately equal predictability for flares.

Finally, as a general trend, the magnitude of the CCs decreases as the time window of FI becomes narrower from 3-day to 1-day. It reveals that the magnetic parameters have relatively less predictability for flares within a 1-day time window than a 3-day time window. It is understandable, because flares as a result of electromagnetic instabilities may occur only under certain circumstances and after a substantial waiting time (Schrijver et al. 2005). Forecasting imminent flares certainly faces more uncertainties than forecasting long-term flares.

Figure 3.5 illustrates how three magnetic parameters, E_{free}, E_{pe} and Φ, correlate with each other. The colored data points from dark to light refer to an increasing levels of FI_{3-day} from flare-quiet to major flaring. Apparently, the major flaring samples generally exhibit higher values of E_{free}, E_{pe} and Φ than the flare-quiet ones. It is interesting to note that, the data points of E_{free}-Φ in the top panel can be fitted by two lines with different slopes. The lower line mainly contains the data from flare-quiet samples, while the higher line is comprised of data from two major flaring active regions (NOAA 10930 and 10960) that were observed on a timescale of several days. E_{pe} does not exhibit such a pattern with Φ. The result suggests that Φ is fairly constant for major flaring regions, but E_{free} may change significantly over days. In addition, the correlation between E_{free} and Φ is weak (CC=0.3) for flare-quiet samples, but very strong (CC=0.86) for flare-active ones.

Theoretically speaking, the statistical relation between E_{free} and FI_{n-day} and the temporal variation of E_{free} derived from individual active regions can provide clues to distinguish between flare-active and flare-quiet regions. The author compared the long-term variation of E_{free} for 3 active regions, NOAA 10930, 10960 and 10963. Figure 3.6 shows the time profiles of E_{free} (grey histogram), E_{pe} (green diamonds), Φ (blue pluses) and the GOES SXR 1-8 Å light curves (red curves). The flares that originated from the active regions are indicated by the black arrows. NOAA 10930 dominated the solar activity during the observation from 2006 December 9 to 14, and produced a X3.4 flare on 2006 December 13. As shown in Figure 3.6, E_{free} in NOAA 10930 is remarkably built up during the 2 days prior to the X3.4 flare and even continues to increase after the flare. NOAA 10960 is also flare-active. It produced a M1.0 flare on 2007 June 9, at the very end of this

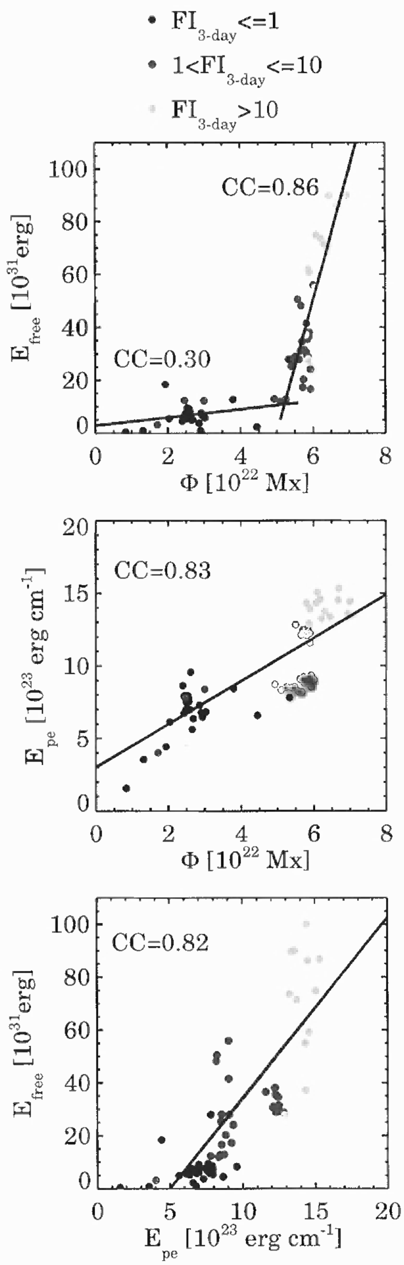

Figure 3.5 *Top panels*: Scatter plots of E_{free} vs. Φ; *Middle panels*: Scatter plots of E_{pe} vs. Φ; *Bottom panels*: Scatter plots of E_{free} vs. E_{pe}. The solid lines are the least-square best fits to the data points, and CCs are correlation coefficients. The different colors of the data points refer to the different levels of the flare activity within the subsequent 3 days.

observation, and 4 C-class flares during the observation. E_{free} in NOAA 10960 fluctuates and does not have obvious association with the flare occurrence. NOAA 10963 did not flare during the observation from 2007 July 12 to July 16, and contains a clearly lower amount of E_{free} in comparison with the other two regions. Since the long-term trend of E_{free} varies from case to case, the author found no particular pre-flare signatures useful in predicting flares.

3.5 Summary and Discussion

In this chapter, the author examined the magnitude scaling correlation between FI_{n-day} and E_{free} based on the 75 samples, and also study the temporal variation of E_{free} with respect to the GOES SXR light curves for three active regions. The most important results are summarized as follows:

1. E_{free} is moderately to strongly correlated with FI_{n-day}. The correlation confirms the physical link between magnetic energy and flare productivity of active regions. However, compared with two photospheric magnetic parameters E_{pe} and Φ, E_{free} shows little improvement for flare predictability.

2. While the magnitude of E_{free} unambiguously differentiates between the flare-active and the flare-quiet regions, the temporal variation of E_{free} does not exhibit a clear and consistent pre-flare pattern.

One likely cause of the lack of satisfactory results is that the storage of E_{free} in magnetic fields is a necessary but not sufficient condition for the onset of solar flares. The trigger mechanism of flares is the determining factor of whether and when an active region will flare. Recently, there has been growing evidence relating emerging flux regions (EFRs)

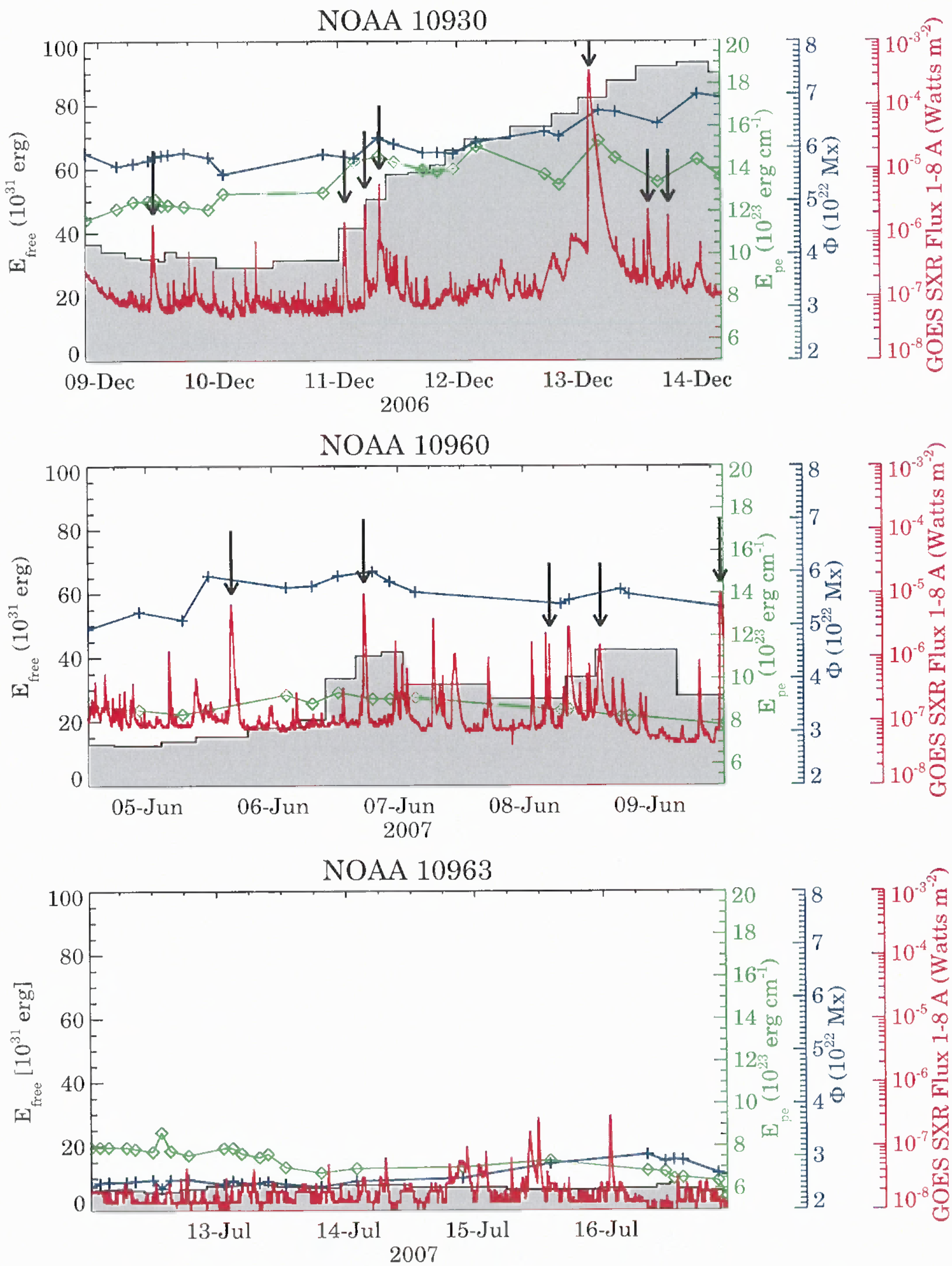

Figure 3.6 Temporal variation of free magnetic energy E_{free} (grey histograms), photospheric excess energy E_{pe} (green diamonds), the photospheric unsigned magnetic flux Φ (blue pluses) and the GOES SXR $1-8$ light curves (red curves) of NOAA 10930, 10960 and 10963. The flares that originated from the active regions are indicated by the black arrows.

and magnetic helicity to the flare trigger mechanism. Magnetic helicity is a measure of magnetic topological complexity such as twists, kinks and linkages of magnetic field lines (Berger & Field 1984). As suggested by a numerical simulation and supported by many observations, flares preferentially occur in the presence of a particular magnetic topology, which is prone to the annihilation of magnetic helicities with opposite signs between the newly EFR and the preexisting region (Kusano et al. 2003b,a; Yokoyama et al. 2003; Wang et al. 2004b; Jing et al. 2004). In addition, the monotonically increasing helicity over days prior to major flares has been found, which can be used as a warning sign of the flare onset (LaBonte et al. 2007; Park et al. 2008). The author expects that a combination of E_{free} and magnetic helicity in future studies would carry extra weight in predicting flares.

Moreover, the energy release process involves a variety of dynamic phenomena such as flare heating, particle acceleration and CME dynamics (Gibson et al. 2009). Consequently, the released E_{free} is converted and partitioned into the forms of thermal and non-thermal emissions and kinetic energy of CMEs. Considering that the SXR FI only quantifies a fraction of the released energy, i.e., the thermal part, the author probably should not expect a very strong correlation between E_{free} and FI_{n-day}.

Besides the concerns on flare trigger and energy release mechanisms, the NLFF field modelling from the photospheric boundary is subject to both observational limitations and intrinsic physical and/or mathematical problems. The observational limitations include the large uncertainties in transverse field measurements (Klimchuk & Canfield 1994), and 180° azimuthal ambiguity (Metcalf et al. 2006), etc. The physical/mathematical problems are related to the non-force-free nature of the photospheric boundary (Metcalf et al. 2008), and the difficulties of guaranteeing the existence and uniqueness of the NLFF field solutions (Rudenko & Myshyakov 2009). Although the use of high-quality magnetogram data and the advanced preprocessing and modelling algorithm improves the situation to some extent, the ability of the NLFF field model to reproduce the real coronal field and E_{free} is seriously compromised (DeRosa et al. 2009). Moreover, the NLFF field is only a good approximation in the force-free domain (i.e., chromosphere and lower corona), not in the high-β photosphere and upper corona. Future improvements on magnetic field modelling may come from developing a self-consistent magnetohydrostatic (MHS) modelling (Wiegelmann et al. 2006), and incorporating information on the coronal field topology as seen, for example, by the the Transition Region and Coronal Explorer (TRACE), and the twin Solar Terrestrial Relations Observatory (STEREO) (Wiegelmann et al. 2009).

Table 3.1 Information of Active Regions

Index	NOAA	number of frames	Maximum Flare Magnitude During Lifetime	Dimensions of V^{a} [arcsec^3]	$FI_{overall}{}^{b}$ [10^{-6} W m^{-2}]
1	10930	25	X3.4	288×158×120	112.7
2	10960	15	M1.0	288×158×120	18.1
3	10921	1	C3.7	144×144×120	0.4
4	10923	1	C3.3	100×120×120	1.1
5	10933	1	C1.7	187×158×120	0.6
6	10938	1	C4.2	187×158×120	0.9
7	10940	1	C3.4	158×158×120	1.0
8	10953	1	C8.5	144×144×120	1.1
9	10956	1	C2.9	154×154×120	0.7
10	10963	25	C8.2	288×154×120	3.2
11	10978	1	C4.5	149×149×120	1.6
12	10961	1	None	158×158×120	0.0
13	11005	1	None	149×149×120	0.0

[a] V: the volume of computational domain, see Equation 3.1

[b] $FI_{overall}$: is calculated with Equation 3.2, the time window τ is the lifetime of the active regions

CHAPTER 4

RELATIONSHIP BETWEEN 3-D MAGNETIC STRUCTURE AND CORONAL EMISSIONS

4.1 Introduction

A solar active region, when it is in a quiescent period and passes through solar disk center, is a preferable object for studying coronal heating mechanism than quiet sun regions, as an active region contains stronger magnetic fields and hotter coronal plasma thus the observational signal covers much large dynamic range. Although coronal heating mechanism is not fully understood and there are numbers of proposed coronal heating models: steady heating models including stressing models (direct current, DC) and wave models (alternating current, AC) heating models (Aschwanden 2001; Démoulin et al. 2003; Klimchuk 2006) and dynamic nanoflare heating model (Parker 1988; Reale et al. 2009; Schmelz et al. 2009), the coronal heating energy is essentially believed from the coronal volume of magnetic fields above the photospheric surface of an active region. Photospheric magnetic parameters have been extensively studied with related the coronal response, for instance magnetic flux, magnetic energy dissipation and Poynting flux proxy (Fisher et al. 1998; Abramenko et al. 2006b) and so on. Chapter 2 has discussed these results. These magnetic parameters represent different processes of magnetic energy deposition into the corona. However, no matter how the magnetic energy is transformed to kinetic and thermal/nonthermal energy, the magnetic fields should offer sufficient so-called free magnetic energy, according to the energy conservation law.

Poynting flux represents the energy flux of a propagating electromagnetic field.

Moreover, it links the magnetic energy between photosphere and corona. From below the photosphere, the pre-existing magnetic energy can be injected into the coronal volume by photospheric Poynting flux (or photospheric footpoint random motions) (Klimchuk 2006; Tan et al. 2007). Therefore, the intrinsic relationship between Poynting flux and coronal free magnetic energy might provide implications of dynamic magnetic energy balance.

This chapter focuses on the evolution profiles of three area-integrated photospheric magnetic parameters including unsigned magnetic flux, Poynting flux and free magnetic energy and three coronal measurements, e.g. coronal soft X-ray brightness, temperature and emission measure. In §4.2, data sets and reduction techniques are presented; in §4.3, the parameters are described; the results are summarized in §4.4; the coronal thermal energy of NOAA 10963 is estimated in §4.5 and the last Section §4.6 includes the discussion.

4.2 Data Sets and Data Reduction

Two active regions are selected when they are in flare-quiet periods. Active region NOAA 10930 experienced a relatively quiescent period from December 8 to December 13, 2006 before the major X3.4 flare, only four flares below C2 happened in this time interval. Active region NOAA 10963 was an even quieter active region than NOAA 10930 from July 11 to July 17, 2007, there was no flare above C class occurred in this active region. Both the active regions were crossing solar central meridian in their observational time intervals. In these two time intervals, the Solar Optical Telescope (SOT) (Suematsu et al. 2008; Tsuneta et al. 2008) and X-Ray Telescope (XRT) (Golub et al. 2007) on board *Hinode* (Kosugi et al. 2007) had excellent coverages of observations.

The Spectro-Polarimeter (SP) instrument of SOT, which obtains Stokes profiles from two magnetically sensitive spectral lines of iron 630.15 and 630.25 nm (Tsuneta et al. 2008) with the spatial resolution about $0''.29$ (slit size or E-W direction) by $0''.32$ (vertical scan size or N-S direction), provides the spectroscopy of photospheric magnetized plasma around the two lines. The magnetic field measurements are fully inverted by using an Unno-Rachkovsky inversion method under the assumption of the Milne-Eddington (ME) atmosphere model (e.g. Skumanich & Lites 1987; Klimchuk et al. 1992). From the ME inversion, the field strength, inclination angle and azimuth angle are obtained. The next step is to resolve the 180 degree ambiguity in the vector magnetograms with the "minimum energy" algorithm that simultaneously minimizes both the electric current density and the field divergence (Metcalf 1994; Metcalf et al. 2006). Force free assumption of photospheric magnetic field is not completely valid, hence the photospheric boundary preprocessing is required to minimize this effect by Wiegelmann's method which minimizes both the overall Lorentz force and magnetic torque (Wiegelmann et al. 2006, 2008; Metcalf et al. 2008; Jing et al. 2009b). Based on the preprocessed vector magnetograms, the non-linear force free (NLFF) fields are extrapolated by Wiegelmann's weighted optimization method (see Wiegelmann (2004) and references therein). At the mean while, the 3-D potential fields are obtain by a Green's function method (Aly 1989) (more detailed description in Section 3.2 Chapter 3).

The G-band (430 nm) observations are obtained with the Broadband Filter Imager (BFI) of SOT with a cadence about 1 or 2 minutes (Tsuneta et al. 2008). The pixel size of the G-band image is $0''.109$ by $0''.109$ or the nominal resolution is about $0''.218$ arc sec. The G-band data are preprocessed by the standard *Hinode* SSW package fg_prep.pro to remove dark flows and flatness of telescope CCD. The active region plasma motion or flow map is measured by local correlation tracking (LCT) method which is similar to what was used by Simon et al. (1988) (see descriptions in Chapter 6 or Tan et al. (2009)).

All the projection effects are corrected for those vector magnetograms and G-band images if they are not close to the solar disk center before measuring magnetic parameters and flow maps. Removing the projection effects improves the photospheric magnetic measurements and makes the LCT sampling window and Gaussian weighing function symmetric.

The XRT, a soft X-ray grazing incidence telescope with $1''$ pixel size resolution, contains nine filters with different temperature responses and measures a wide temperature spectra of corona (Kosugi et al. 2007). Because of multiple filter observations, intensity ratio between different filters can be utilized to obtain coronal plasma temperature and emission measure based on the ATOMDB/APEC plasma emission model (Reale et al. 2007). The filter ratio technique assumes the coronal plasma is isothermal in the line-of-sight direction. The author employed filters of Be_med and C_poly and the characteristic response temperature of this filter ratio is about $10^{6.5}$ K (Reale et al. 2009). All the XRT data are processed by the standard package xrt_prep.pro to remove vignettes, pattern noise, jitters and normalize the exposure time.

4.3 Parameters

4.3.1 Photospheric Magnetic Parameters

Three parameters of the magnetic field are computed from the two nominally continuous data set. They are unsigned total magnetic flux, Poynting flux and free magnetic energy. In the following, B_x, B_y, and B_z represent components of magnetic field in Cartesian coordinate system with z along line-of-sight, and x,y situated in the image plane. As we the projection effects of the two active regions were corrected, the axes of this coordinate system are close to true vertical and horizontal directions in respect to solar surface.

(1) unsigned line-of-sight total magnetic flux Φ:

$$\Phi = \sum_{i=1}^{n} |B_z| dA. \tag{4.1}$$

here A is the integration area. Schrijver et al. (1985) and Fisher et al. (1998) have shown that unsigned magnetic flux has strong correlation with coronal soft X-ray brightness.

(2) photospheric Poynting flux:

Magnetic energy flux cross the photosphere due to the footpoint motions of magnetic concentrations and twists of magnetic flux loop can be expressed as the Poynting flux (Parker 1979, 1988; Dahlburg et al. 2005):

$$F = -\frac{1}{4\pi} \cdot B_z \cdot \mathbf{B_h} \cdot \mathbf{V_h} \tag{4.2}$$

here B_h is the horizontal component of the magnetic field and V_h is the horizontal velocity vectors. All the elements of Eq. (4.2) are measurable so that real measurement of Poynting flux can be fulfilled. To minimize the measurement error, the author co-registers velocity vectors with vector magnetograms by co-aligning G-band image and continuum intensity (Figure 4.1 demonstrates the Poynting flux of NOAA 10930 on December 8, 2006).

(3) free magnetic energy:

The structure of 3-D magnetic field is constructed by NLFF field and potential field extrapolations as described above. Figure 4.2 shows the 3-D extrapolated NLFF field of

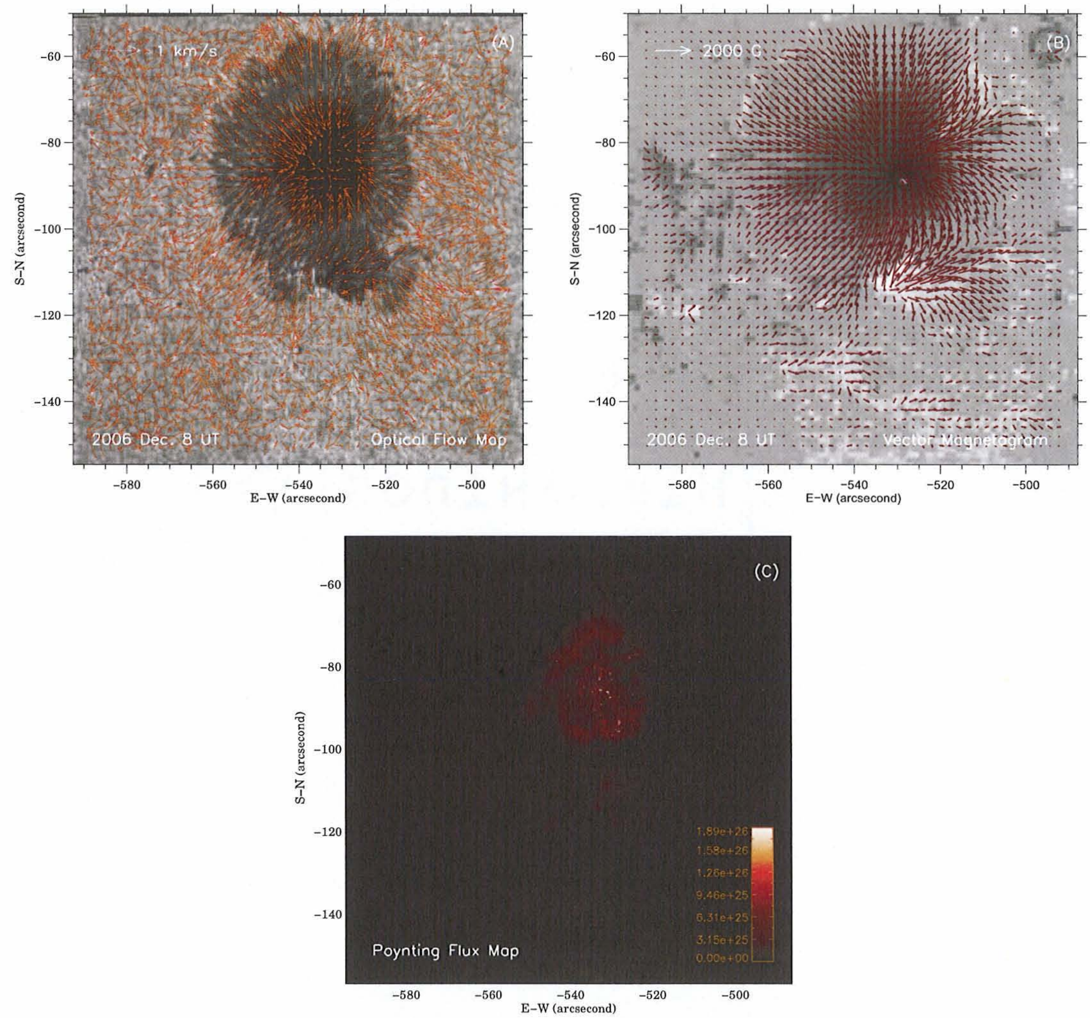

Figure 4.1 (A) Flow map on G-band image (B) vector magnetogram on line-of-sight magnetogram and (C) derived Poynting flux of NOAA 10930 on December 8, 2006. The projection effects are corrected.

NOAA 10930 and NOAA 10963. The free magnetic energy, the upper limit of magnetic energy available for release, can be quantified as the magnetic energy departure between the non-constant α current-carrying system and current-free one (Wheatland et al. 2000; Schrijver et al. 2005; Jing et al. 2009b):

$$E_{free} = E_{NLFF} - E_p = \int \frac{B_{NLFF}^2}{8\pi} dV - \int \frac{B_p^2}{8\pi} dV, \tag{4.3}$$

where V is the coronal volume above the photosphere which contains the extrapolated fields.

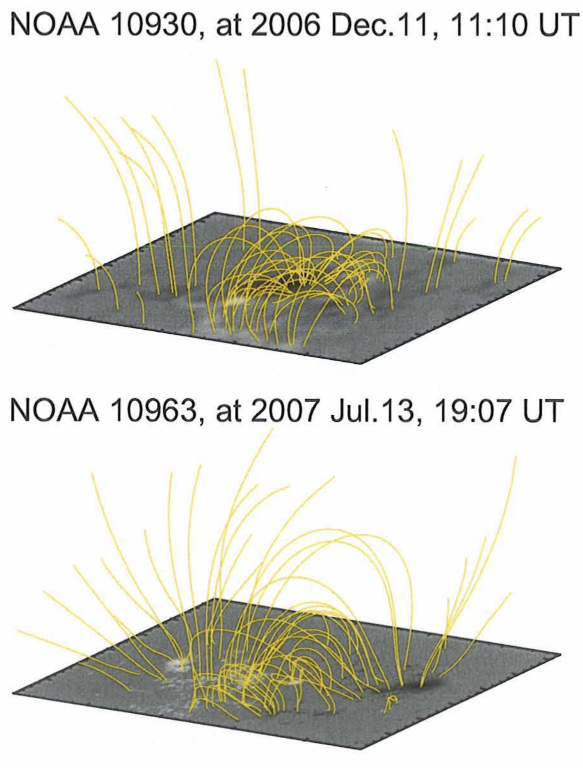

Figure 4.2 The extrapolated NLFF fields of NOAA 10930 (upper panel) and NOAA 10963 (lower panel).

4.3.2 Coronal Parameters

(1) soft X-ray brightness:

Coronal soft X-ray brightness (L_B) is computed by integrating the normalized filter intensity (in Digital Numbers, DN):

$$L_B = \int \ell_B(i) dA, \tag{4.4}$$

where dA is a pixel area, $\ell_B(i)$ is X-ray brightness of i^{th}-pixel, and n is the total number of pixels.

To calculate soft X-ray brightness, the author selected pixels which brightness exceeds triple of standard deviation of noise level above average intensity.

(2) coronal emission meassure:

$$EM = \int n^2 \cdot V_i dA, \tag{4.5}$$

here n is the line-of-sight plasma number density of each pixel area and V_i is the product of pixel area and column depth.

(3) coronal plasma temperature: T

The coronal plasma temperature is derived by the filter ratio technique, as described above as the temperature response functions of each filter are known (Kosugi et al. 2007).

4.4 Results

4.4.1 Temporal Evolution of NOAA 10930

Active region 10930 was a highly flare-productive region in it crossed the solar disk, however it had several relatively quiescent periods. The one under study is from the end of December 8 to the early of December 13, 2006. Figure 4.3 shows the evolutions of the photospheric and coronal parameters. In the four day time window, the total unsigned magnetic flux gradually increased 27.7% from 4.7×10^{22} to 6.0×10^{22} Mx. Correspondingly, the total outward (towards the earth) Poynting flux increased 70.0% from 2.0×10^{29} to 3.4×10^{29} ergs s^{-1}. The two similar evolution tendencies might imply the Poynting flux is dominated by the magnetic flux.

The free magnetic energy of this NOAA 10930 kept constant from December 9 to December 10 and starts to increased from the end of December 10 towards time of the X3.4 flare on December 13. As the free magnetic energy stayed flat, both magnetic non-potential energy and potential energy did not change much. When free magnetic energy started to increase, the magnetic potential energy increased, and so did the non-potential energy. However, the magnetic non-potential energy increased faster. For this active region, only one medium filter, Be_thin, operated the observation. Without filter ratio, the temperature and emission measure information is not available. The tendency of the evolution of the total soft X-ray brightness monotonously increased from 3.0×10^{6} to 9.0×10^{6} DN.

4.4.2 Temporal Evolution of NOAA 10963

The two-day temporal profiles of photospheric and coronal quantities are shown in Figure 4.4. The active region was in a decay phase, the total unsigned magnetic flux and Poyting

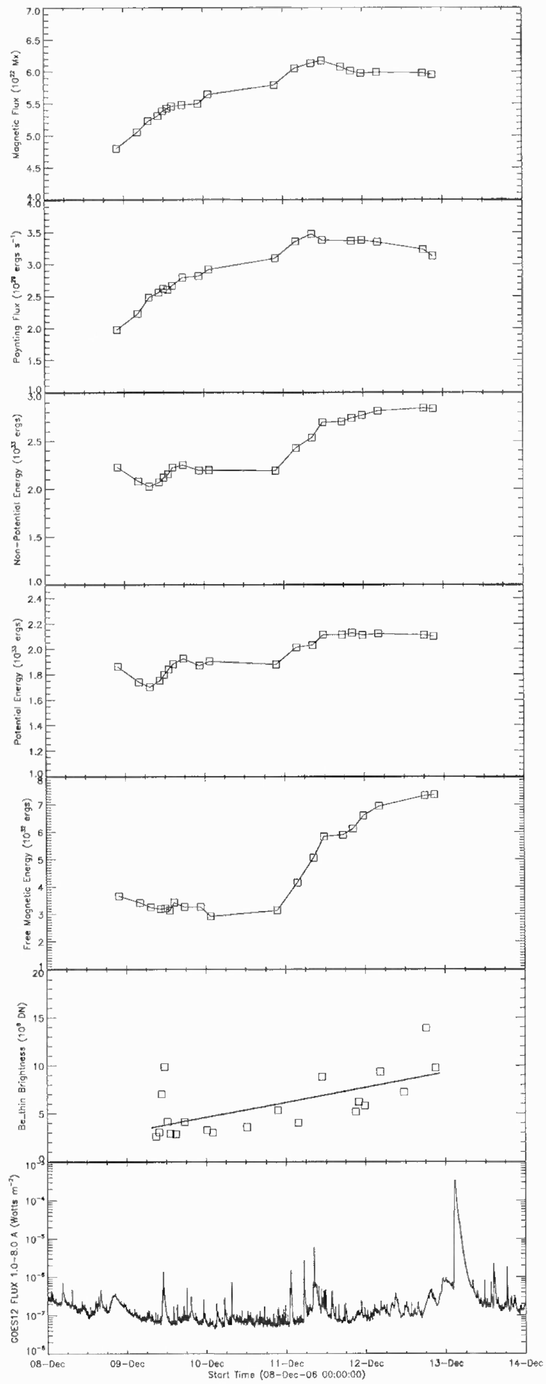

Figure 4.3 Temporal profiles of photospheric and coronal parameters of NOAA 10930. From top to bottom, the quantities are: total unsigned magnetic flux, Poynting flux, total magnetic energy, potential magnetic energy, free magnetic energy, soft X-ray brightness through Be_thin filter and GOES soft X-ray flux.

flux gradually decreased 42.2% and 61.1%, respectively. The potential and non-potential energies evolved in similar patterns. No matter how complex the evolution patterns were, the coronal-volume integrated free magnetic energy went constantly, around 7.0×10^{31} ergs. This active region was covered by three soft X-ray filters. The author applied the filter ratio technique on two filters, Be_med (hard filter) and C_poly (soft filter) (see details of filter ratio technique in Reale et al. (2007) and therein references). And all the evolutions of soft X-ray brightness through filter Ti_poly, the averaged temperature and emission measure seem to keep invariant despite minor oscillationally increase or decrease.

4.5 Thermal Energy Budget

For a flare-quiet active region, the free magnetic energy will partially transform to thermal energy to heat the plasma in coronal volume. It is important to roughly estimate this amount of required thermal energy for the specific active region NOAA 10963. The author treats the whole coronal volume of strand-unresolved magnetized plasma as an isolated plasma conglomeration and assume the plasma is isothermal and uniform in the line-of-sight direction. The emission measure can be conveniently obtained from the filter ratio technique, however the difficulty is to measure the column depth. The column depth of the coronal quiescent active region NOAA 10963 can be measured when it rotated to the west limb on 2007 July 21, assuming it did not decay much in the quadural rotation from the disk center to the west limb. Because of the scantiness of soft X-ray observation when it rotated to the west limb, the author substitutes the observation by *SoHO* EIT 284 Å image. *SoHO* EIT 284 Å is sensitive to the temperature of about 2.0 MK (Delaboudinière et al. 1995, 1997) which is lower in height than soft X-ray observation (Aschwanden & Nitta 2000).

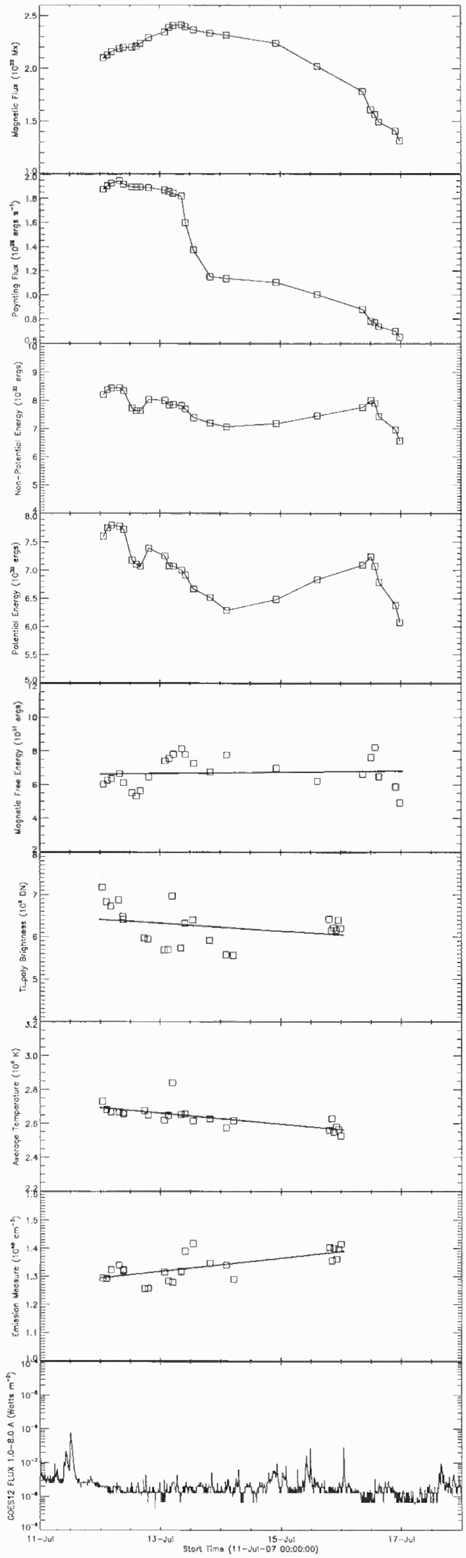

Figure 4.4 Temporal profiles of photospheric and coronal parameters of NOAA 10963. From top to bottom, the quantities are: total unsigned magnetic flux, Poynting flux, total magnetic energy, potential magnetic energy, free magnetic energy, soft X-ray brightness through Ti_poly filter, averaged active region coronal temperature, emission measure and GOES soft X-ray flux.

This causes an about 35% underestimation of the column depth. The edge of the bright coronal plasma is fitted via a parabolic function (see Figure 4.5) and artificially construct a parabolic surface (see Figure 4.6) based on the parabolic curve to cover the whole coronal volume. The line-of-sight plasma density in each pixel square can be computed via:

$$n_i = \sqrt{EM_i/(A_i \cdot H_i)}, \tag{4.6}$$

here, n_i, EM_i, A_i and H_i are the number density, emission measure, area and column depth of each pixel. Then the thermal energy can be estimated as:

$$\sum_i E_i^{thermal} = \sum_i n_i \cdot k \cdot T_i \tag{4.7}$$

where k is the Boltzmann constant and T_i is the temperature of each pixel obtained from the filter ratio technique. The total thermal energy is estimated as $3.0 \times 10^{27} \pm 50\%$ ergs (see Figure 4.7).

4.6 Conclusions and Discussion

The photospheric vector magnetograms, G-band and coronal soft X-ray observations of two active regions, NOAA 10930 and 10963, are well covered by Hinode SOT and XRT observations almost synchronously when they are in flare-quiet periods near the solar disk center. The combination of the photospheric/coronal observations and non-linear force free magnetic field extrapolation provides a unique opportunity to study how changes in magnetic energy can be related to the corona heating. The author studied the temporal evolution of free magnetic energy, Poynting flux and total magnetic flux of the active regions during

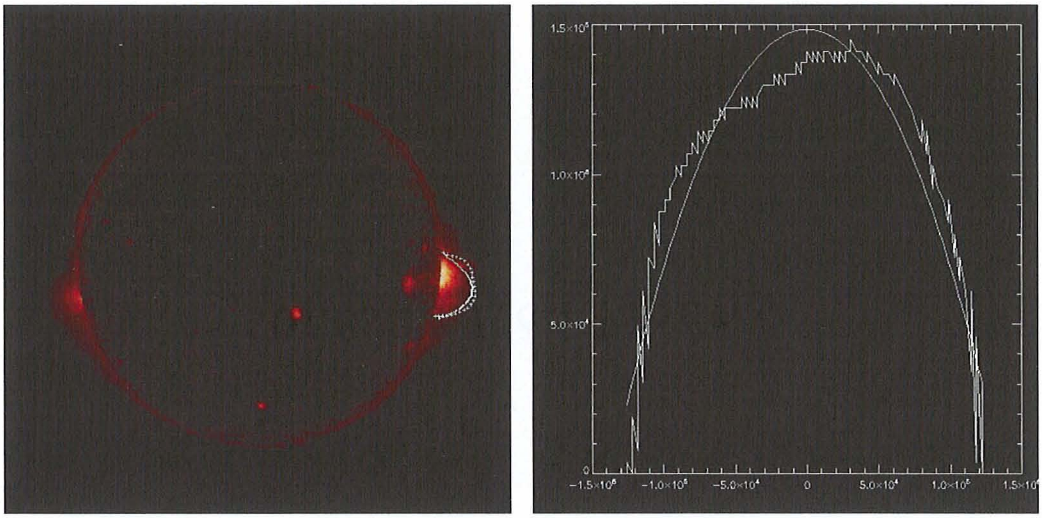

Figure 4.5 Fit coronal height via parabolic curve to estimate the column depth of NOAA 10963 when it rotated to the west limb. The image is from *SoHO* EIT 284 Å.

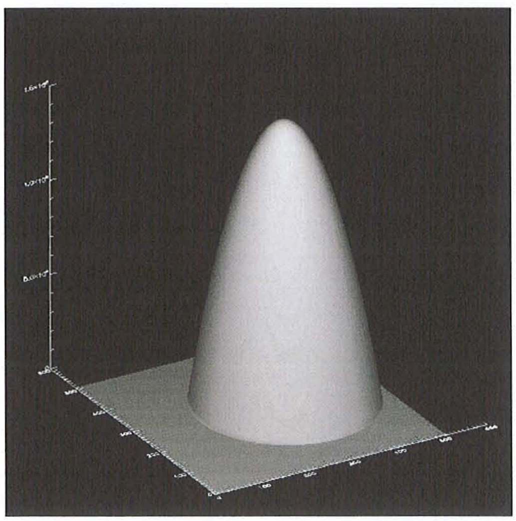

Figure 4.6 The artificial parabolic surface to cover the entire NOAA 10963.

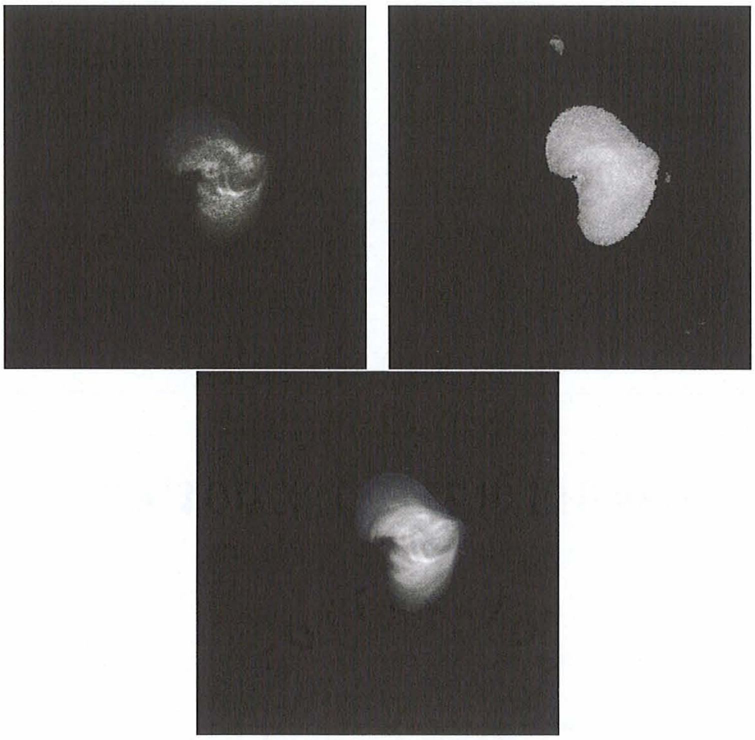

Figure 4.7 From left to right, the quantities are the maps of emission measure, temperature and thermal energy of NOAA 10963.

a period of 2-3 days when they were near the solar disk center, and compare them with the evolution of coronal heating properties including soft X-ray brightness, temperature and emission measure. Some techniques are utilized in this study, such as the local correlation tracking, the "minimum energy" method for the 180-degree ambiguity resolution and the optimization method for nonlinear force-free field extrapolation. In summary, from the analysis of the two active regions, the author draws the following conclusions:

(1) The unsigned total magnetic flux may not be the most important influencing factor of the free magnetic energy. The overall 3-D configuration of the magnetic field is important for magnetic energy storage. In NOAA10963, when the unsigned total magnetic flux decreases, the free magnetic energy keeps constant with small fluctuations.

(2) The evolutions of Poynting flux are highly coupled with the evolutions of unsigned magnetic flux. Instead of the velocity fields, the magnetic flux dominates the Poynting flux.

(3) The Poynting flux of NOAA10963 is about $1.0 \sim 4.0 \times 10^{29}$ ergs/s and free magnetic energy is about 7.0×10^{31} ergs, however the electron thermal energy is estimated about $3.0 \times 10^{27} \pm 50\%$ ergs. From both Poynting flux (Klimchuk 2006) and magnetic energy aspects, photosphere has the capability to generate sufficient coronal heating energy. However, the concern is the direction of the Poynting flux. It is well known that the energy flow, the Poynting flux, can go bi-directions, upward (outward the sun) and downward (toward the sun). The Poynting flux, $B_z \cdot \mathbf{B_h} \cdot \mathbf{V_h}$, where "$v$" and "$h$" signify vertical and horizontal, is essentially the energy going upward. If $\mathbf{B_h}$ is the same on the bottom and top sides of the plane where $\mathbf{B_h}$ and $\mathbf{V_h}$ are measured, then an equal amount of energy goes downward. This downward energy is not reflected. All information about the upward

energy flux is contained in the Eq. 4.2, with $\mathbf{B_h}$ on the top side of the plane (private conversation with Dr. Klimchuk). In this case, the obtained Poynting flux can be considered as propagation in upward direction to heat the upper corona.

(4) The evolution trends of coronal X-ray brightness (and average temperature) follow those of free magnetic energy more closely than total unsigned magnetic flux — suggesting that the free magnetic energy plays an important role to heat corona.

CHAPTER 5

THE EVOLUTION OF PHOTOSPHERIC MAGNETIC FIELDS INSIDE AND AROUND THE CORONAL HOLES

5.1 Introduction

Solar coronal holes (CHs) are the open magnetic field regions dominated by the uni-magnetic-polarity imbedded in the solar corona with lower plasma density and temperature than other regions (Wang et al. 1996). The CHs were discovered by the X-ray telescopes in the Skylab mission which were launched on 14 May 1973. Coronal holes, the origin of the fast component of the solar wind ($\sim$ 800 km s^{-1}) (Krieger et al. 1973), are linked to unipolar concentrations of open magnetic field lines. The magnetic field structure of CHs can be understood by simply applying potential extrapolation models using measurements of the photospheric magnetic field as boundary condition (Wiegelmann et al. 2005). Also Wiegelmann et al. (2005) showed that the closed magnetic loop in the CHs are much lower and flatter than those in the quiet sun regions (QSs). The CH magnetic field structure is the key to understand the CH physics, and ultimately to help to unveil the physical processes responsible for coronal heating and the solar wind driving. During solar minimum, coronal holes are usually found at the Sun's polar regions, sometimes they may be extended to the equatorial regions. The equatorial CHs can be either "isolated" among the QSs or connected to polar with an open magnetic flux channel (Kahler & Hudson 2002; Madjarska & Wiegelmann 2009). The polar region coronal holes can last for as long as a few solar rotations, but the equatorial CHs live shorter. In responding to the photospheric differential rotation, the difference between polar CHs and equatorial CHs is that the polar CHs rotate more slowly and rigidly, while the equatorial CHs rotate faster but more differentially.

The boundaries of equatorial CHs can usually be defined with various shapes (see Figure 5.1). The motions of equatorial CHs appear quasi-rigid rotations was reported by Timothy et al. (1975) and confirmed by Insley et al. (1995) and Kahler & Hudson (2002). While it is well known that the photosphere, the base of corona, rotates differentially. Consequently, it is straightforward that there should be magnetic shears between the photosphere and corona around the CHs and the shears would force the magnetic fields to be more dynamic. Even more importantly, magnetic reconnection may tend to occur in the CH boundary to maintain the CH integrity (Kahler & Hudson 2002; Fisk 2005). However, the CH boundary vertically passes the chromosphere, transition region, then corona. Wang et al. (1996) suggested the continuous field-line reconnection may happen in the corona. Nevertheless, the clue of the reconnection fingerprint should be pinned down to the photospheric magnetic field. These motivate us to investigate whether and where the signature of the dynamic evolution occurs in photospheric magnetic fields in and around CHs. The difference of magnetic dynamics in and outside CHs has been demonstrated by studying individual magnetic elements (Abramenko et al. 2006a; Zhang et al. 2006). Zhang et al. (2006) concluded that the appearance and disappearance of magnetic flux in QS regions are much more dynamic than inside the CHs. From Fisk (2005) model, the lower magnetic flux appearance rate in CHs is related to the formation of CHs. The lower magnetic flux disappearance rate in CHs implies lower magnetic reconnection rate. The study uses a statistical approach: the measurements of cross-correlation coefficient of magnetograms — are used as the indication of level of evolution and motion of magnetic fields.

This chapter is organized as follows: the data sets and the analysis method are described in §5.2. The results are presented and briefly discussed in §5.3.

5.2 Data Sets and Analysis

15 isolated equatorial CHs between August 21 2003 and December 30 2006 are selected. All the CHs are in the mature (stable or quasi-stationary) phase. The 15 CHs have a variety of shapes and areas (see Figure 5.1). Each CH had been tracked for more than 10 hours when they cross the solar disk center to minimize the projection effect. CHs are darker in radio wavelengths, extreme ultraviolet, and X-rays observation. The image of He I 10830 Å line is usually employed to diagnose the presence of CHs with opposite contrast because He I absorption is significantly weaker in CHs than in any other solar features in spectroheliograms (Harvey et al. 1975). However, in this study, due to the limitation in data set, EUV data are used instead. The He I 10830 Å triplet absorption line is formed in the upper chromosphere by the photoionization recombination and the collision, while the EUV 195 Å line is formed in the lower corona, about 70 Mm above photosphere (Aschwanden & Nitta 2000). In this study, the author uses the observations from Extreme ultraviolet Imaging Telescope (*EIT*) (Delaboudinière et al. 1995, 1997) on the Solar and Heliospheric Observatory (*SoHO*) to locate CHs. The *EIT* provides excellent spatial resolution ($2''.6$ pixel) observations in four EUV wavelength bands. The temperature response curve for *EIT* 195 Å mainly produced by spectral lines of Fe XII at 195.12 and 193.52 Å which peaks at 1.4 MK with a FWHM about 0.8 MK (Moses et al. 1997). Because of the formation height difference between He I and Fe XII, the shapes of CHs are slightly bigger in *EIT* observations. On the other hand, the CHs identified in EUV observations are slightly smaller than those identified in X-ray observations, because X-ray formation height is higher than EUV.

Therefore, the belt-shaped masks with certain thickness (say 20 arc second, see Figure 5.2) are used to define CH boundaries.

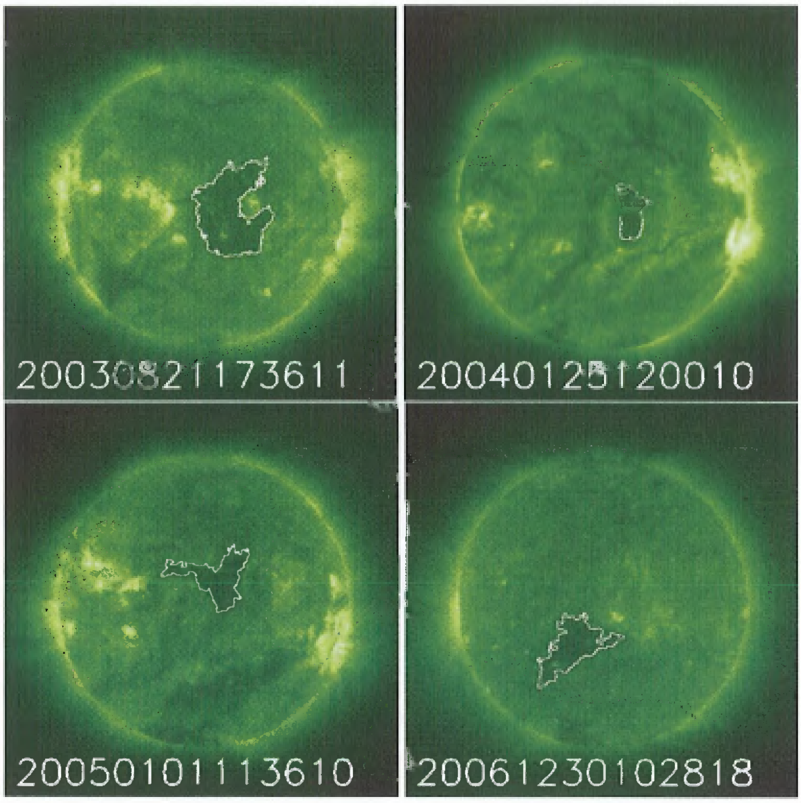

Figure 5.1 Examples of identified CHs on August 21, 2003, January 25, 2004, January 01, 2005 and December 30, 2006, respectively. The white contour shows the boundary of each CH. The background images are the *EIT* 195Å images.

The magnetic fields in the CHs are much weaker than active regions and the noise of the transverse magnetic fields is an order of magnitude higher than the longitudinal fields. Therefore no vector magnetograms available. The magnetic field evolution is analyzed by using *SoHO* Michelson Doppler Imager (MDI) data. *SoHO* MDI provides excellent full disk longitudinal magnetograms with the pixel size of 1.98 arc seconds, 1 or 96 minutes cadence and 20 Gauss noise level (Scherrer et al. 1995). MDI is sensitive to the photospheric absorption line Ni I 6768 Å with narrow bandwidth 94 mÅ. The Stanford MDI team provides re-calibrated magnetograms since 2008, that is used in this study. The author used one minute cadence MDI data and average the magnetogram every five minutes to reduce the noise. The author also smoothed each magnetogram with kernel of $10''$ by $10''$. The following steps are used to process data (see Figure 5.2): (1) identify the boundary by certain threshold on *EIT* 195Å data; (2) treat the thin closed boundary curve as the center of the boundary belt and expand the thin curve towards both sides $5''$ to form the boundary belt mask; (3) to minimize the differential rotation and projection effects, rotate or de-rotate (rotate back) the series of MDI magnetograms to the time when the *EIT* EUV image were observed by *ssw* routine *de_rotmap*; (4) superpose the boundary belt mask on the smoothed MDI magnetogram; (5) chop the coronal hole part, then get the isolated parts, e.g. inner coronal hole part and coronal hole boundary part (see Figure 5.3).

It is hard to visually distinguish the dynamic difference of magnetic fields inside the CH and on the boundary of CH when track them for tens of hours. The author quantitatively employed cross-correlation to manifest the difference. The cross-correlation coefficient can be computed as:

$$CC = \frac{\sum\limits_{x,y} A_1(x,y) \cdot A_2(x,y)}{\sqrt{\sum\limits_{x,y} A_1^2(x,y)} \cdot \sqrt{\sum\limits_{x,y} A_2^2(x,y)}} \tag{5.1}$$

The author can simply apply Mosher (1977)'s diffusion model under the assumption that the average motion is less than 0.14 km/sec. Then the CC can be manifested as a function of time t :

$$CC(t) = 1 - \sqrt{\pi D t}/1.7 r_0 \tag{5.2}$$

where, r_0 is the average radius of circular magnetic flux tubes $\sim$ 5000 km and D is the effective diffusion constant. Diffusion constant is a factor of proportionality representing

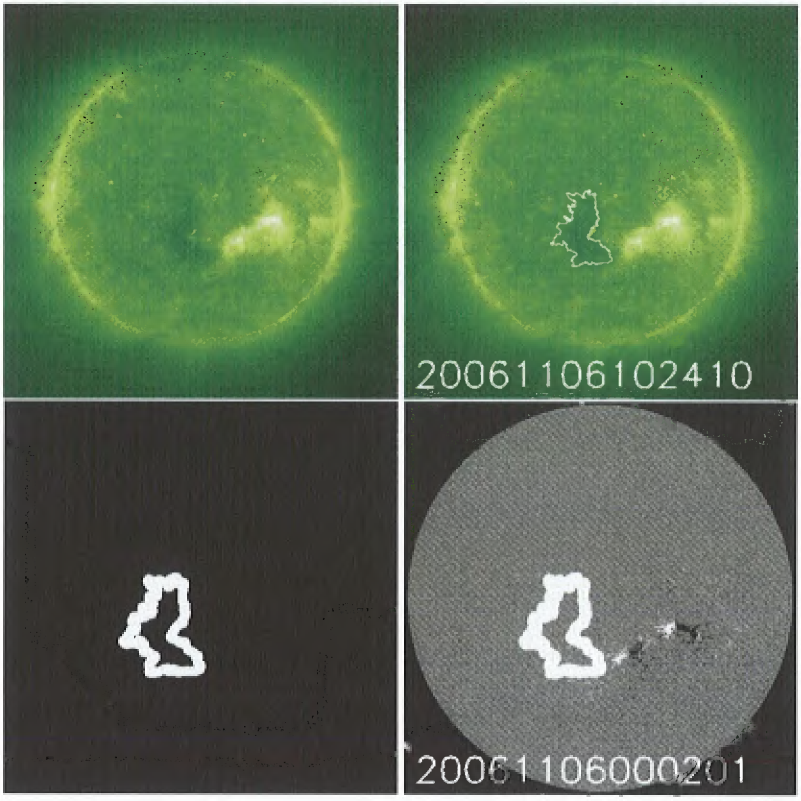

Figure 5.2 Figures illustrate the method of CH boundary identification and overlapping on the MDI magnetogram. This CH is on November 06, 2006. The upper left panel is the original *EIT* image. The upper right panel is the identification of the boundary of the CH. The lower left panel is the corresponding mask by image process technique. The lower right panel shows the MDI magnetogram overlapped by the coronal hole boundary mask.

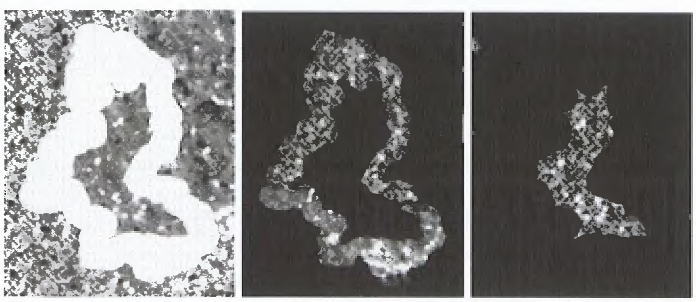

Figure 5.3 The isolated parts of the CH on November 06, 2006 on MDI magnetogram. This CH is dominated by positive polarity. From the left to the right are CH boundary mask overlapped on the magnetogram, the magnetic field on the CH boundary and inside the CH, respectively.

the amount of substance diffusing across a unit area in unit time. Then the evolution of the cross-correlation coefficient can be fitted by the curve as Equation 5.2. D is estimated by least-squares fitting according to Equation 5.2. The diffusion constant describes the dynamics of the fields, higher D, more dynamic (a sample, see Figure 5.4) the fields.

5.3 Results and Discussion

The author investigated the evolution of photospheric magnetic fields inside and around the boundaries of 15 CHs with a variety of sizes and complexities from August 21 2003 to December 30 2006. Each CH area was spatially divided into three parts (inside, outside and the boundary of the coronal hole), via image process techniques. As an example, the CH on November 06, 2006 is dominated by positive polarity. Figure 5.4 shows the evolution profiles of the inner CH magnetic field (purple asterisk) and the CH boundary magnetic field (blue asterisk). This CH was tacked for more than 10 hours, but this figure plots the evolutions of 400 minutes, since the distinguishable difference are obvious in 400 minutes. The asterisks are least-squares fit using the curves of Equation 5.2. The fitting found the diffusion constants to be 330 and 470 $km^2\ s^{-1}$, respectively. All the 15 fitting results are listed in Table 5.1. From 15 CHs analyzed (Table 5.1), the technique was successful in 11 cases. Eight of these 11 cases showed the magnetic fields on the boundaries of CHs are more dynamic than inside the CHs at the first several hours. Three of 11 CHs show the evolutions are similar in both areas. The rest four (e.g. events of 2003-08-21, 2004-02-29, 2005-01-19 and 2006-12-30) could not be fitted due to the unaccepted data gaps. This result suggests that the magnetic fields are indeed more dynamic on the CH boundaries than inside the CHs, likely due to the magnetic reconnections at the boundary that will be discussed later.

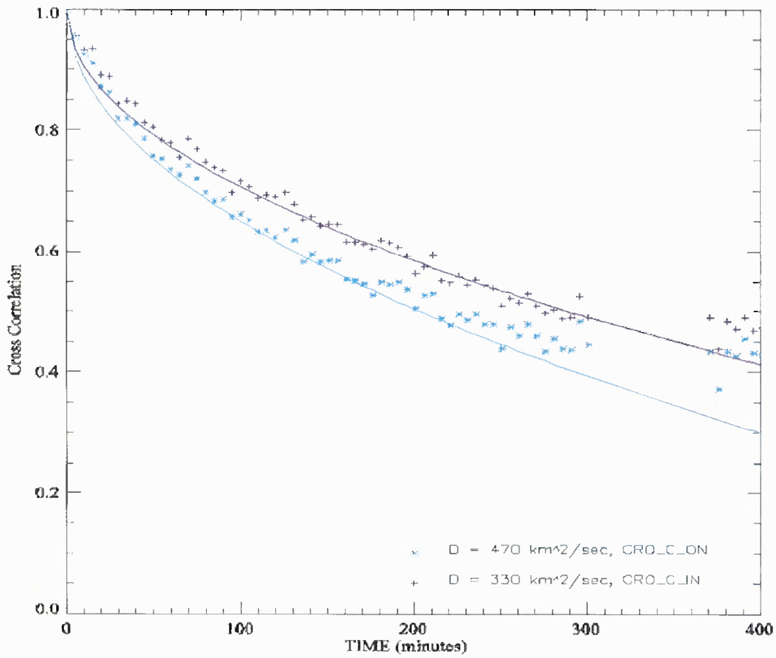

Figure 5.4 The evolution profiles of the auto cross correlations of the line-of-sight magnetic fields of the coronal hole (purple asterisk) and its boundary (blue asterisk).

The findings imply the magnetic field of equatorial CH boundary is more diffusive than that inside the CH. To maintain the integrity of the CH shape when rotation, the scenario could be: at the leading CH boundary (the west side), the CH open magnetic fields keep transporting and opening the frontal closed QS magnetic loops by reconnection; at the trailing boundary (the east side), the open magnetic fields keep closing themselves by changing the connectivity. It is a dynamic equilibrium in a macro-view. The open magnetic field lines can be transported by random walk associated with convection motions (granulation or supergranulation) below the photosphere (Wang & Sheeley 1994; Fisk 2005). How the whole integrity of CH moving is a mystery. Is there possibly a kind of large-scale convention motion underneath the CH?

Table 5.1: Comparison of the 15 Equatorial CHs Diffusion Constants

Events	Inside CHs D_{in} ($\pm$ 10 $km^2 \cdot s^{-1}$)	On the CH Boundaries D_{bdry} ($\pm$ 10 $km^2 \cdot s^{-1}$)
2004-01-25	400	600
2004-02-01	270	450
2005-01-01	330	330
2005-01-27	230	300
2005-02-24	150	200
2005-07-18	340	340
2005-07-26	400	500
2005-08-08	500	500
2005-08-14	230	370
2006-05-02	300	450
2006-11-06	330	470
2003-08-21	—	—
2004-02-29	—	—
2005-01-19	—	—
2006-12-30	—	—

Feldman et al. (1999) investigated the coronal hole boundaries and concluded that they are seeded with small-scale loops (loop length less than 7 Mm). There coexist, however, long loops with higher temperatures ($\sim$1.4 $\times$ 10^6 K) which generally originate from the same location but close at faraway from CHs. Madjarska & Wiegelmann (2009) draw a conclusion that small-scale ($10'' \sim 40''$ and smaller) loops known as EUV or X-ray bright points play a key role in coronal holes boundaries evolution at small scales. The emergence and disappearance of small-scale loops continuously occur on the CH boundaries. Therefore the magnetic reconnection happen mainly in these relatively small-scale loops or dipole structure, not change the long distant connectivity of long loop field lines. They also found there is no significant energy release during the dynamic reconnection of the small-scale loops. It is due to the weaker field strength of small loops and may imply the small-scale loops are not dense. The small-scale loops along CH boundaries have a main contribution to keep the CH shapes. Continuous magnetic reconnection between the open magnetic field lines of the CH and the closed field loops in the QS is more likely to take place at the CH boundary. This quasi-stationary pattern of reconnection process results in an exchange of footpoints between open and closed magnetic field lines without change in the total amount of open or closed flux (Wang & Sheeley 1994). If this scenario is true, one can conjecture that this kind of small-scale reconnection (or nanoflare, defined by Parker (1988)) occurs ubiquitously. Inside the CHs, fields are dominated in one polarity, therefore the small scale reconnection rate is much reduced — causing lower energy output, so CHs appear much darker.

CHAPTER 6

EVOLUTION OF OPTICAL PENUMBRAL AND SHEAR FLOWS ASSOCIATED WITH THE X3.4 FLARE OF 2006 DECEMBER 13

6.1 Introduction

It has been well established that large-scale solar eruptions, e.g., solar flares and coronal mass ejections (CMEs), are magnetic in nature. Magnetic energy accumulating in the corona due to photospheric motions and flux emergence is released during the eruptions, and the coronal magnetic field becomes less non-potential. As the lower boundary of the involved magnetic structure and the only layer where magnetic field is routinely observed, the photosphere may also display some variations in magnetograms. Therefore, studies of the magnetic structure evolution in solar active regions are vitally important to the understanding of the physics of solar flares and CMEs. In recent years, several observations showed convincing evidence that rapid δ-spot penumbral decays are associated with X-class flares, and the neighboring umbral cores are simultaneously darkening as well (Wang et al. 2002a,b, 2004a; Liu et al. 2005; Deng et al. 2005), confirming the early discovery revealed by Howard (1963). Spirock et al. (2002) reported the evolution of magnetic field, a rearrangement of the magnetic field in a projected configuration, associated with a X20 flare. Sudol & Harvey (2005) and Li et al. (2008) confirmed that optical intensity changes are tightly related with photospheric magnetic field variations in X-class flares. Later, Chen et al. (2007) surveyed over 400 events and statistically concluded the trend that the darkening is more concentrated near the flaring neutral line in larger flares. Wang et al. (2004a) proposed that magnetic fields in the penumbral decay areas partially change from more inclined to more vertical accompanying the occurrence of solar flare. Yurchyshyn et al. (2004) proposed that the tether-cutting model (Moore & Labonte 1980; Sturrock 1989; Moore & Roumeliotis 1992) can explain the stretching of outer field line and the formation of new field line near the flaring neutral line. In particular, the tether-cutting could interpret the enhancement of transverse fields after flare. Deng et al. (2005), on the other hand, explained the phenomenon in terms of the field lines turning to more vertical positions in the breakout model framework. During an X-class flare, the rearrangement of magnetic field structures would also induce mass motions in the magnetized solar atmosphere, therefore variations of the plasma motions are expected.

Inside a sunspot group, the photosphere manifests two kinds of notable optical motions. One is the Evershed flow in the penumbra, and the other is the shear flow along the magnetic neutral line between positive and negative polarities. Evershed effect, discovered by Evershed (1909), is height dependent, decreasing rapidly with the height (see e.g. Solanki (2003)). The Evershed flow carries magnetized gas (Solanki et al. 1992, 1994), and is restricted to the horizontal component of magnetic fields (Title et al. 1993; Degenhardt 1991). It was also found that Evershed flows begin to be visible when a penumbra forms (Leka & Skumanich 1998). This suggests that the Evershed flow pattern is coupled with the morphology of local magnetic fields. The speed of the Evershed flow should be measured spectrocopically (Shine et al. 1994; Tritschler et al. 2004; Sánchez Cuberes et al. 2005; Sánchez Almeida et al. 2007). However, the optical penumbral flow (which the author assumes is related to the Evershed flow) can be measured from imaging observations. The measurement of penumbral flow can provide information of Evershed flow. Naturally, one critical question is: is there a penumbral flow change associated with flares and the penumbral decay?

Shear flows, in photospheric and chromospheric layers, along the magnetic neutral lines can build up magnetic energy in flaring regions (Harvey & Harvey 1976; Amari et al. 2000; Yang et al. 2004). The moving plasma drags the magnetic field lines to form a non-potential magnetic topology, so the shearing motions are a signature of the accumulation of magnetic non-potentiality (Zhang 2001; Falconer 2001; Wang et al. 2006). The free magnetic energy will be released and the potential configuration will be restored after the sheared field reaches its critical point. Furthermore, shear motions could accumulate the magnetic helicity (Chae 2001) and form magnetic "channel" structures (Zirin & Wang 1993). Denker et al. (2007) concluded that the shear flows are commonly presented in complex sunspots but not related to the local magnetic shear. However, it is still not clear whether the shear flow can be affected by the energy releasing process during solar flare.

With the above two questions in mind, the changes of optical penumbral flows and shear flows associated with the X3.4 flare on 2006 December 13 are investigated. In §6.2, the data set and the processing are described. The results are presented in §6.3, which is followed by discussions in §6.4.

6.2 Observations and Data Analysis

On 2006 December 13, which was close to the recent solar minimum, an X3.4-class two-ribbon flare erupted in the active region AR10930. The flare event, which was associated with a halo CME, was observed by various ground-based and space-borne telescopes, and has been studied extensively. The recently launched Hinode mission (Kosugi et al. 2007) provides unprecedented continuous high resolution observations of the solar atmosphere.

The Solar Optical Telescope (SOT) (Suematsu et al. 2008; Tsuneta et al. 2008) on board Hinode provides G-band (430.5nm) images through the Broadband Filter Imager (BFI) and *Stokes-V* (Fe I 630.2nm) observations from the Narrowband Filter Imager (NFI). In this paper, the author concentrates on the variation of the flow motions in the source region, using the SOT G-band and *Stokes-V* data. The main data set is selected from 01:00:32 to 04:36:37 UT on 2006 December 13, covering the peak time of the X3.4 flare at 02:14 UT. In addition, the data from 20:44:36 on 2006 December 11 to 00:58:40 on 2006 December 12 are analyzed for comparison to a flare-free period. The pixel sizes are $0''.109$ (G-band) and $0''.16$ (*Stokes-V*), or the nominal resolutions are about $0''.218$ arc sec (G-band) and $0''.32$ arc sec (*Stokes-V*). The cadence for both observations is 2 minutes. The field of view is about $100'' \times 100''$. The 2-min cadence data offers a possibility to measure the plasma motions in the photosphere with the local correlation tracking (LCT) method (November & Simon 1988; Simon et al. 1988).

For the LCT calculations, the sequence of images was aligned and registered to remove drifts and occasional jumps from the Hinode tracking system. The author then used a technique similar to that of Simon et al. (1988). It works by comparing bounded cells in each image with the same cells in the subsequent image. The rigid shift that gives the best match for each cell pair is interpreted as an (x, y) offset for the center of the cell. The shifted cells are apodized with a centered Gaussian. The cell centers are spaced $0''.109$ apart for the G-band images. The FWHM of the 2-D Gaussian apodization is twice this and hence the resolution is also about twice the cell spacing. Even though seeing is not an issue with Hinode data, there is still noise in the LCT velocities resulting from random motions, oscillations, and perhaps photon noise. Hence, each cell is binned by around 4 by 4 grids.

Also, a running temporal averaging was applied to reduce the noise in the individual LCT signals. The temporal window applied is 20 minutes, which includes 11 successive velocity maps. These are averaged and the ending time of each time window is assigned to the mean velocity field. Because portions of the areas contain motions other than the penumbral flows, the author used a threshold of 0.2 km s^{-1} to eliminate low amplitude motions and also reject any vectors that were not within 90 degrees of the nominal outward direction. Only the selected vectors were taken into account for average velocity calculations. This makes the result a better measure of the optical penumbral flow.

Limb darkening is an effect of the solar atmospheric temperature gradient (Milne 1921). Correction of the limb darkening should be the very first step of this study. However, the G Band is not a continuum window but heavily populated with lines. Motivated by Langhans & Schmidt (2002), the author selected a calibration line in a pure granulation area (see Figure 6.1), and fit the G-band intensity along the straight line with a fifth order polynomial in the variable μ, i.e., $I' = c_0 + c_1\mu + c_2\mu^2 + c_3\mu^3 + c_4\mu^4 + c_5\mu^5$, where I' is the best fitted intensity along the calibration line, and $\mu = \cos\theta$, θ is the angular central meridian distance. The coefficients resulting from the fitting are $c_0 = -3.60350 \times 10^6$, $c_1 = 1.64239 \times 10^7$, $c_2 = -2.73969 \times 10^7$, $c_3 = 1.89836 \times 10^7$, $c_4 = -3.35536 \times 10^6$, and $c_5 = -1.05473 \times 10^6$, respectively. Then, each pixel of the original G-band image is corrected by the below formula:

$$I = (I_m - I') + 1500 \tag{6.1}$$

here, I_m is the measured intensity and 1500 is a biased constant to make I positive and closer to I_m.

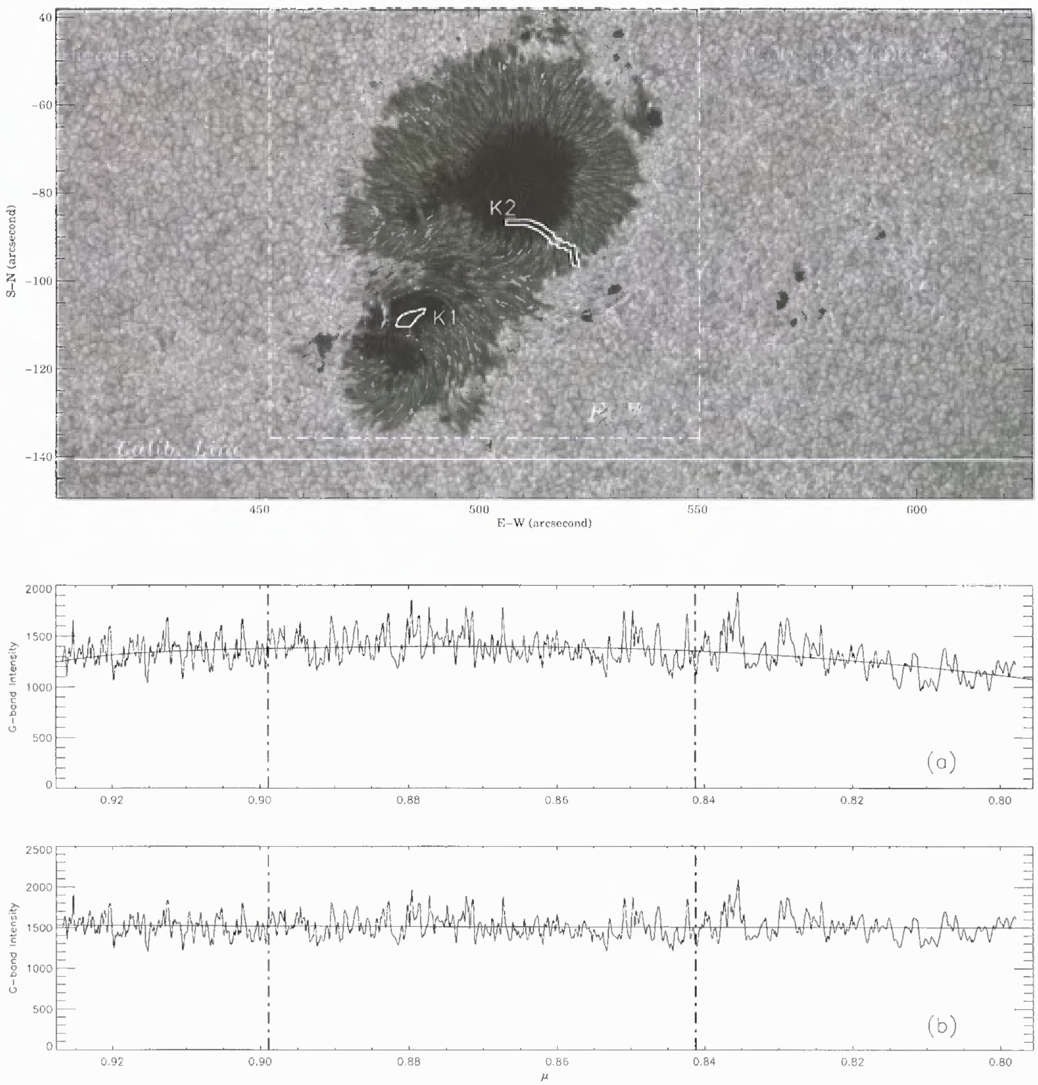

Figure 6.1 Correction of E-W limb darkening effect. The top panel is the Hinode SOT G-band image on 01:00:32 UT 2006 Dec. 13. The calibration line (white solid line) indicates the position where the G-band (430.5nm) intensity is fitted along. The calibration line contains only pixels with quiet Sun granulation. The dotted-dash box is the FOV focused in this study. Contours K1 and K2, derived from G-band difference image, indicate positions of flare kernels. Panel (a) is the original intensity along the calibration line versus μ ($\cos\theta$). The black solid line is the fifth order polynomial fitting. Panel (b) shows the corrected intensity and the best fitting.

The raw intensity images give us projected features in the plane of the sky because the active region is located around S05W33. The real pixel size and the derived velocities are subject to foreshortening. Therefore, the author constructed the image in the heliographic plane and de-rotated the image sequence to the disk center to mainly justify the pixel size shrinkages in solar latitude and longitude (similar to Gary & Hagyard (1990)) (see Figure 6.2). Thus the projection effect is removed and the LCT sampling window and Gaussian weighing function can be symmetric.

Using the LCT method, the G-band images are processed to derive flow motions in the entire field of view (FOV). For the shear flow along the magnetic neutral line, the *Stokes-V* images are co-registered (or overlapped) in order to distinguish the positive and negative magnetic elements and then to separate their velocities. Here, the author defines the shear velocity as the difference between positive and negative polarity elements in the direction parallel to the complex of magnetic neutral line (Wang 2006), i.e.,

$$V_{shear} = \overline{V}_{pos} - \overline{V}_{neg} \tag{6.2}$$

where $\overline{V}_{pos}$ and $\overline{V}_{neg}$ are the mean velocities of the positive and negative magnetic elements parallel to the magnetic neutral line, respectively. Both the velocities are projected in the direction of the neutral line. Note the shear velocity is the relative speed between positive and negative magnetic elements along the neutral line. A positive V_{shear} means that the shear flow (or relative velocity between positive and negative magnetic elements) direction is clockwise for this specific case.

In this study, the penumbral decay is quantitatively described by the difference intensity which can be calculated by the formula below:

$$I_{diff}(t) = \overline{I(t) - I(t_0)} \tag{6.3}$$

where $I(t)$ is the G-band intensity of each area at time t and t_0 is the start time of the observation. The average velocity of the flow depends on the velocity vectors selected. The average difference intensity depends on the area selected.

6.3 Results

The G-band images before the flare (at 01:00:32 UT) and after the flare (at 04:36:37 UT), are plotted in the left and middle panels of Figure 6.3, respectively. The difference image is shown in the right panel, where the significant enhancement of difference intensity in the bright areas near the penumbra indicates that the penumbra locally decayed after the flare and intensity dimming indicates that the penumbra is locally enhanced. It is seen that, contrary to the flare ribbons that appeared along the common penumbra between the upper and lower sunspots and flare kernels usually located in the strong magnetic fields (see kernels K1 and K2 in Figure 6.1), the penumbral decay is significant mainly on the outer side of the sunspot group, i.e., the north side of the upper sunspot and the south side of the lower sunspot, consistent with previous studies (e.g., Wang et al. 2004a; Liu et al. 2005; Deng et al. 2005).

The difference image in Figure 6.3 is spatially smoothed by a kernel of $2''.2$. The bright areas, labeled A1, A2, A3, A4, N1, N2, and defined by blue contour lines, are penumbral decay areas, and the dark area (labeled as D) defined by the red contour line

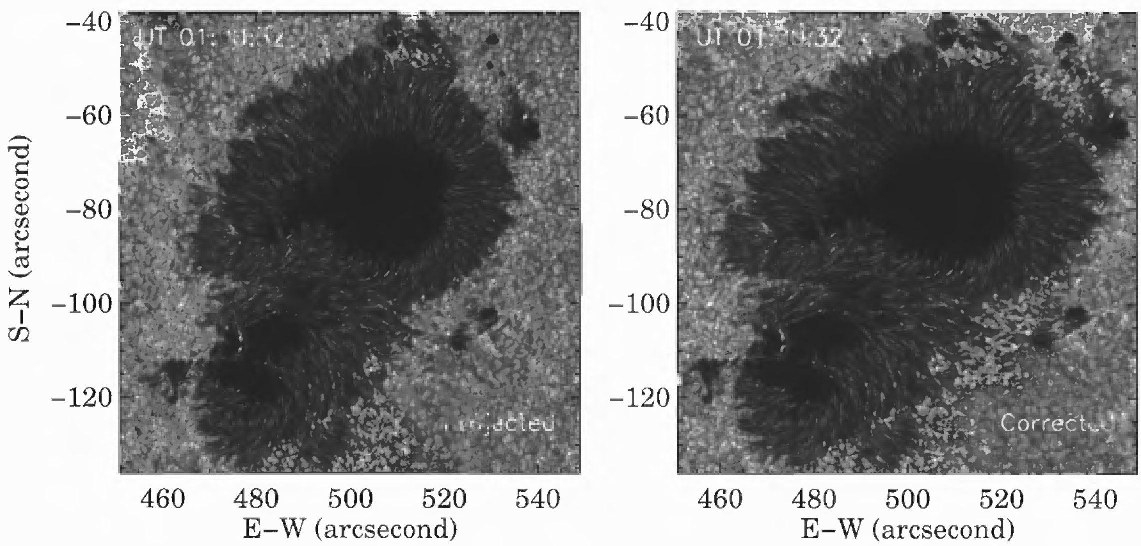

Figure 6.2 Comparison of original and projection corrected images. The left panel is the original (or projected) G-band image on 01:00:32 UT 2006 Dec. 13. The right panel is the projection corrected (or deprojected) image.

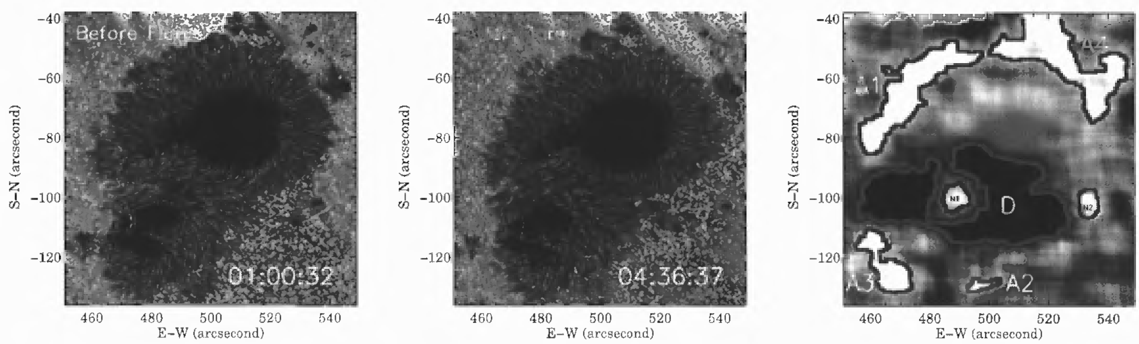

Figure 6.3 The left panel is the G-band image before the X3.4 flare on 01:00:32 UT 2006 Dec. 13. The middle one is the image after the flare on 04:36:37 UT 2006 Dec. 13. The right panel is the difference image (postflare image minus preflare G-band image). It was smoothed with a kernel of 20 $\times$ 20 pixels. The blue areas (A1, A2, A3, A4, N1, N2) are penumbral decay areas. The red region (D) is the penumbral enhanced area.

represents the penumbral enhancement area. Area N1 is located in the common penumbra, while the difference intensity enhancement of area N2 is due to fast motion of a pore structure. The author only took account of major enhanced areas (A1, A2, A3, A4) in this work.

The penumbra decay areas are outlined in Figure 6.4 by white curves. The boundaries of areas A3 and A4 are manually modified to avoid the pores. For comparison, the author selected a non-decay area, labeled as A5. The horizontal flow field at 01:10:33 UT, which is derived from consecutive G-band images with the LCT method, is over-plotted as vector arrows. It is seen that the flows in the selected areas are mainly radially outward along the penumbral fibrils, which is a typical feature of the penumbral flow in most penumbrae. However, in the common penumbra between the north and south sunspots, the photospheric motion significantly deviates from radial and is nearly tangent to the rotating sunspot to the south. Note that the measured granular LCT speed is mainly between 0.5 to 1 km s^{-1}, which is comparable with previous results of 650 m s^{-1} (Wang et al. 1995) and 700 m s^{-1} (Berger et al. 1998).

The temporal evolutions of the mean values of the G-band intensity (*diamonds*) and the penumbral flow velocity (*black asterisks*) for the five selected areas are displayed in Figure 6.5. The flare peak time is indicated by a vertical dashed line in each panel. Panel 1 reveals that in the area A1, the penumbral intensity was almost constant before the flare and it started to increase near the flare peak time. One hour later, the G-band intensity increased to its maximum. Correspondingly, the penumbral flow in the same area, showed a trend of decreasing from ~ 0.96 to ~ 0.85 km s^{-1} on average in the observation time window with visible oscillations. The evolutions of the G-band difference intensity and the

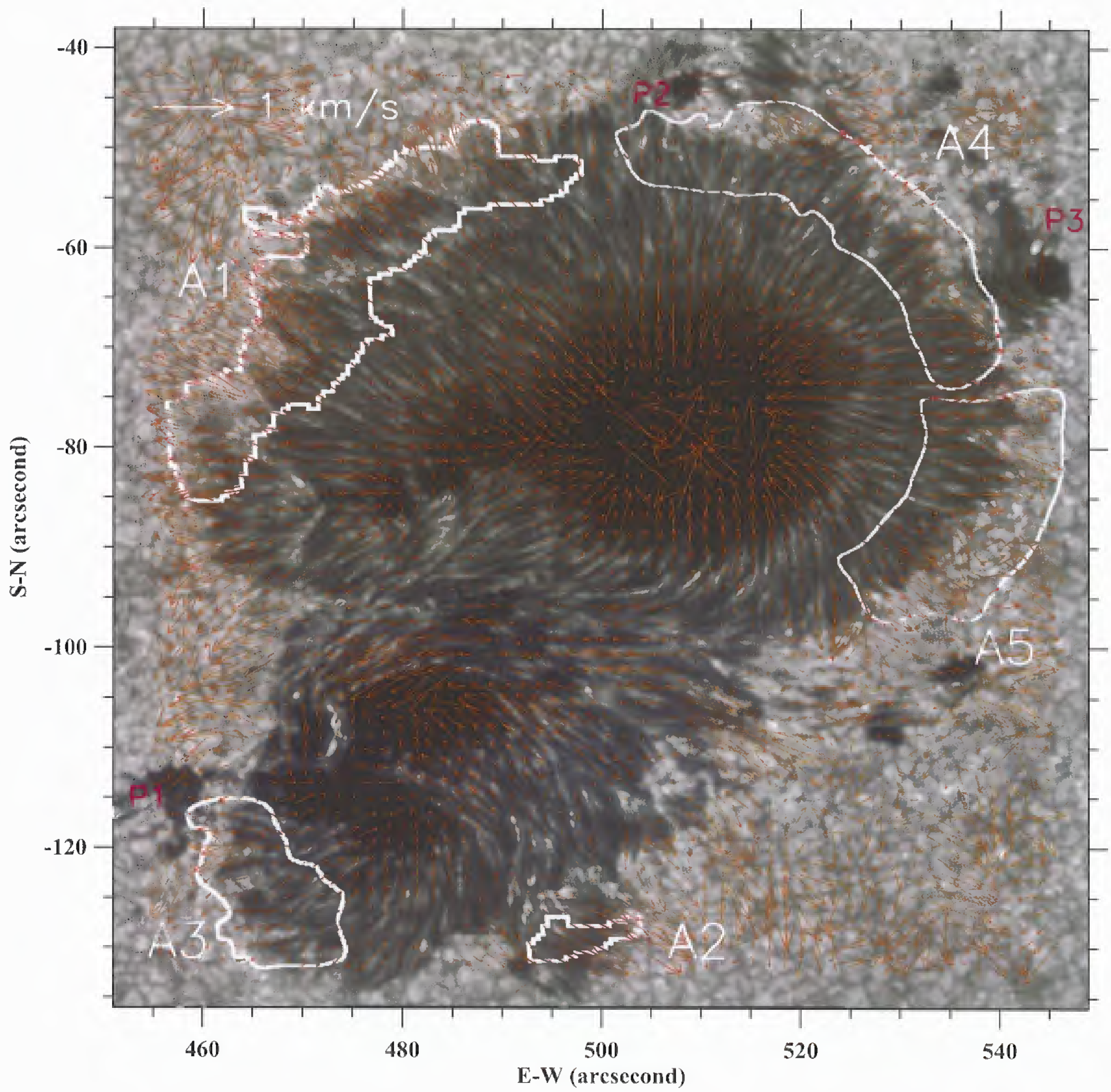

Figure 6.4 The G-band image flow map on 1:10:33 UT 2006 Dec. 13. The areas (A1, A2, A3, A4) are penumbral decay areas corresponding to the markings in Figure 6.1. The area A5 is a reference area that the penumbra did not change much after the flare. The orange arrows indicate the magnitude and direction of flow velocity. The pink labels P1, P2 and P3 are the major pores.

penumbral flow in area A2 (*panel 2*) show a similar behaviour, but with a systematic delay of $\sim$ 20 min. The magnitude of the penumbral flow decreased from $\sim$ 1 to 0.9 km s^{-1}. The G-band difference intensity increases after the occurrence of the flare in both areas A3 and A4. However, the penumbral flow velocity stays almost invariant in area A3 about $\sim$ 0.6 km s^{-1}, and varies from $\sim$ 0.70 to $\sim$ 0.77 km s^{-1} in area A4 across the flare peak. For comparison, the author plotted the evolution of the mean values of the G-band difference intensity (*diamonds*) and the penumbral flow velocity (*black asterisks*) of area A5 in panel 5 of Figure 6.5. It is seen that both quantities do not show significant variation across the flare peak, except that the penumbral flow velocity shows a slight trend of increasing oscillation amplitude.

The plasma motion in the common penumbra between the positive sunspot (the northern one) and the negative sunspot (the southern one) is driven by gradual rotation of the negative sunspot. This is manifested as a shear flow along the magnetic neutral line as shown mainly in the common penumbral area (see Figures 6.4 and 6.6). Figure 6.7 shows the evolution of the mean difference of the shearing velocity between the positive and negative magnetic elements in the region A6 that is enclosed by a white box in the right panel of Figure 6.6. The mean velocity difference decreased from $\sim$ 0.6 km s^{-1} 30 min before the flare peak to $\sim$ 0.3 km s^{-1} 30 min after the flare peak. The shear flow in the common penumbra is also oscillating, with a quasi-period of $\sim$ 50 min, which is almost identical to or slightly longer than those in the areas shown in Figure 6.5.

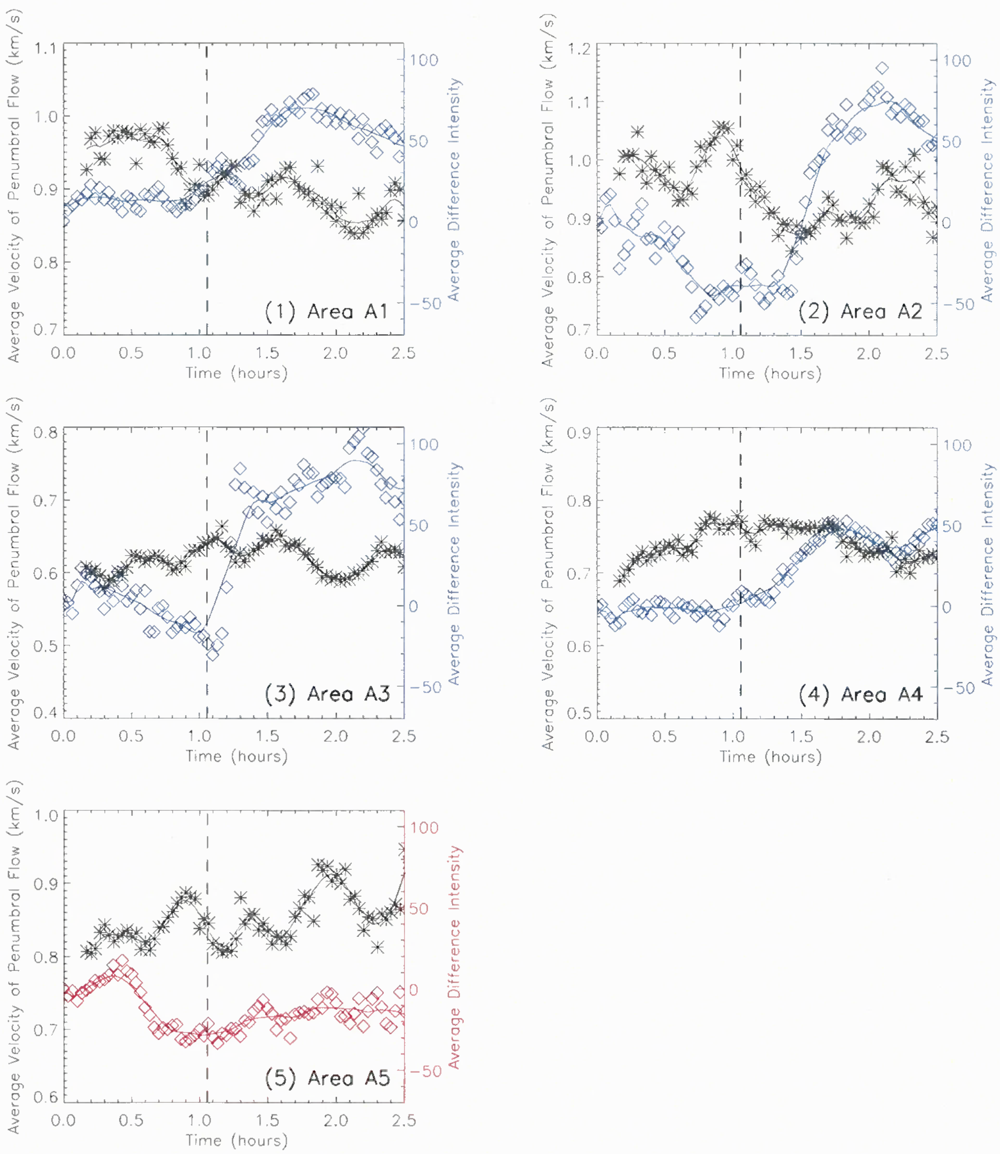

Figure 6.5 The time profiles of penumbral flows and G-band intensities. The black asterisks represent the magnitudes of the average velocity of horizontal penumbral flows in each area. The diamonds are the average difference intensities of each area. The solid curve shows the evolution tendency of each area. Panels (1) - (5) correspond to the areas A1 - A5 in Figure 6.2. The start time of plots is 1:10:33 UT 2006 Dec. 13. The vertical dashed line indicates the flare time. The red color represents the intensity in the reference region.

6.4 Discussion

By comparing the G-band images before and after X-class flares, Wang et al. (2004a); Deng et al. (2005) discovered penumbral decays associated with the eruptions. Such a feature was confirmed to be quite common in strong flare events (Liu et al. 2005). With the help of the optical observations by the newly launched Hinode satellite, the author can study the timely evolution of the penumbral decay for the first time. In this chapter, the author analyzed the optical data for the X3.4-class flare on 2006 December 13. The author found that while the two-ribbon flare appeared along the magnetic neutral line between the bipolar sunspots, the penumbral decay areas were basically located on the outer side of each sunspot, as indicated by Figure 6.3. In each segment of the penumbral decay areas, the G-band intensity was seen to increase for $\sim$50-70 DN after the flare peak, with a relative amplitude of $\sim 6-8\%$. It should be noted here that the penumbral decay studied in the earlier papers (e.g., Wang et al. 2004a; Deng et al. 2005; Liu et al. 2005) was usually associated with umbral darkening, which is absent in this case as implied by Figure 6.3. However, the absence of umbral darkening is actually not rare. According to the recent statistical research, quite a lot of penumbral decay events did not show umbral darkening (Chen et al. 2007). The difference can be understood as follows: According to Wang et al. (2004a) and Liu et al. (2005), the penumbral decay is attributed to the rearrangement of magnetic field from being more horizontal to more vertical during solar eruptions. While the penumbral magnetic field is significantly re-directed, the transverse field will be enhanced near the magnetic neutral line, that would influence the umbral magnetic fields and lead to umbral darkening. However, if the common penumbral magnetic field horizontally changes its direction by a small angle during the solar eruption, it would not affect the umbra that much, as in this case.

As mentioned above, the penumbral decay was explained by Wang et al. (2004a) to be produced when the more inclined magnetic field lines are stretched upward to become more vertical during the CME/flare eruptions, which was confirmed by recent vector magnetogram observations (Li et al. 2008). Since the outer penumbral flows tend to appear in areas with nearly horizontal magnetic field (Title et al. 1993), the author expected to see a decrease of the outer penumbral flow associated with the magnetic field line stretching in the penumbral decay areas. During the quiescent stage, the penumbral flow was found to be oscillating with periods ranging from several up to 40 min (Shine et al. 1994; Rimmele 1994; Georgakilas & Christopoulou 2003; Cabrera Solana et al. 2007) which is consistent with the observation. Besides the intrinsic oscillation behavior, changes in fine structures might also be attributed to some residual jitters because of the limitations of LCT techniques (Simon et al. 1995). As indicated in Figure 6.5, among the four segments with penumbral decay, the areas A1 and A2 did show a significant decrease in the penumbral flow after the occurrence of the strong flare. The mean value of the optical penumbral flow velocity decreased by ~ 0.1 km s^{-1} (about 10%) for both segments. However, the mean velocity of the penumbral flow in the areas A3 and A4 was almost constant across the flare event despite the penumbral decay. It is noted that a rotating pore (P3 in Figure 6.4) was located near the segment A4, and the other segment A3, as a part of the fast rotating positive sunspot, was in dynamic evolution. Therefore, the unexpected behavior of the penumbral flow in these two segments is probably due to the dynamic evolution in the surrounding photosphere. More surprisingly, the mean velocity of the penumbral flow in the area A5 (an area with relatively constant intensity) increased by ~ 0.1 km s^{-1} across the flare occurrence.

The Evershed effect manifests itself in Doppler shifts and asymmetries of spectral lines. Therefore, it can be determined reliably only based on spectroscopic observations. However, the author assumed that there is a relationship between the optical penumbral flows and the Evershed flow. Fortunately, there are two observations from Hinode/SOT spectro-polarimeter (SP) near the X3.4 flare with 8 hr temporal interval. One is at 20:30 UT 2006 Dec. 12 before the flare, the other is at 04:30 UT 2006 Dec. 13 after the flare (see Figure 6.8). The bottom two images are the dopplergrams measured from the doppler shift at wavelength 6301.5 Å. Table 6.1 presents the variation of Evershed flows in selected areas which is consistent with the variation of optical penumbral flow. The optical penumbral flow and the Evershed flow both decreased about 10% in area A1 and A2 after the major flare.

In order to further confirm that the variations of the penumbral flow and the penumbral intensity were associated with the CME/flare eruption, the author investigated the temporal evolution of the same sunspot group one day before the CME/flare eruption, when it was flare-free. Two patches of the penumbra are selected and labeled as "B1" and "B2" in the left panel of Figure 6.9. The evolution of the G-band difference intensity (*diamonds*) and the penumbral flow velocity (*asterisks*) for the two patches are displayed in the middle and right panels. Note that the average value of the G-band intensity in the 4-hr data set is subtracted from the observed intensity to obtain the difference intensity. Both the difference intensity and the penumbral flow velocity were clearly oscillating, with amplitudes of $\sim \pm 40$ DN and $\sim \pm 0.09$ km s^{-1}, respectively. However, both quantities did not show any trend of increasing or decreasing during 4 hours. This reinforces the idea that the

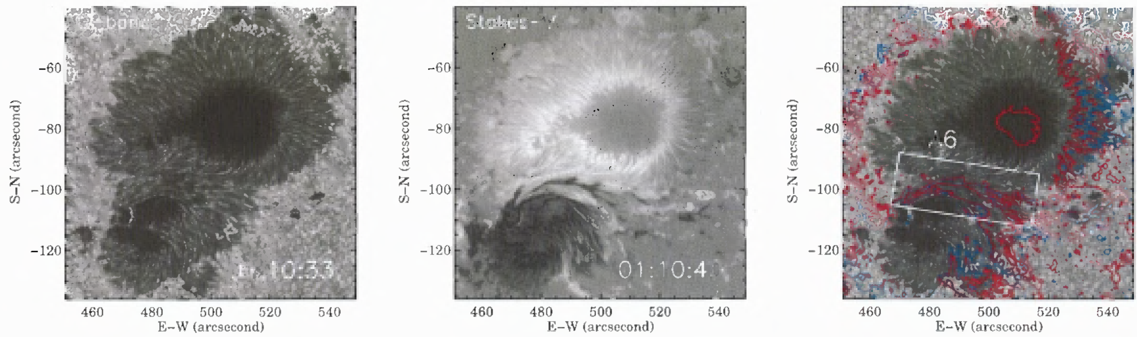

Figure 6.6 The left panel is the G-band intensity on 1:10:33 UT 2006 Dec. 13. The middle one is the co-aligned corresponding *Stokes-V* data (Fe I 630.2nm). The right panel is the G-band image contoured with *Stokes-V* image. The red contour represents positive polarity and the blue is negative. The boxed area A6 is the strong shear flow region.

Table 6.1: Variation of Doppler Velocities in Selected Areas Before and After the Flare

	A1	A2	A3	A4	A5
Before (km/s)	-4.23 [a]	-2.47	-3.76	-3.16	-2.92
After (km/s)	-3.80	-2.17	-3.76	-3.16	-2.86
Decrease	10.2%	12.1%	-	-	2.1%

[a] These values are area-averaged. The negative sign means the direction is from the sun towards the observer. Poor fitting points are removed.

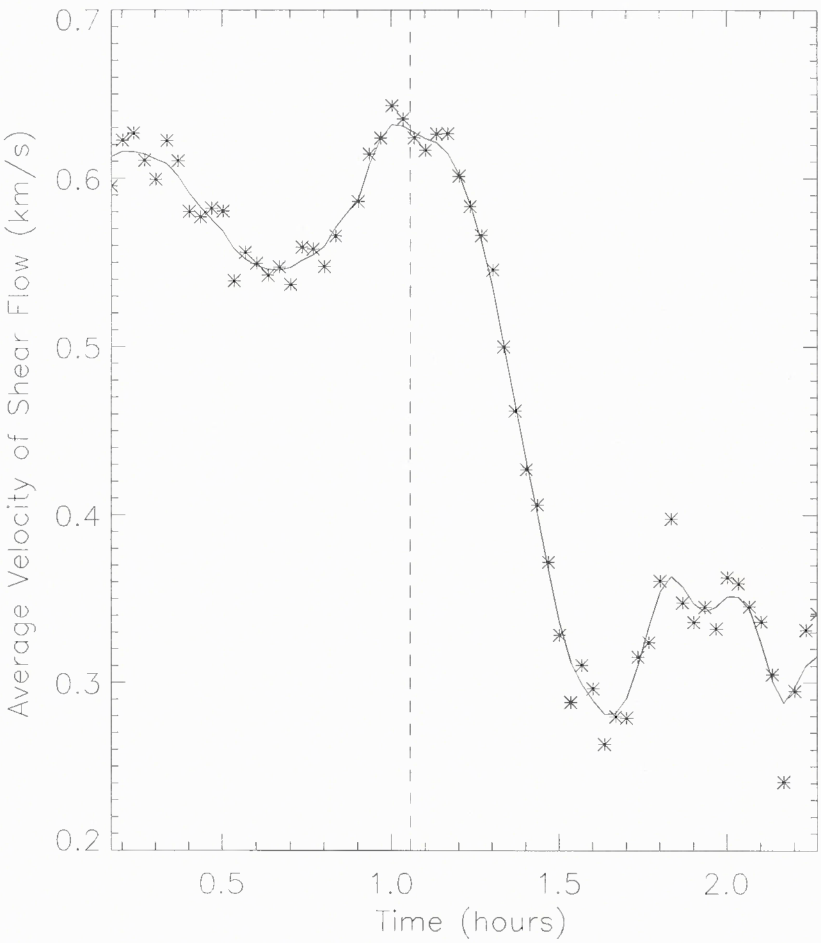

Figure 6.7 The evolution of shear flows covering the flaring period. The asterisks represent the average velocity of shear flows in the box area A6 in Figure 6.6. The start time of plot is 1:10:40 UT 2006 Dec. 13. The vertical dashed line indicates the flare time.

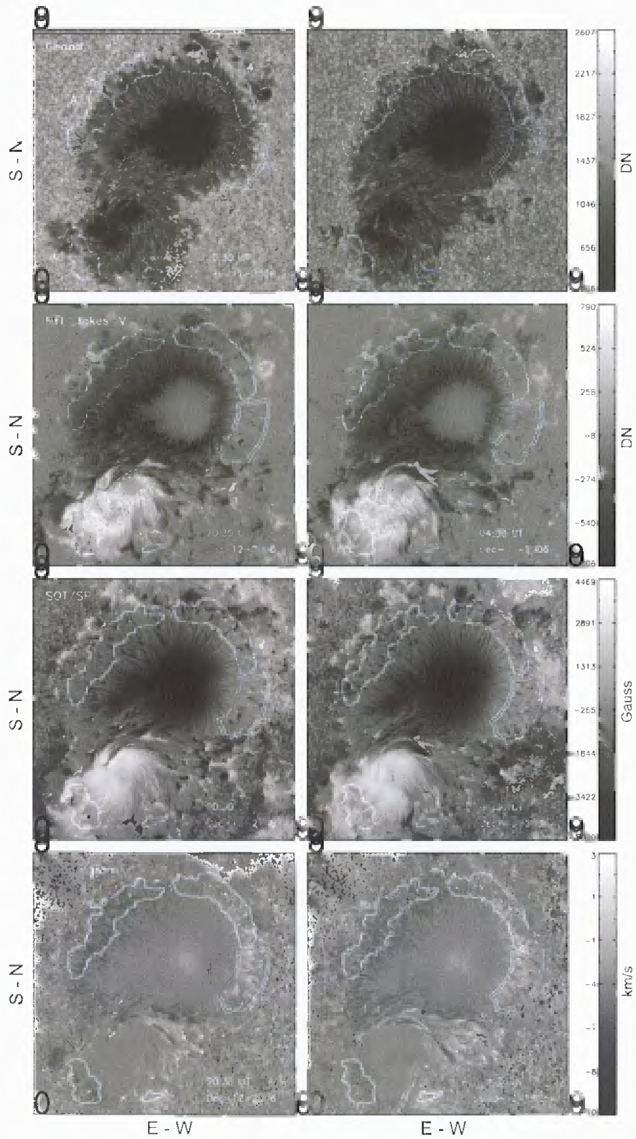

Figure 6.8 The images in the left column are at 20:30 UT 2006 Dec. 12 (before the major flare). They are G-band, Hinode/SOT *Stokes-V* from NFI, Hinode/SOT spectro-polarimeter (SP) magnetogram and Hinode/SOT SP dopplergram, respectively from top to bottom. The images in the right column are at 04:30 UT 2006 Dec. 13 (after the major flare). The areas (A1, A2, A3, A4, A5) are the areas corresponding to the markings in Figure 6.2.

penumbral decay and the penumbral flow decrease in segments A1 and A2 are intimately associated with the CME/flare eruption, or more precisely, they are caused by the stretching of the magnetic field lines associated with the CME/flare eruption.

Shear flows are often present along the magnetic neutral line, which is responsible for the energy built-up in active regions (e.g., Wang 1992). In the event analyzed in this paper, the magnetic neutral line happened to be along the common penumbra of the sunspot group. Therefore, shear flow showed also some features present in the penumbral flow, e.g., the quasi-periodic oscillation of the flow velocity as indicated by Figure 6.7. The striking feature shown in this figure is that the shear flow velocity dropped down rapidly from ~ 0.6 km s^{-1} to ~ 0.3 km s^{-1} in association with the CME/flare eruption. This can be understood as follows. Before the CME/flare event, magnetic shear was increasing continuously due to the rotation of the southern sunspot (Zhang et al. 2007). As the non-potentiality increases, the magnetic system in the corona approached a critical point, after which it became unstable. The stored magnetic energy was then released to be manifested as the CME and flare, during which the magnetic field lines were un-twisted. As a result the shear flow speed decreased. In other words, the decrease of the shear flow speed across the magnetic neutral line could be regarded as a signature of the magnetic energy relaxation. It should be noted that the shear flow slowed down, but did not stop. It kept moving in the original direction even after the CME/flare eruption. Probably it is such a continual shear flow along the magnetic neutral line that led to the increase of the magnetic shear in the photosphere after the flare, compared to the pre-eruption stage 8 hr earlier, as found by Jing et al. (2008). It was, however, noted by (Denker et al. 2007) that the photospheric shear flow along the magnetic neutral line was not related to any change of the local magnetic shear in their case. They emphasized the important role of the global magnetic twist of the δ spot field.

In summary, for the first time, the author tracked the evolution of the penumbral decay process associated with a CME/flare eruption with 2-min cadence from space, and found that the eruption was also accompanied by a decrease of the optical penumbral flow and the Evershed flow in the penumbral decay areas. Both features are probably the direct signature of the magnetic field stretching in the CME eruption. It is also found that the shear flow across the magnetic neutral line decreased in response to the magnetic energy release.

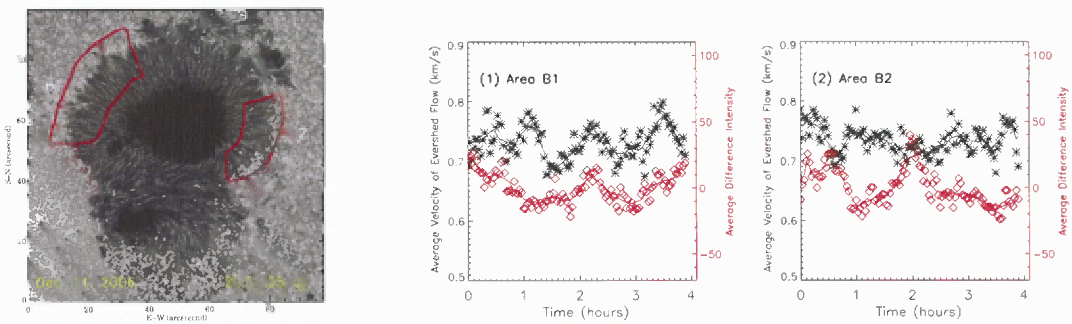

Figure 6.9 The left panel is the G-band image on 20:54:35 UT 2006 Dec. 11. The red patches (B1, B2) are the reference penumbral areas. The middle and right panels are the evolutions of penumbral flows covering four-hour flare quiet time interval in areas B1 and B2. The start time of plots is 20:54:35 UT 2006 Dec. 11.

CHAPTER 7

SUMMARY OF THE DISSERTATION

This dissertation focused on the relationship between photospheric magnetic fields and solar coronal activities. According to the different temporal scales, the coronal activities can be classified into two categories: steady heating and transient eruptions. The major conclusions are summarized below, with respect to the two distinct coronal activities.

Over six decades ago, the solar coronal temperature was inferred to be about a million Kelvin when Bengt Edlén and Walter Grotrain identified Fe IX and Ca XIV lines from the spectrum of the Sun (Edlén 1943). This is opposite to the traditional idea that the coronal temperature should steadily drop from the chromospheric temperature with increasing height if there were no other heating sources because of the strong coronal thermal conduction and radiation loss. Since then, the problem of coronal heating remains as an important problem in coronal physics. In this dissertation, a statistical study was conducted to investigate the the relationship between coronal X-ray brightness and five photospheric magnetic parameters (1) the length of strong-gradient magnetic neutral lines, (2) the magnetic energy dissipation, (3) the unsigned line-of-sight magnetic flux, (4) the horizontal velocities of random footpoint motions in the photosphere, and (5) a proxy for the Poynting flux. The strongest correlated parameters were found to be magnetic flux and 1-D Poynting flux. The energy of the Poynting flux of the majority of active regions is sufficient to heat the corona. Therefore, kinetic energy in the form of foot point motion may be the main source of coronal heating. Furthermore, the author investigated the 3-D Poynting flux from the vector magnetograms and flow map and as well as free magnetic energy based on NLFF field extrapolation. After tracking the evolutions of Poynting flux and free magnetic energy of two flare-quiet active regions, the evolution trends of coronal X-ray brightness follow those of free magnetic energy more closely were found. The free magnetic energy is not only related to the unsigned total magnetic flux, but also the nonpotentiality of the magnetic field. Therefore, the three strongly coronal-heating related parameters are established: magnetic flux, Poynting flux and free magnetic energy. In addition, the coronal hole, with lower coronal emission and temperature, is another important subject to be studied in order to solve mystery of coronal heating problem. The difference of the magnetic dynamics between the boundaries and center parts of coronal holes was examined. The author found the magnetic fields of coronal hole boundaries are more dynamic than those inside the coronal holes — supporting the theories of flux transport and reconnection in the boundary of CHs (Wang & Sheeley 1994; Fisk 2005).

The transient coronal events, namely solar flares have been studied for 150 years (Carrington 1859; Hodgson 1859). It is well known that the flare energy is from the magnetic fields. The magnetic nonpotentiality was confirmed to be strongly correlated with flare productivity (e.g., Jing et al. 2006). Our study was to investigate the correlation between free magnetic energy and flare productivity. This becomes possible because advanced data and data processing tools are available recently. Based on 75 samples, a positive correlation between the free magnetic energy and the flare index was found. The temporal variation of free magnetic energy of three active regions, two are flare-active and one is flare-quiet, were studied as well. The author concluded that the flare triggering mechanism may be more important than the overall correlation in predicting flares. In addition, as a single case study, the optical penumbral and shear flows of NOAA 10930, associated with an X3.4 flare on 2006 December 13, were studied. The author found the mean magnitude of the horizontal speeds of the penumbral flows within the penumbral decay areas decreases permanently as a result of the flare and proposed the decays of the penumbra and the penumbral flow are related to the rearrangement of magnetic topology associated with the flare. This magnetic rearrangement is likely the result of the free magnetic energy release.

In the near future, New Solar Telescope (*NST*) and Solar Dynamics Observatory (*SDO*) will provide high resolution and high cadence data. These high-quality data will help to advance the knowledge of solar magnetic fields which are related to physics of coronal heating and flares. Applying our technique on the new data, the Poyting flux and free magnetic energy could be computed more precisely. This will be helpful to verify coronal heating models from the observational aspect. On the other hand, the flare triggering mechanisms will be extensively studied on the basis of high cadence vector magnetograms. The knowledge that was learned from flare study will be useful to flare forecasting or space weather which is closely related to daily lives of human beings.

REFERENCES

Abhyankar, K. D. 1977, Bulletin of the Astronomical Society of India, 5, 40.

Abramenko, V. I. 2005, Astrophys. J., 629, 1141.

Abramenko, V. I., Fisk, L. A., & Yurchyshyn, V. B. 2006a, Astrophys. J., Lett., 641, 65.

Abramenko, V. I., Pevtsov, A. A., & Romano, P. 2006b, Astrophys. J., Lett., 646, 81.

Abramenko, V. I., Yurchyshyn, V. B., Wang, H., Spirock, T. J., & Goode, P. R. 2003, Astrophys. J., 597, 1135.

Alexander, D. & Fletcher, L. 1999, Sol. Phys., 190, 167.

Aly, J. J. 1989, Sol. Phys., 120, 19.

Amari, T., Luciani, J. F., Mikic, Z., & Linker, J. 2000, Astrophys. J., Lett., 529, 49.

Antiochos, S. K. 1998, Astrophys. J., Lett., 502, 181.

Aschwanden, M. J. 2001, Astrophys. J., 560, 1035.

—. 2009, Physics of the Solar Corona (Springer in association with Praxis Publishing, Chichester, UK).

Aschwanden, M. J. & Nitta, N. 2000, Astrophys. J., Lett., 535, 59.

Barnes, G. & Leka, K. D. 2008, Astrophys. J., Lett., 688, 107.

Benz, A. O. 2008, Living Reviews in Solar Physics, 5, 1.

Berger, M. A. & Field, G. B. 1984, Journal of Fluid Mech., 147, 133.

Berger, T. E., Löfdahl, M. G., Shine, R. A., & Title, A. M. 1998, Astrophys. J., 506, 439.

Berger, T. E. & Title, A. M. 1996, Astrophys. J., 463, 365.

Bleybel, A., Amari, T., van Driel-Gesztelyi, L., & Leka, K. D. 2002, Astron. Astrophys., 395, 685.

Bogdan, T. J., Carlsson, M., Hansteen, V. H., McMurry, A., Rosenthal, C. S., Johnson, M., Petty-Powell, S., Zita, E. J., Stein, R. F., McIntosh, S. W., & Nordlund, Å. 2003, Astrophys. J., 599, 626.

Bray, R. J., Cram, L. E., Durrant, C. J., & Loughhead, R. E. 1991, Plasma loops in the solar corona. (Cambridge University Press, Cambridge, UK).

Bray, R. J., Loughhead, R. E., & Durant, C. J. 1984a, Astronomy Express, 1, 39.

Bray, R. J., Loughhead, R. E., & Durrant, C. J. 1984b, Journal of the British Astronomical Association, 94, 196.

Browning, P. K. 1991, Plasma Physics and Controlled Fusion, 33, 539.

Brueckner, G. E. & Bartoe, J. 1983, Astrophys. J., 272, 329.

Cabrera Solana, D., Bellot Rubio, L. R., Beck, C., & Del Toro Iniesta, J. C. 2007, Astron. Astrophys., 475, 1067.

Cargill, P. 1993, in Solar System Plasma Physics: Resolution of Processes in Space and Time, ed. J.L Birch & J.H. Waite, Jr.1993–2000.

Carmichael, H. 1964, NASA Special Publication, 50, 451.

Carrington, R. C. 1859, Monthly Notice of Roy. Astro. Soc., 20, 13.

Chae, J. 2001, Astrophys. J., Lett., 560, 95.

Chae, J., Moon, Y., & Park, Y. 2004, Sol. Phys., 223, 39.

Chae, J., Wang, H., Qiu, J., Goode, P. R., Strous, L., & Yun, H. S. 2001, Astrophys. J., 560, 476.

Chen, W., Liu, C., Song, H., Deng, N., Tan, C., & Wang, H. 2007, Chinese Journal of Astronomy and Astrophysics, 7, 733.

Collins, W. 1992, Astrophys. J., 384, 319.

Dahlburg, R. B., Klimchuk, J. A., & Antiochos, S. K. 2005, Astrophys. J., 622, 1191.

Degenhardt, D. 1991, Astron. Astrophys., 248, 637.

Delaboudinière, J., Artzner, G. E., Brunaud, J., Gabriel, A. H., Hochedez, J. F., Millier, F., Song, X. Y., Au, B., Dere, K. P., Howard, R. A., Kreplin, R., Michels, D. J., Moses, J. D., Defise, J. M., Jamar, C., Rochus, P., Chauvineau, J. P., Marioge, J. P., Catura, R. C., Lemen, J. R., Shing, L., Stern, R. A., Gurman, J. B., Neupert, W. M., Maucherat, A., Clette, F., Cugnon, P., & van Dessel, E. L. 1995, Sol. Phys., 162, 291.

Delaboudinière, J., Stern, R. A., Maucherat, A., Portier-Fozzani, F., Neupert, W. M., Gurman, J. B., Catura, R. C., Lemen, J. R., Shing, L., Artzner, G. E., Brunaud, J., Gabriel, A. H., Michels, D. J., Moses, J. D., Au, B., Dere, K. P., Howard, R. A., Kreplin, R., Defise, J. M., Jamar, C., Rochus, P., Chauvineau, J. P., Marioge, J. P., Clette, F., Cugnon, P., & van Dessel, E. L. 1997, Advances in Space Research, 20, 2231.

Démoulin, P., van Driel-Gesztelyi, L., Mandrini, C. H., Klimchuk, J. A., & Harra, L. 2003, Astrophys. J., 586, 592.

Deng, N., Liu, C., Yang, G., Wang, H., & Denker, C. 2005, Astrophys. J., 623, 1195.

Denker, C. 2005, in Astrophysics and Space Science Library, Vol. 320, Solar Magnetic Phenomena, ed. A. Hanslmeier, A. Veronig, & M. Messerotti1–25.

Denker, C., Deng, N., Tritschler, A., & Yurchyshyn, V. 2007, Sol. Phys., 245, 219.

Dennis, B. R. 1985, Sol. Phys., 100, 465.

DeRosa, M. L., Schrijver, C. J., Barnes, G., Leka, K. D., Lites, B. W., Aschwanden, M. J., Amari, T., Canou, A., McTiernan, J. M., Régnier, S., Thalmann, J. K., Valori, G., Wheatland, M. S., Wiegelmann, T., Cheung, M. C. M., Conlon, P. A., Fuhrmann, M., Inhester, B., & Tadesse, T. 2009, Astrophys. J., 696, 1780.

Edlén, B. 1943, Zeitschrift fur Astrophysik, 22, 30.

Evershed, J. 1909, Monthly Notice of Roy. Astro. Soc., 69, 454.

Falconer, D. A. 2001, J. Geophys. Res., 106, 25185.

Falconer, D. A., Moore, R. L., & Gary, G. A. 2003, Journal of Geophysical Research (Space Physics), 108, 1380.

Falconer, D. A., Moore, R. L., Porter, J. G., Gary, G. A., & Shimizu, T. 1997, Astrophys. J., 482, 519.

Faurobert, M. 2000, in Astronomical Society of the Pacific Conference Series, Vol. 205, Last Total Solar Eclipse of the Millennium, ed. W. Livingston & A. Özgüç156–170.

Feldman, U., Widing, K. G., & Warren, H. P. 1999, Astrophys. J., 522, 1133.

Fisher, G. H., Longcope, D. W., Metcalf, T. R., & Pevtsov, A. A. 1998, Astrophys. J., 508, 885.

Fisk, L. A. 2005, Astrophys. J., 626, 563.

Forbes, T. G. & Priest, E. R. 1995, Astrophys. J., 446, 377.

Gary, D. E. & Hurford, G. J. 1994, Astrophys. J., 420, 903.

Gary, G. A. 2001, Sol. Phys., 203, 71.

Gary, G. A. & Hagyard, M. J. 1990, Sol. Phys., 126, 21.

Georgakilas, A. A. & Christopoulou, E. B. 2003, Astrophys. J., 584, 509.

Georgoulis, M. K. & Rust, D. M. 2007, Astrophys. J., Lett., 661, 109.

Gibson, S., Bastian, T., Lin, H., Low, B. C., & Tomczyk. 2009, in Astronomy, Vol. 2010, AGB Stars and Related Phenomenastro2010: The Astronomy and Astrophysics Decadal Survey94–100.

Golub, L., Deluca, E., Austin, G., Bookbinder, J., Caldwell, D., Cheimets, P., Cirtain, J., Cosmo, M., Reid, P., Sette, A., Weber, M., Sakao, T., Kano, R., Shibasaki, K., Hara, H., Tsuneta, S., Kumagai, K., Tamura, T., Shimojo, M., McCracken, J., Carpenter, J., Haight, H., Siler, R., Wright, E., Tucker, J., Rutledge, H., Barbera, M., Peres, G., & Varisco, S. 2007, Sol. Phys., 243, 63.

Golub, L., Maxson, C., Rosner, R., Vaiana, G. S., & Serio, S. 1980, Astrophys. J., 238, 343.

Grotrian, W. 1939, Naturwissenschaften, 27, 214.

Guillermier, P. & Koutchmy, S. 1999, Total Eclipses (Springer - Praxis Series in Astronomy, Springer - Verlag, Berlin and Praxis Publishing, Chichester, UK).

Guo, Y., Ding, M. D., Wiegelmann, T., & Li, H. 2008, Astrophys. J., 679, 1629.

Hart, A. B. 1954, Monthly Notice of Roy. Astro. Soc., 114, 17.

—. 1956, Monthly Notice of Roy. Astro. Soc., 116, 38.

Harvey, J. W. 1977, Highlights of Astronomy, 4, 223.

Harvey, J. W., Krieger, A. S., Timothy, A. F., & Vaiana, G. S. 1975, Osserv. Mem. Oss. Astrofis. Arcetri, 104, 50.

Harvey, K. L. & Harvey, J. W. 1976, Sol. Phys., 47, 233.

Heyvaerts, J., Priest, E. R., & Rust, D. M. 1977, Astrophys. J., 216, 123.

Hirayama, T. 1974, Sol. Phys., 34, 323.

Hodgson, R. 1859, Monthly Notice of Roy. Astro. Soc., 20, 15.

Hollweg, J. V. 1993, in Mechanisms of Chromospheric and Coronal Heating, Springer-Verlag, Berlin, ed. P. Ulmshneider, E.R. Priest & R. Rosner423–500.

Howard, R. 1963, Astrophys. J., 138, 1312.

Insley, J. E., Moore, V., & Harrison, R. A. 1995, Sol. Phys., 160, 1.

Jing, J., Chen, P. F., Wiegelmann, T., Xu, Y., Park, S., & Wang, H. 2009a, Astrophys. J., 696, 84.

Jing, J., Song, H., Abramenko, V., Tan, C., & Wang, H. 2006, Astrophys. J., 644, 1273.

Jing, J., Tan, C., Yuan, Y., Wang, B., Wiegelmann, T., Xu, Y., & Wang, H. 2009b, Submitted to ApJ.

Jing, J., Wiegelmann, T., Suematsu, Y., Kubo, M., & Wang, H. 2008, Astrophys. J., Lett., 676, 81.

Jing, J., Yurchyshyn, V. B., Yang, G., Xu, Y., & Wang, H. 2004, Astrophys. J., 614, 1054.

Kahler, S. W. & Hudson, H. S. 2002, Astrophys. J., 574, 467.

Katsukawa, Y. & Tsuneta, S. 2005, Astrophys. J., 621, 498.

Keller, C. U. & Nso Staff. 1998, in Astronomical Society of the Pacific Conference Series, Vol. 154, Cool Stars, Stellar Systems, and the Sun, ed. R. A. Donahue & J. A. Bookbinder636–640.

Klimchuk, J. A. 2006, Sol. Phys., 234, 41.

Klimchuk, J. A. & Canfield, R. C. 1994, in Astronomical Society of the Pacific Conference Series, Vol. 68, Solar Active Region Evolution: Comparing Models with Observations, ed. K. S. Balasubramaniam & G. W. Simon233–240.

Klimchuk, J. A., Canfield, R. C., & Rhoads, J. E. 1992, Astrophys. J., 385, 327.

Kopp, R. A. & Pneuman, G. W. 1976, Sol. Phys., 50, 85.

Kosugi, T., Matsuzaki, K., Sakao, T., Shimizu, T., Sone, Y., Tachikawa, S., Hashimoto, T., Minesugi, K., Ohnishi, A., Yamada, T., Tsuneta, S., Hara, H., Ichimoto, K., Suematsu, Y., Shimojo, M., Watanabe, T., Shimada, S., Davis, J. M., Hill, L. D., Owens, J. K., Title, A. M., Culhane, J. L., Harra, L. K., Doschek, G. A., & Golub, L. 2007, Sol. Phys., 243, 3.

Krieger, A. S., Timothy, A. F., & Roelof, E. C. 1973, Sol. Phys., 29, 505.

Kudoh, T. & Shibata, K. 1999, Astrophys. J., 514, 493.

Kusano, K., Maeshiro, T., Yokoyama, T., & Sakurai, T. 2003a, Advances in Space Research, 32, 1917.

Kusano, K., Yokoyama, T., Maeshiro, T., & Sakurai, T. 2003b, Advances in Space Research, 32, 1931.

LaBonte, B. J., Georgoulis, M. K., & Rust, D. M. 2007, Astrophys. J., 671, 955.

Landé, A. 1937, Principles of Quantum Mechanics (The Macmillan company, The University press (New York, Cambridge)).

Langhans, K. & Schmidt, W. 2002, Astron. Astrophys., 382, 312.

Leka, K. D. & Barnes, G. 2003, Astrophys. J., 595, 1277.

—. 2007, Astrophys. J., 656, 1173.

Leka, K. D. & Skumanich, A. 1998, Astrophys. J., 507, 454.

Li, Y., Jing, J., & Wang, H. 2008SP51C–01.

Lin, H., Kuhn, J. R., & Coulter, R. 2004, Astrophys. J., Lett., 613, 177.

Lin, R. P., Schwartz, R. A., Kane, S. R., Pelling, R. M., & Hurley, K. C. 1984, Astrophys. J., 283, 421.

Lites, B. W. & Skumanich, A. 1990, Astrophys. J., 348, 747.

Liu, C. 2007, PhD thesis, New Jersey Inst. of Tech., Newark.

Liu, C., Deng, N., Liu, Y., Falconer, D., Goode, P. R., Denker, C., & Wang, H. 2005, Astrophys. J., 622, 722.

Liu, C., Lee, J., Karlický, M., Prasad Choudhary, D., Deng, N., & Wang, H. 2009, Astrophys. J., 703, 757.

Livingston, W. C. & Harvey, J. 1975, Bull. AAS, 7, 346.

Lüst, R. & Schlüter, A. 1954, Zeitschrift fur Astrophysik, 34, 263.

Madjarska, M. S. & Wiegelmann, T. 2009, Astron. Astrophys., 503, 991.

Maeshiro, T., Kusano, K., Yokoyama, T., & Sakurai, T. 2005, Astrophys. J., 620, 1069.

Mandrini, C. H., Démoulin, P., & Klimchuk, J. A. 2000, Astrophys. J., 530, 999.

Metcalf, T. R. 1994, Sol. Phys., 155, 235.

Metcalf, T. R., Canfield, R. C., Hudson, H. S., Mickey, D. L., Wulser, J., Martens, P. C. H., & Tsuneta, S. 1994, Astrophys. J., 428, 860.

Metcalf, T. R., De Rosa, M. L., Schrijver, C. J., Barnes, G., van Ballegooijen, A. A., Wiegelmann, T., Wheatland, M. S., Valori, G., & McTtiernan, J. M. 2008, Sol. Phys., 247, 269.

Metcalf, T. R., Leka, K. D., Barnes, G., Lites, B. W., Georgoulis, M. K., Pevtsov, A. A., Balasubramaniam, K. S., Gary, G. A., Jing, J., Li, J., Liu, Y., Wang, H. N., Abramenko, V., Yurchyshyn, V., & Moon, Y. 2006, Sol. Phys., 237, 267.

Milne, E. A. 1921, Monthly Notice of Roy. Astro. Soc., 81, 361.

Moon, Y., Chae, J., Choe, G. S., Wang, H., Park, Y. D., Yun, H. S., Yurchyshyn, V., & Goode, P. R. 2002a, Astrophys. J., 574, 1066.

Moon, Y., Chae, J., Wang, H., Choe, G. S., & Park, Y. D. 2002b, Astrophys. J., 580, 528.

Moore, R. L. & Labonte, B. J. 1980, in IAU Symposium, Vol. 91, Solar and Interplanetary Dynamics, ed. K. V. Sheridan & G. A. Dulk207–210.

Moore, R. L. & Roumeliotis, G. 1992, in Lecture Notes in Physics, Berlin Springer Verlag, Vol. 399, IAU Colloq. 133: Eruptive Solar Flares, ed. Z. Svestka, B. V. Jackson, & M. E. Machado69–75.

Moore, R. L., Sterling, A. C., Hudson, H. S., & Lemen, J. R. 2001, Astrophys. J., 552, 833.

Moriyasu, S., Kudoh, T., Yokoyama, T., & Shibata, K. 2004, Astrophys. J., Lett., 601, 107.

Moses, D., Clette, F., Delaboudinière, J., Artzner, G. E., Bougnet, M., Brunaud, J., Carabetian, C., Gabriel, A. H., Hochedez, J. F., Millier, F., Song, X. Y., Au, B., Dere, K. P., Howard, R. A., Kreplin, R., Michels, D. J., Defise, J. M., Jamar, C., Rochus, P., Chauvineau, J. P., Marioge, J. P., Catura, R. C., Lemen, J. R., Shing, L., Stern, R. A., Gurman, J. B., Neupert, W. M., Newmark, J., Thompson, B., Maucherat, A., Portier-Fozzani, F., Berghmans, D., Cugnon, P., van Dessel, E. L., & Gabryl, J. R. 1997, Sol. Phys., 175, 571.

Mosher, J. M. 1977, PhD thesis, California Inst. of Tech., Pasadena.

Muller, R., Roudier, T., Vigneau, J., & Auffret, H. 1994, Astron. Astrophys., 283, 232.

Narain, U. & Ulmschneider, P. 1996, Space Science Reviews, 75, 453.

November, L. J. & Simon, G. W. 1988, Astrophys. J., 333, 427.

Pallavicini, R., Serio, S., & Vaiana, G. S. 1977, Astrophys. J., 216, 108.

Park, S., Lee, J., Choe, G. S., Chae, J., Jeong, H., Yang, G., Jing, J., & Wang, H. 2008, Astrophys. J., 686, 1397.

Parker, E. N. 1957, J. Geophys. Res., 62, 509.

—. 1979, Cosmical magnetic fields: Their origin and their activity, ed. E. N. Parker (Oxford, Clarendon Press; New York, Oxford University Press, 1979, 858 p.).

—. 1983, Astrophys. J., 264, 642.

—. 1988, Astrophys. J., 330, 474.

—. 1991a, Astrophys. J., 372, 719.

—. 1991b, Astrophys. J., 376, 355.

Patsourakos, S. & Klimchuk, J. A. 2006, Astrophys. J., 647, 1452.

Pearce, G. & Harrison, R. A. 1990, Astron. Astrophys., 228, 513.

Petschek, H. E. 1964, NASA Special Publication, 50, 425.

Pevtsov, A. A. & Kazachenko, M. 2004, in ESA Special Publication, Vol. 575, SOHO 15 Coronal Heating, ed. R. W. Walsh, J. Ireland, D. Danesy, & B. Fleck241–250.

Priest, E. & Forbes, T. 2000, Magnetic Reconnection (Cambridge University Press, Cambridge UK).

Priest, E. R. 1990, Mem. Soc. Astron. Ital., 61, 383.

Reale, F., Parenti, S., Reeves, K. K., Weber, M., Bobra, M. G., Barbera, M., Kano, R., Narukage, N., Shimojo, M., Sakao, T., Peres, G., & Golub, L. 2007, Science, 318, 1582.

Reale, F. & Peres, G. 2000, Astrophys. J., Lett., 528, 45.

Reale, F., Testa, P., Klimchuk, J. A., & Parenti, S. 2009, Astrophys. J., 698, 756.

Régnier, S., Amari, T., & Kersalé, E. 2002, Astron. Astrophys., 392, 1119.

Régnier, S. & Canfield, R. C. 2006, Astron. Astrophys., 451, 319.

Rimmele, T. R. 1994, Astron. Astrophys., 290, 972.

Rudenko, G. V. & Myshyakov, I. I. 2009, Sol. Phys., 257, 287.

Sakurai, T. 1981, Sol. Phys., 69, 343.

Sánchez Almeida, J., Márquez, I., Bonet, J. A., & Domínguez Cerdeña, I. 2007, Astrophys. J., 658, 1357.

Sánchez Cuberes, M., Puschmann, K. G., & Wiehr, E. 2005, Astron. Astrophys., 440, 345.

Scherrer, P. H., Bogart, R. S., Bush, R. I., Hoeksema, J. T., Kosovichev, A. G., Schou, J., Rosenberg, W., Springer, L., Tarbell, T. D., Title, A., Wolfson, C. J., Zayer, I., & MDI Engineering Team. 1995, Sol. Phys., 162, 129.

Schmelz, J. T., Saar, S. H., DeLuca, E. E., Golub, L., Kashyap, V. L., Weber, M. A., & Klimchuk, J. A. 2009, Astrophys. J., Lett., 693, 131.

Schrijver, C. J. 2007, Astrophys. J., Lett., 662, 119.

Schrijver, C. J., De Rosa, M. L., Metcalf, T. R., Liu, Y., McTiernan, J., Régnier, S., Valori, G., Wheatland, M. S., & Wiegelmann, T. 2006, Sol. Phys., 235, 161.

Schrijver, C. J., De Rosa, M. L., Title, A. M., & Metcalf, T. R. 2005, Astrophys. J., 628, 501.

Schrijver, C. J., Sandman, A. W., Aschwanden, M. J., & De Rosa, M. L. 2004, Astrophys. J., 615, 512.

Schrijver, C. J., Zwaan, C., Maxson, C. W., & Noyes, R. W. 1985, Astron. Astrophys., 149, 123.

Schwarzchild, M. 1959, Astrophys. J., 130, 345.

Shibata, K., Ishido, Y., Acton, L. W., Strong, K. T., Hirayama, T., Uchida, Y., McAllister, A. H., Matsumoto, R., Tsuneta, S., Shimizu, T., Hara, H., Sakurai, T., Ichimoto, K., Nishino, Y., & Ogawara, Y. 1992, Publ. Astron. Soc. Jpn., 44, L173.

Shine, R. A., Title, A. M., Tarbell, T. D., Smith, K., Frank, Z. A., & Scharmer, G. 1994, Astrophys. J., 430, 413.

Simon, G. W., Brandt, P. N., November, L. J., Shine, R. A., & Strous, L. H. 1995, in 223–226.

Simon, G. W., Title, A. M., Topka, K. P., Tarbell, T. D., Shine, R. A., Ferguson, S. H., Zirin, H., & SOUP Team. 1988, Astrophys. J., 327, 964.

Skumanich, A. & Lites, B. W. 1987, Astrophys. J., 322, 473.

Solanki, S. K. 2003, Astron. Astrophys. Rev., 11, 153.

Solanki, S. K., Montavon, C. A. P., & Livingston, W. 1994, Astron. Astrophys., 283, 221.

Solanki, S. K., Rueedi, I., & Livingston, W. 1992, Astron. Astrophys., 263, 339.

Song, H., Jing, J., Tan, C., & Wang, H. 2006a, in Bulletin of the American Astronomical Society, Vol. 38, Bulletin of the American Astronomical Society236–240.

Song, H., Tan, C., Jing, J., Wang, H., Yurchyshyn, V., & Abramenko, V. 2009, Sol. Phys., 254, 101.

Song, H., Yurchyshyn, V., Yang, G., Tan, C., Chen, W., & Wang, H. 2006b, Sol. Phys., 238, 141.

Spicer, D. S. 1991, in Mechanisms of Chromospheric and Coronal Heating, ed. P. Ulmschneider, E. R. Priest, & R. Rosner547–550.

Spirock, T. J., Yurchyshyn, V. B., & Wang, H. 2002, Astrophys. J., 572, 1072.

Stein, R. F. & Nordlund, Å. 1991, in Mechanisms of Chromospheric and Coronal Heating, ed. P. Ulmschneider, E. R. Priest, & R. Rosner386–400.

Stix, M. 1989, The Sun (Springer-Verlago Berlin Heidelberg, New York).

Sturrock, P. A. 1966, Nature, 211, 697.

—. 1989, Sol. Phys., 121, 387.

Sudol, J. J. & Harvey, J. W. 2005, Astrophys. J., 635, 647.

Suematsu, Y., Tsuneta, S., Ichimoto, K., Shimizu, T., Otsubo, M., Katsukawa, Y., Nakagiri, M., Noguchi, M., Tamura, T., Kato, Y., Hara, H., Kubo, M., Mikami, I., Saito, H., Matsushita, T., Kawaguchi, N., Nakaoji, T., Nagae, K., Shimada, S., Takeyama, N., & Yamamuro, T. 2008, Sol. Phys., 249, 197.

Sweet, P. A. 1958, Electromagnetic Phenomena in Cosmical Physics (Cambridge University Press, Cambridge UK).

Tan, C., Chen, P. F., Abramenko, V., & Wang, H. 2009, Astrophys. J., 690, 1820.

Tan, C., Jing, J., Abramenko, V. I., Pevtsov, A. A., Song, H., Park, S., & Wang, H. 2007, Astrophys. J., 665, 1460.

Thalmann, J. K. & Wiegelmann, T. 2008, Astron. Astrophys., 484, 495.

Thalmann, J. K., Wiegelmann, T., & Raouafi, N. 2008, Astron. Astrophys., 488, L71.

Timothy, A. F., Krieger, A. S., & Vaiana, G. S. 1975, Sol. Phys., 42, 135.

Title, A. M., Frank, Z. A., Shine, R. A., Tarbell, T. D., Topka, K. P., Scharmer, G., & Schmidt, W. 1993, Astrophys. J., 403, 780.

Title, A. M., Tarbell, T. D., & Topka, K. P. 1987, Astrophys. J., 317, 892.

Title, A. M., Topka, K. P., Tarbell, T. D., Schmidt, W., Balke, C., & Scharmer, G. 1992, Astrophys. J., 393, 782.

Tritschler, A., Schlichenmaier, R., Bellot Rubio, L. R., the KAOS Team, Berkefeld, T., & Schelenz, T. 2004, Astron. Astrophys., 415, 717.

Tsiklauri, D. 2005, Astron. Astrophys., 441, 1177.

Tsuneta, S., Acton, L., Bruner, M., Lemen, J., Brown, W., Caravalho, R., Catura, R., Freeland, S., Jurcevich, B., & Owens, J. 1991, Sol. Phys., 136, 37.

Tsuneta, S., Ichimoto, K., Katsukawa, Y., Nagata, S., Otsubo, M., Shimizu, T., Suematsu, Y., Nakagiri, M., Noguchi, M., Tarbell, T., Title, A., Shine, R., Rosenberg, W., Hoffmann, C., Jurcevich, B., Kushner, G., Levay, M., Lites, B., Elmore, D., Matsushita, T., Kawaguchi, N., Saito, H., Mikami, I., Hill, L. D., & Owens, J. K. 2008, Sol. Phys., 249, 167.

Uchida, Y. 1980, in Japan-France Seminar on Solar Physics, ed. F. Moriyama & J. C. Henoux83–86.

van Speybroek, L. P., Krieger, A. S., & Vaiana, G. S. 1970, Nature, 227, 818.

Waldmeier, M. 1938, Zeitschrift fur Astrophysik, 15, 299.

Wang, H. 1992, Sol. Phys., 140, 85.

—. 2006, Astrophys. J., 649, 490.

Wang, H., Ji, H., Schmahl, E. J., Qiu, J., Liu, C., & Deng, N. 2002a, Astrophys. J., Lett., 580, 177.

Wang, H., Liu, C., Qiu, J., Deng, N., Goode, P. R., & Denker, C. 2004a, Astrophys. J., Lett., 601, 195.

Wang, H., Song, H., Jing, J., Yurchyshyn, V., Deng, Y., Zhang, H., Falconer, D., & Li, J. 2006, Chinese Journal of Astronomy and Astrophysics, 6, 477.

Wang, H., Spirock, T. J., Qiu, J., Ji, H., Yurchyshyn, V., Moon, Y., Denker, C., & Goode, P. R. 2002b, Astrophys. J., 576, 497.

Wang, J., Zhou, G., & Zhang, J. 2004b, Astrophys. J., 615, 1021.

Wang, Y., Hawley, S. H., & Sheeley, Jr., N. R. 1996, Science, 271, 464.

Wang, Y., Noyes, R. W., Tarbell, T. D., & Title, A. M. 1995, Astrophys. J., 447, 419.

Wang, Y. & Sheeley, Jr., N. R. 1994, Astrophys. J., 430, 399.

Warren, H. P., Winebarger, A. R., & Hamilton, P. S. 2002, Astrophys. J., Lett., 579, 41.

Welsch, B. T., Fisher, G. H., Abbett, W. P., & Regnier, S. 2004, Astrophys. J., 610, 1148.

Wheatland, M. S., Sturrock, P. A., & Roumeliotis, G. 2000, Astrophys. J., 540, 1150.

Wiegelmann, T. 2004, Sol. Phys., 219, 87.

Wiegelmann, T., Inhester, B., & Feng, L. 2009, Ann.Geophys., 27, 2925.

Wiegelmann, T., Inhester, B., & Sakurai, T. 2006, Sol. Phys., 233, 215.

Wiegelmann, T., Thalmann, J. K., Schrijver, C. J., De Rosa, M. L., & Metcalf, T. R. 2008, Sol. Phys., 247, 249.

Wiegelmann, T., Xia, L. D., & Marsch, E. 2005, Astron. Astrophys., 432, 1.

Withbroe, G. L. & Noyes, R. W. 1977, Annual Review of Astron. & Astrophys., 15, 363.

Wolfson, R., Roald, C. B., Sturrock, P. A., & Weber, M. A. 2000, Astrophys. J., 539, 995.

Yang, G., Xu, Y., Cao, W., Wang, H., Denker, C., & Rimmele, T. R. 2004, Astrophys. J., Lett., 617, 151.

Yashiro, S. & Shibata, K. 2001, Astrophys. J., Lett., 550, 113.

Yokoyama, T., Kusano, K., Maeshiro, T., & Sakurai, T. 2003, Advances in Space Research, 32, 1949.

Yurchyshyn, V., Wang, H., Abramenko, V., Spirock, T. J., & Krucker, S. 2004, Astrophys. J., 605, 546.

Zhang, H. 2001, Astrophys. J., Lett., 557, 71.

Zhang, J., Li, L., & Song, Q. 2007, Astrophys. J., Lett., 662, 35.

Zhang, J., Ma, J., & Wang, H. 2006, Astrophys. J., 649, 464.

Zirin, H. & Wang, H. 1993, Nature, 363, 426.

Zirker, J. B. 1993, Sol. Phys., 148, 43.